

INFORMATION TO USERS

This was produced from a copy of a document sent to us for microfilming. While the most advanced technological means to photograph and reproduce this document have been used, the quality is heavily dependent upon the quality of the material submitted.

The following explanation of techniques is provided to help you understand markings or notations which may appear on this reproduction.

1. The sign or "target" for pages apparently lacking from the document photographed is "Missing Page(s)". If it was possible to obtain the missing page(s) or section, they are spliced into the film along with adjacent pages. This may have necessitated cutting through an image and duplicating adjacent pages to assure you of complete continuity.
2. When an image on the film is obliterated with a round black mark it is an indication that the film inspector noticed either blurred copy because of movement during exposure, or duplicate copy. Unless we meant to delete copyrighted materials that should not have been filmed, you will find a good image of the page in the adjacent frame.
3. When a map, drawing or chart, etc., is part of the material being photographed the photographer has followed a definite method in "sectioning" the material. It is customary to begin filming at the upper left hand corner of a large sheet and to continue from left to right in equal sections with small overlaps. If necessary, sectioning is continued again—beginning below the first row and continuing on until complete.
4. For any illustrations that cannot be reproduced satisfactorily by xerography, photographic prints can be purchased at additional cost and tipped into your xerographic copy. Requests can be made to our Dissertations Customer Services Department.
5. Some pages in any document may have indistinct print. In all cases we have filmed the best available copy.

University
Microfilms
International

300 N. ZEEB ROAD, ANN ARBOR, MI 48106
18 BEDFORD ROW, LONDON WC1R 4EJ, ENGLAND

8104292

HOWELL, ROBERT RICHARD

INFRARED SPECKLE INTERFEROMETRY

The University of Arizona

PH.D.

1980

University
Microfilms
International 300 N. Zeeb Road, Ann Arbor, MI 48106

PLEASE NOTE:

In all cases this material has been filmed in the best possible way from the available copy. Problems encountered with this document have been identified here with a check mark .

1. Glossy photographs _____
2. Colored illustrations _____
3. Photographs with dark background _____
4. Illustrations are poor copy _____
5. Print shows through as there is text on both sides of page _____
6. Indistinct, broken or small print on several pages
7. Tightly bound copy with print lost in spine _____
8. Computer printout pages with indistinct print _____
9. Page(s) _____ lacking when material received, and not available from school or author
10. Page(s) _____ seem to be missing in numbering only as text follows
11. Poor carbon copy _____
12. Not original copy, several pages with blurred type _____
13. Appendix pages are poor copy _____
14. Original copy with light type _____
15. Curling and wrinkled pages _____
16. Other _____

INFRARED SPECKLE INTERFEROMETRY

by

Robert Richard Howell

A Dissertation Submitted to the Faculty of the

DEPARTMENT OF PLANETARY SCIENCES

In Partial Fulfillment of the Requirements
For the Degree of

DOCTOR OF PHILOSOPHY

In the Graduate College

THE UNIVERSITY OF ARIZONA

1980

THE UNIVERSITY OF ARIZONA
GRADUATE COLLEGE

As members of the Final Examination Committee, we certify that we have read
the dissertation prepared by Robert Richard Howell
entitled Infrared Speckle Interferometry

and recommend that it be accepted as fulfilling the dissertation requirement
for the Degree of Doctor of Philosophy.

<u>Frank J. Law</u>	<u>Oct. 13, 1980</u>
Date	
<u>J. R. Johnson</u>	<u>"</u>
Date	
<u>W. Wilson</u>	<u>"</u>
Date	
<u>J. Wilson</u>	<u>"</u>
Date	
<u>Michael J. Drah</u>	<u>"</u>
Date	

Final approval and acceptance of this dissertation is contingent upon the
candidate's submission of the final copy of the dissertation to the Graduate
College.

I hereby certify that I have read this dissertation prepared under my
direction and recommend that it be accepted as fulfilling the dissertation
requirement.

<u>Frank J. Law</u>	<u>Oct. 13, 1980</u>
Dissertation Director	Date

STATEMENT BY AUTHOR

This dissertation has been submitted in partial fulfillment of requirements for an advanced degree at The University of Arizona and is deposited in the University Library to be made available to borrowers under rules of the Library.

Brief quotations from this dissertation are allowable without special permission, provided that accurate acknowledgment of source is made. Requests for permission for extended quotation from or reproduction of this manuscript in whole or in part may be granted by the head of the major department or the Dean of the Graduate College when in his judgment the proposed use of the material is in the interests of scholarship. In all other instances, however, permission must be obtained from the author.

SIGNED: Robert R. Howell

ACKNOWLEDGMENTS

This dissertation would not have been possible without the advice and assistance of many people. Don McCarthy built much of the equipment borrowed from the Michelson project and provided invaluable assistance with the observations and their interpretation. George Rieke, Marcia Lebofsky, and Rodger Thompson provided the He cooled InSb detector. George and Marcia also cheerfully tolerated the inconvenience caused by my using their word processor for this text. Many friends have provided encouragement and advice. Nancy Lebofsky answered innumerable questions concerning the typing of the dissertation. The spatial interferometry program is supported by the National Science Foundation. Finally I would like to thank my advisor, Frank Low, for his patient support during the long course of this study.

TABLE OF CONTENTS

	Page
LIST OF TABLES	vii
LIST OF ILLUSTRATIONS	viii
ABSTRACT	x
1. INTRODUCTION	2
High Resolution at Infrared Wavelengths	2
Previous Work the University of Arizona	3
Outline of the Dissertation	4
2. THEORY OF SPECKLE INTERFEROMETRY	6
The Modulation Transfer Function	6
Atmospheric Turbulence	8
Atmosphere Degraded MTF.	10
Constraints on system parameters	14
Wavelength Bandpass	14
Exposure Time	16
Field of View	16
Telescope Aberrations.	16
3. EQUIPMENT AND DATA REDUCTION	17
Design Goals.	17
Photometer-Like Design	17
Good Seeing Conditions	18
Real Time Data Processing.	19
Control of Scan Direction.	19
The Optical System.	20
Scanning System.	20
Dewar Optics and Filters	26
Detectors and Electronics	32

TABLE OF CONTENTS--Continued

	Page
Data Recording and Processing	38
Character of the Scans	39
Real Time Photometry	39
Corrected Photometry	40
Speckle Scans.	40
4. CALIBRATION AND PERFORMANCE.	43
Spatial Frequency Calibration	43
Position Angle	49
Sensitivity	52
System Responsivity.	52
System Noise	53
Limiting Magnitudes.	55
Systematic Errors	57
Observed MTF.	61
Test Objects.	61
Double Stars	61
Asteroids.	65
Galilean Satellites.	67
5. OBSERVATIONS	70
Protostellar Objects.	70
W3 IRS 5	71
S140	77
Mon R2 IRS 3	78
BN	80
GL 490	82
GL 2591.	85
NGC 2264	85
Summary.	87
Evolved stars	89
IRC+10216.	90
Alpha Ori.	94

TABLE OF CONTENTS--Continued

	Page
VY CMa	97
Omicron Ceti	97
Other Objects.	97
6. SUMMARY AND FUTURE PLANS	106
APPENDIX A: SIGNAL-TO-NOISE RATIO.	110
BIBLIOGRAPHY	112

LIST OF TABLES

Table	Page
1. Filter characteristics	28
2. Slit diffraction effects	29
3. Dates of observations	44
4. Limiting magnitudes	56

LIST OF ILLUSTRATIONS

Figure	Page
1. Diffraction limited MTF	9
2. Refractive index structure constant	11
3. Atmosphere degraded MTF	13
4. The scanning secondary for the 229 cm telescope	23
5. Block diagram of the electronics and data system.	24
6. The position sensor output for one scan	25
7. Diffraction at the focal plane slit	31
8. The preamp for the N ₂ cooled InSb detector.	34
9. The N ₂ cooled InSb frequency response	35
10. The preamp for the He cooled InSb detector.	36
11. The He cooled InSb frequency response	37
12. The results of the digital frequency compensation	41
13. Scanner angle vs. position sensor voltage	45
14. Coadded scans of Alpha Psc and Alpha Gem.	47
15. Transform for double slit	50
16. Position angle adjustments.	51
17. Noise spectra and NEP's	54
18. Effects of the finite scan length	60
19. Observed MTF for the K filter	62
20. Observed MTF for the M filter	63
21. Alpha Psc visibility.	64
22. Vesta and Ceres visibilities.	66

LIST OF ILLUSTRATIONS--Continued

Figure	Page
23. Ganymede and Callisto visibilities.	68
24. W3 IRS 5 visibilities	73
25. Size limits for IRS 5 components.	75
26. W3 IRS 5 orientation, polarimetry, and H ₂ O masers	76
27. S140 IR visibility.	79
28. Mon R2 IRS 3 visibility	81
29. BN visibility	83
30. GL 490 visibility	84
31. GL 2591 visibility.	86
32. NGC 2264 IRS visibilities	88
33. IRC+10216 visibilities.	92
34. Comparison of IRC+10216 visibilities.	93
35. Alpha Ori visibility.	95
36. NML Tau visibility.	96
37. VY CMa visibilities	98
38. Omicron Ceti visibilities	99
39. IRC+10011 visibility.	100
40. RX Boo visibility	101
41. R Hyd visibility.	102
42. W Hyd visibility.	103
43. CIT 6 visibilities.	104

ABSTRACT

Since 1975 McCarthy and Low have conducted a program of Michelson spatial interferometry at infrared wavelengths, measuring a large number of evolved stars and protostellar objects. This dissertation discusses the development of an infrared speckle interferometer which was used to extend those observations. This instrument uses a modified version of the technique pioneered by Sibille, Chelli, and Lená. The secondary mirror is used to scan the image across a narrow slit. Each scan is fourier transformed, and the moduli squared of many such transforms are coadded. Both the object of interest and a point source are observed. The square root of the ratio of their power spectra is the visibility as defined by Michelson.

This system was assembled for the most part with existing equipment and the design should be readily adaptable to other observatories. Initial tests were made with the 154 cm telescope of the University of Arizona since it had a preexisting mechanism for scanning the secondary. However most of the observations were carried out with the University's 229 cm telescope. A new linear servo was added to the existing hard-stop chopper for this telescope's $f/45$ secondary.

Three detector systems were used to provide wavelength coverage from 2 to 12 microns. An N_2 cooled InSb and a He cooled bolometer were available from the Michelson program. In addition a high sensitivity He cooled InSb detector from the Steward Observatory FTS was used. Slits with an angular size of $\lambda/2D$, where D is the telescope diameter were

placed at the focal plane in the dewar. The narrow slit results in diffraction losses when used with conventional dewar optics. The loss could be eliminated with optics optimized for this application. However even with the loss, a large number of objects could be observed.

Test results at 2 microns were obtained for a double star, the asteroids Vesta and Ceres, and the Galilean satellites Ganymede and Callisto. The protostellar objects W3 IRS 5, S140, and Mon R2 IRS 3 were resolved. The separation, orientation, and relative brightness of the two components IRS 5 were measured at 5 microns. The separation is $1.26'' \pm 0.06$ and the position angle is $37^\circ \pm 5$. The brightness ratio is approximately 0.59. S140 and Mon R2 IRS 3 were observed at 2 microns. S140 shows some indication of an extended region of greater than $1''$ contributing half the flux. IRS 3 has a size of approximately $1''$ but the data is too noisy for an exact fit. Upper size limits were determined for BN, GL 490, GL 2591, and NGC 2264 IRS.

A large number of evolved stars were observed. The size of the shell around Alpha Ori was found to be $\sim 4''$ at 11 microns. Observations were obtained for IRC+10216 at 2, 5, 8, and 11 microns which further define the asymmetrical shape of this object. Observations were also obtained for VY CMa. Upper size limits were established for Omicron Ceti, IRC+10011, RX Boo, R Hyd, W Hyd, and CIT 6.

CHAPTER 1

INTRODUCTION

Our understanding of the world around us is to a large extent based on the spatial relationships we see. It is ironic therefore, that in astronomy so much of our knowledge of the spatial structure of objects must be derived indirectly. Until Michelson developed his spatial interferometer in 1920 all stars except our sun appeared as mere point sources of light. Their sizes could only be inferred from spectral and photometric measurements. Until recently the same situation prevailed in infrared astronomy. The sizes of the dust shells around both young and evolved stars were difficult to determine because of the large uncertainties in their optical thicknesses.

The first widely successful application of high resolution techniques came at radio wavelengths. There VLBI (very long baseline interferometry) can now give a resolution of milliarcseconds. The H_2O and OH masers surrounding some of the objects described later were in fact mapped using this technique.

Little progress was made at visible wavelengths for some time after the work of Michelson. But within the past few decades this has changed. Hanbury Brown (1974) and Twiss developed the technique known as intensity interferometry and Currie, Knapp, and Liewer (1974) applied photoelectric detectors to Michelson interferometry to enable precise measurements of the visibility function. Meanwhile Labyrie (1970)

developed speckle interferometry. This dissertation will be concerned with the application of this last technique to infrared wavelengths.

High Resolution at Infrared Wavelengths

Infrared astronomers have used three of the above techniques for achieving high resolution. The work of the Berkeley group (Sutton 1979, Sutton et al. 1977, Sutton, Storey, and Townes, 1978, Sutton et al. 1979) is essentially an adaptation of the radio technique, using lasers to heterodyne the infrared signals from independent telescopes into the radio frequency range and then combining these signals as is done in radio astronomy. The heterodyne technique has the advantage that it is relatively easy to use separate telescopes and therefore obtain large baselines. However it can only use extremely narrow bandwidths with a corresponding loss in sensitivity.

McCarthy has developed the Michelson technique, taking the light from two parts of a single telescope objective (McCarthy and Low 1975, McCarthy, Howell, and Low 1977a, 1977b, 1978, 1980; McCarthy, Low, and Howell 1979). This method has shown itself capable of providing highly accurate visibility measurements for spatial frequencies up to the aperture limit of a single telescope. Its primary disadvantage is that it provides information for only one spatial frequency at a time and the present instrument takes considerable time to realign for different spatial frequencies. Several of the objects observed are sufficiently complex that measurements at several spatial frequencies are needed to discern their structure.

The ability to make simultaneous measurements at many spatial frequencies is the principle advantage of the speckle technique. The application of speckle interferometry to infrared wavelengths has been pioneered by Chelli, Foy, Léna, and Sibille (Chelli 1979, Sibille, Léna, 1979, Foy et al. 1979). A modified version of it has been tested by Selby, Wade, and Magro (1979). The primary purpose of the work in this dissertation was to use the speckle method to extend the spatial frequency coverage for the kinds of objects which McCarthy had observed with the Michelson interferometer.

While we planned to acquire new data on the objects observed with the Michelson interferometer we felt that our first system should only be regarded as a prototype instrument. Therefore this work was carried out as far as possible using existing equipment. This approach forced some compromises in the performance of the system but resulted in a considerable savings in time and money. The use of the same detectors and telescopes also had the advantage of allowing a better comparison between the Michelson and speckle techniques.

Previous Work at the University of Arizona

This work is an extension of the spatial interferometry program begun at Arizona by McCarthy and Low. The Michelson interferometer developed by them covers the wavelength range of 2 to 20 microns. It has been used on several telescopes in the Tucson area, primarily for observing dust shells around late type stars and also around what are believed to be protostars. Before the Voyager I encounter with Jupiter it was used in a program which attempted to characterize the

distribution of water frost on the Galilean satellites. During this program it became increasingly obvious that an instrument which measured visibilities at many spatial frequencies was necessary. Also, a system was needed which was not subject to the alignment problems that become severe with the Michelson at short wavelengths.

While the satellite observing program was being conducted the first results on speckle interferometry in France and the United Kingdom became available. They showed that for some problems the speckle technique had clear advantages. Therefore we decided to build a prototype system. Initial observations were carried out at the 154 cm telescope during the spring of 1979. During the following year an improved system was used at the Steward 229 cm telescope. The results presented in this dissertation are taken mostly from the observations carried out at the 229 cm. At the present time Don McCarthy is working with Kitt Peak personnel designing a new speckle system for the 4 meter telescope. Some consideration is also being given to an instrument for the MMT.

Outline of the Dissertation

Chapter 2 is a short description of the principles of speckle interferometry and the special requirements at infrared wavelengths. This is followed by a chapter describing the equipment that we used and specific suggestions for improvements. The fourth chapter is a discussion of the instrument's performance along with results obtained for several test objects. The observations of protostars and evolved stars are discussed in chapter 5. Although the results on evolved stars

are reviewed, this dissertation does not present a detailed discussion of them. For these objects the speckle observations are an extension of the work done with the Michelson technique. Instead, this dissertation concentrates on the results for the protostars where the speckle results are a more self-contained set of data. The final chapter is a summary and a discussion of the relative merits of Michelson and speckle interferometry along with some suggestions for the future.

CHAPTER 2

THE THEORY OF SPECKLE INTERFEROMETRY

Many researchers have contributed to the theoretical framework of speckle interferometry over the past fifteen years. A useful overview of their results is presented by Fried (1979). The original work is presented in papers by Fried (1966), Roddier (1974), Dainty (1973) and several others. The paper by Korff (1973) is the most complete and the following discussion is based upon it. These papers deal mostly with visible wavelengths, and in order to be applied to infrared wavelengths several modifications are necessary. Some of this has been done by Sibille et al. (1979) and by Chelli (1979).

The Modulation Transfer Function

The turbulence in the atmosphere introduces phase and amplitude changes in the wavefront entering the telescope. Therefore instead of the Airy disk that would be produced by an aberration free telescope we observe a "seeing disk" that is typically a few arcseconds in diameter. While long exposures show no detail in this disk, short exposures show that structure exists out to the spatial frequency limit of the telescope:

$$f_0 = D/\lambda \tag{1}$$

where λ is the wavelength and D is the diameter of the objective. The goal of speckle interferometry is to preserve this high frequency information while integrating to obtain a useful signal to noise ratio.

For random processes such as "seeing" it is easier to describe the results in frequency rather than image space. If $o(\mathbf{f})$ is the Fourier transform of the object intensity and $T(\mathbf{f})$ is the transfer function of the atmosphere plus telescope then the Fourier transform of the image is given by

$$i(\mathbf{f}) = o(\mathbf{f}) \cdot T(\mathbf{f}) \quad . \quad (2)$$

As will be shown below $T(\mathbf{f})$ is nonzero out to f_0 . However, the phase of $T(\mathbf{f})$ is constantly changing and therefore the average $\langle T(\mathbf{f}) \rangle$ is zero for f much greater than $1/\theta_s$ where θ_s is the size of the seeing disk. To avoid this one can average $|i(\mathbf{f})|^2$ rather than $i(\mathbf{f})$ itself:

$$\langle |i(\mathbf{f})|^2 \rangle = |o(\mathbf{f})|^2 \cdot \langle |T(\mathbf{f})|^2 \rangle \quad . \quad (3)$$

This results in the loss of the phase information in $o(\mathbf{f})$ but for simple objects the modulus alone is useful. To find $|o(\mathbf{f})|$ it is necessary to know $\langle |T(\mathbf{f})|^2 \rangle$. The general form can be derived theoretically but for actual observations it is necessary to determine it by measuring a "point source". For a point source $o(\mathbf{f})$ is unity and therefore

$$\langle |i(\mathbf{f})|^2 \rangle = \langle |T(\mathbf{f})|^2 \rangle \quad . \quad (4)$$

This procedure has the advantage of including the instrumental frequency response.

The above are ensemble averages but in practice one assumes that the turbulence is stationary and ergodic. Therefore one measures the image in a time short enough to "freeze" the seeing, Fourier transforms this image, and averages $|i(\mathbf{f})|^2$ for many exposures. The exposure time necessary to freeze the seeing will be discussed later.

The modulation transfer function (MTF) of the optical system is obtained by integrating the complex amplitude of the wavefront, $U(\mathbf{r})$, over the objective:

$$T(\mathbf{f}) = B \int d\mathbf{r} U^*(\mathbf{r}) U(\mathbf{r}) \quad . \quad (5)$$

B is a constant typically chosen so the MTF is unity at DC. If $W(\mathbf{r})$ is the window function of the aperture (1 for points in the aperture, 0 otherwise) then

$$\begin{aligned} \langle |T(\mathbf{f})|^2 \rangle = B^2 \iint d\mathbf{r} d\mathbf{r}' W(\mathbf{r}) W(\mathbf{r}-\lambda\mathbf{f}) W(\mathbf{r}') W(\mathbf{r}'-\lambda\mathbf{f}) \\ \langle U(\mathbf{r}) U^*(\mathbf{r}-\lambda\mathbf{f}) U^*(\mathbf{r}') U(\mathbf{r}'-\lambda\mathbf{f}) \rangle \quad . \quad (6) \end{aligned}$$

In the absence of the atmosphere $\langle U(\mathbf{r}) U^*(\mathbf{r}-\lambda\mathbf{f}) U^*(\mathbf{r}') U(\mathbf{r}'-\lambda\mathbf{f}) \rangle$ would be unity and $T^2(\mathbf{f})$ would be determined by $W(\mathbf{r})$:

$$\langle |T(\mathbf{f})|^2 \rangle = T_0^2(\mathbf{f}) \quad (7)$$

where

$$T_0(\mathbf{f}) = B^2 \int W(\mathbf{r}) W(\mathbf{r}-\lambda\mathbf{f}) d\mathbf{r} \quad (8)$$

is the MTF for a diffraction limited telescope. It can be seen that T_0 is a maximum for $f = 0$ and is zero for $f > D/\lambda$. For a circular aperture and for $f < D/\lambda$

$$T_0(f) = (2/\pi) [\cos^{-1}(\lambda f/D) - (\lambda f/D) (1 - (\lambda f/D)^2)^{1/2}] \quad . \quad (9)$$

The central obscuration modifies the form of $T_0(f)$. Several examples are shown in Fig. 1.

The statistics of $U(\mathbf{r})$ must be known in order to account for the effects of the atmosphere. The greater the correlation length of $U(\mathbf{r})$, the greater is the MTF at high frequencies.

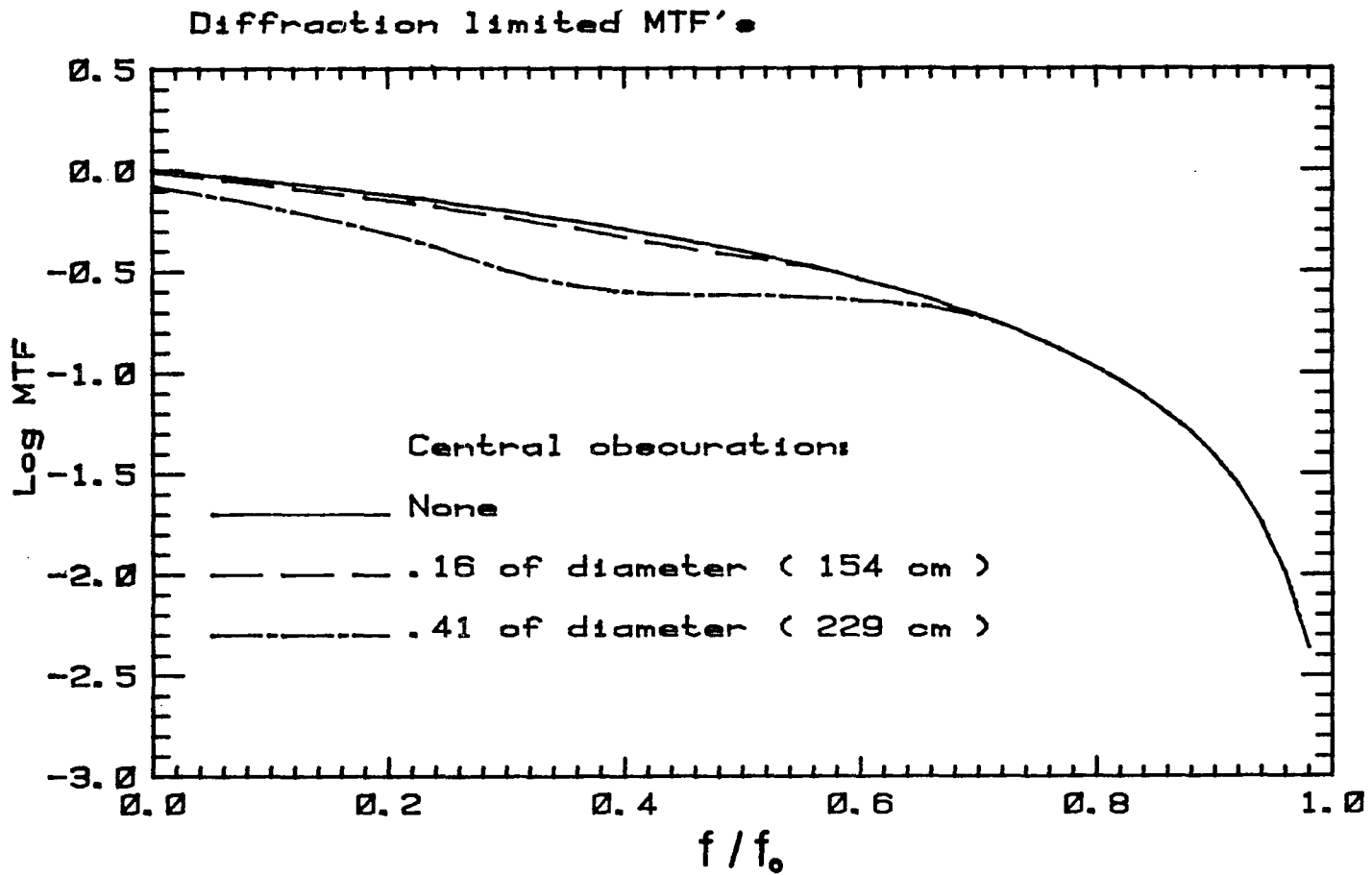


Fig. 1. Diffraction limited MTF. -- The MTF is shown for a circular aperture and also for the 154 cm and 229 cm telescopes.

Atmospheric Turbulence

"Seeing" is caused by random fluctuations in the temperature and the index of refraction of the atmosphere above the telescope. If the index of refraction is written as $N = 1 + n$ where $n \ll 1$ then the quantity that is used to characterize the atmosphere is

$$D_n(|\mathbf{r}_1 - \mathbf{r}_2|) = \langle [n(\mathbf{r}_1) - n(\mathbf{r}_2)]^2 \rangle . \quad (10)$$

Numerous observations (Tatarski 1971) have shown that for the distance scales of interest here, the turbulence is isotropic and shows only a slow z dependence. It is characterized by a Kolmogorov spectrum:

$$D_n(r) = C_n^2 r^{2/3} \quad (11)$$

where C_n^2 is called the refractive-index structure constant. Fig. 2 shows a plot of C_n^2 versus altitude taken from Fried (1979).

Atmosphere Degraded MTF

To describe the variations of the wavefront $U(\mathbf{r})$ it is common to express it as

$$U(\mathbf{r}) = U_0(\mathbf{r}) \exp [i \Psi(\mathbf{r})] \quad (12)$$

where

$$\Psi(\mathbf{r}) = \phi(\mathbf{r}) + i l(\mathbf{r}) . \quad (13)$$

Both the phase shift $\phi(\mathbf{r})$ and the log amplitude $l(\mathbf{r})$ are found to be gaussian random variables (Sibille et al. 1979, Fried 1979). The quantities of interest are the structure functions of $\Psi(\mathbf{r})$, $\phi(\mathbf{r})$, and $l(\mathbf{r})$,

$$D_\Psi(\mathbf{r}_1 - \mathbf{r}_2) = \langle [\Psi(\mathbf{r}_1) - \Psi(\mathbf{r}_2)]^2 \rangle . \quad (14)$$

D_l and D_ϕ are defined similarly. There are two general cases. For the

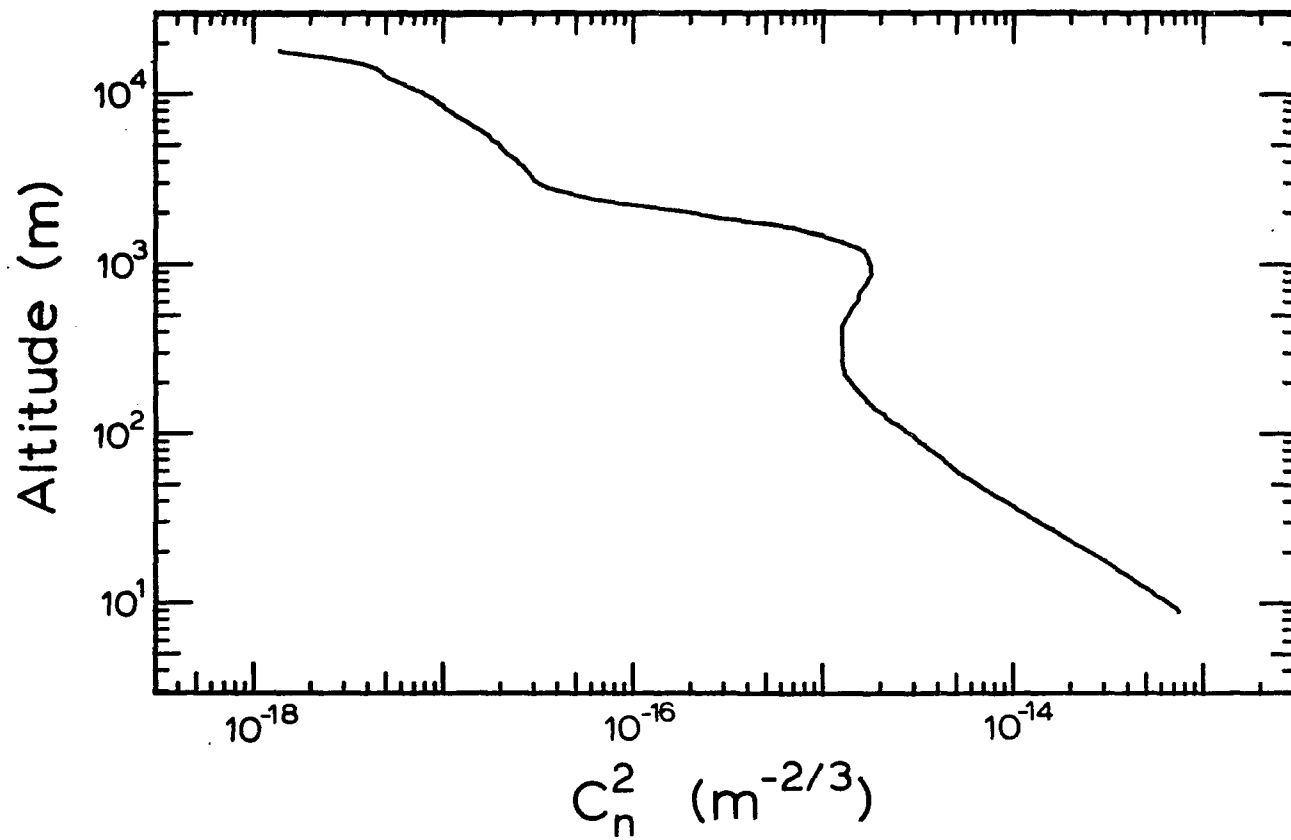


Fig. 2. Refractive index structure constant. -- The data are from Greenwood as reported in Fried (1979).

far field case, (for separations much less than λL , where L is the distance to the region of turbulence)

$$D_1 \approx D_\phi \approx 1/2 D_\psi \quad (15)$$

However for speckle interferometry the spatial frequencies of interest correspond to separations much greater than λL and in this near field case

$$D_\psi \approx D_\phi \gg D_1 \quad (16)$$

This means the primary effect of the turbulence is to introduce phase irregularities rather than amplitude changes. If $k = 2\pi/\lambda$ then the phase structure function is given by

$$D(r) = 6.88 (r/r_0)^{5/3} \quad (17)$$

where

$$r_0 = [0.42 k^2 \int_0^L C_n^2(z) dz]^{-3/5} \quad (18)$$

Note that r_0 is proportional to $\lambda^{6/5}$. For long exposures the resolution obtained is just that which would be achieved with a telescope of diameter r_0 . Korff shows that

$$\langle |T(\mathbf{f})|^2 \rangle = C \int d\mathbf{r} \int d\mathbf{r}' W(\mathbf{r}-\lambda\mathbf{f}) W(\mathbf{r}) W(\mathbf{r}') W(\mathbf{r}'-\lambda\mathbf{f}) Q(\Delta\mathbf{r}, \mathbf{f}) \quad (19)$$

where

$$Q(\Delta\mathbf{r}, \mathbf{f}) = \exp - [D_\phi(\lambda\mathbf{f}) + D_\phi(\Delta\mathbf{r}) - 1/2 D_\phi(|\Delta\mathbf{r}+\lambda\mathbf{f}|) - 1/2 D_\phi(|\Delta\mathbf{r}-\lambda\mathbf{f}|)] , \quad (20)$$

$\mathbf{r} = \Delta\mathbf{r} - \mathbf{r}'$, and C is a normalization constant chosen so that $\langle |T(0)|^2 \rangle = 1$. The equation for $\langle |T(\mathbf{f})|^2 \rangle$ must be integrated numerically. Fig. 3 shows $\langle |T(\mathbf{f})|^2 \rangle$ for the Steward 229 cm telescope at several values of D/r_0 . For the limiting cases of high and low spatial frequencies the results can be derived analytically.

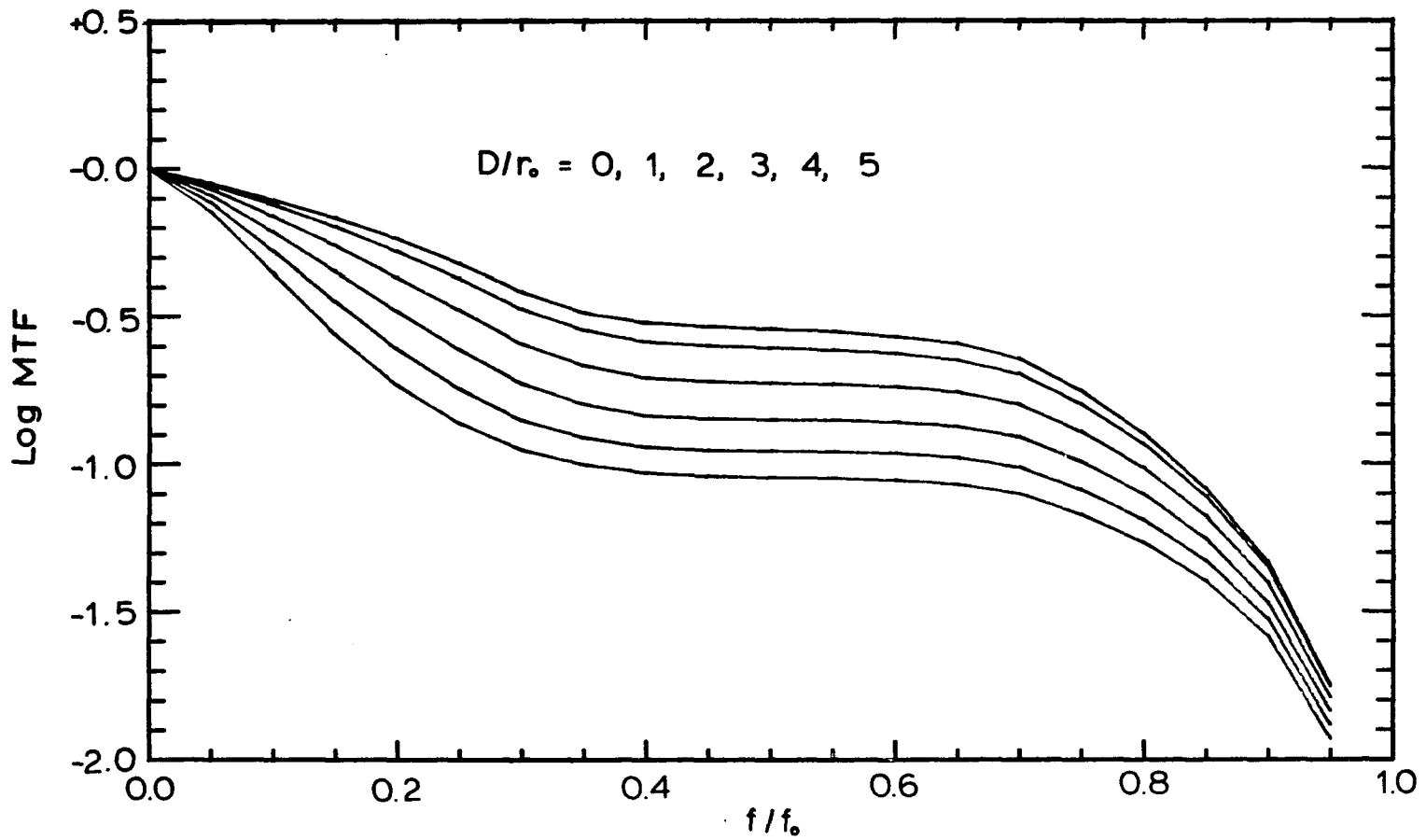


Fig. 3. Atmosphere degraded MTF. -- The MTF is shown for the 229 cm telescope under various seeing conditions.

The MTF for high frequencies. For those frequencies where $\lambda f \gg r_0$ the aperture can be divided into regions of size r_0 between which $U(\mathbf{r})$ is uncorrelated. At a given spatial frequency there will be $N = (D/r_0)^2 T_0(f)$ pairs of regions contributing components of random phase. Therefore for those f where N is large ($r_0/\lambda \ll f < (D-r_0)/\lambda$) the amplitude of the "fringes" will add as $N^{1/2}$ and the power as N . When normalized to give unity at zero frequency:

$$\langle |T(\mathbf{f})|^2 \rangle = 0.436 (r_0/D)^2 T_0(\mathbf{f}) \quad . \quad (21)$$

This is the approximation that is commonly used in visible speckle work. However, in the infrared r_0 can become comparable to D and therefore the assumption that N is large begins to break down. Therefore it is necessary to use the exact expression.

Constraints on System Parameters

The above discussion relies upon four assumptions: the radiation is monochromatic, the exposures are short enough to freeze the seeing, the various parts of the image are viewed through the same part of the atmosphere, and the wavefront errors from telescope aberrations are less than those from seeing. For the speckle system to work these conditions must be approximately met. They place constraints on the wavelength bandpass, the exposure or scan time, the image size, and the telescope image quality.

Wavelength Bandpass

For visible wavelengths, observers have determined that bandpasses on the order of hundreds of Angstroms or less are needed. For the infrared these constraints can be relaxed considerably. There

are two considerations: differential refraction, and temporal incoherence caused by the atmospheric path length changes.

Differential refraction. The differential refraction must be much less than the Airy disk of the telescope. The refraction of the atmosphere in arcseconds is given by

$$\theta_r = (N-1) 206265 \tan(z) \quad (22)$$

where N is the index of refraction and z is the zenith distance. The differential refraction is given by

$$d\theta_r = d(N-1)/d\lambda 206265 \tan(z) d\lambda . \quad (23)$$

Since the dispersion is proportional to $1/\lambda^3$ and the Airy disk is proportional to λ the permissible bandwidth increases as λ^4 . The values for $R_o(\lambda)$ in Allen (1963 p. 119) show that although the broadband visible dispersion is greater than 1", for the K filter at 2.2 microns it is less than 0.02" at a zenith angle of 45° . Therefore the dispersion is significant only for large zenith angles. For the longer wavelengths it is even smaller.

Temporal coherence. The atmosphere introduces path length changes on the order of $D\theta_s$ where again θ_s is the size of the seeing disk. For the speckles of various wavelengths to be coincident the coherence length $\lambda^2/\Delta\lambda$ must be greater than this. Therefore

$$\Delta\lambda < \lambda^2/(D \theta_s) . \quad (24)$$

The values recommended for various wavelengths are listed in Table 1 of chapter 3 along with the other characteristics of the filters.

Exposure Time

The image must be obtained in a time short enough that the wavefront distortion does not change significantly. This time depends not only on r_0 but also on the wind speed. It is commonly assumed that the turbulence pattern is "frozen" into the atmosphere and moves past the telescope at the wind speed. The characteristic time can then be estimated as r_0 divided by the wind speed. It therefore increases as $\lambda^{6/5}$. Exposure times of about 20 ms are used in the visible which indicates that times on the order of 100 ms should be satisfactory for the infrared. The wind speed is of course highly variable and the actual times can only be determined by experiment.

Field of View

For the above discussion to be meaningful the same MTF must apply to different parts of the image. The size of the field for which this is true is known as the isoplanatic patch. Visible measurements indicate it is a few arcseconds in diameter. The exact value is uncertain. However since it is proportional to r_0 (Fried 1979) its size in the infrared is much larger than any angles considered here.

Telescope Aberrations

In order to be able to ignore telescope aberrations the wavefront errors caused by them must be less than the errors introduced by seeing (Korff, Dryden, and Miller 1972). Since the image size of the 229 cm telescope is better than 0.5" this condition was fulfilled for all observations that are presented here.

CHAPTER 3

EQUIPMENT

The primary difference between present infrared and visible speckle systems is the fact that infrared ones obtain only one dimensional information. High sensitivity infrared imaging detectors are not available at this time. Therefore one is forced to use a single detector or at most a small array of them to scan the image. To obtain information out to the telescope cut-off frequency it is necessary to sample the image at twice this frequency. It is also necessary to sample completely across a seeing disk of size θ_s . Given the problems of centering and tracking, twice this distance is more reasonable. Therefore one must measure

$$N = 4 \theta_s D / \lambda \quad (25)$$

samples in each direction. For the 229 cm telescope in 2" seeing and at 2 microns $N \sim 40$. For two dimensions one would be forced observe $N^2 \sim 1600$ points. This cannot be done and still obtain a reasonable signal-to-noise ratio. The solution is to scan in one direction with a slit that is longer than the seeing disk and thereby measure $|i(f_x \hat{x} + 0 \hat{y})|$.

Design Goals

Photometer-Like Design

We felt that our speckle system should maintain the advantages of the IR photometry systems that are available at Arizona. For long wavelengths where the dominant noise comes from the thermal background

it is best to operate at the Cassegrain focus of a telescope designed for low background (Rieke and Low 1974). This is done by using a telescope with an undersized secondary and a small central obscuration, or at least optics designed so that the detector does not see the obscuration. Also, using the secondary to scan the object greatly reduces the changes in background which must be subtracted to find the true signal.

For short wavelengths the dominant noise source is either the detector's Johnson noise or noise from the preamp. Rieke et al. (1980) have developed very low noise helium cooled InSb detectors and one they built for the Steward FTS was made available for this project.

Good Seeing Conditions

Good seeing is crucial to the success of speckle interferometry not simply because it results in a higher MTF and therefore higher signal-to-noise ratio. More important is the fact that poor seeing is accompanied by variable seeing. Small changes in r_0 between the observation of the object and the point source can cause large errors at the higher spatial frequencies. Even in good seeing the observations must be repeated several times in order to establish the accuracy of the result.

Others have made speckle observations in daytime because of telescope availability. However night observing allows much better seeing conditions. Our original tests were done at the 154 cm telescope on Mt. Bigelow, a site noted for its good seeing. The later work

was done at the 229 cm telescope on Kitt Peak. Several of those nights had better than 2" seeing and at times better than 1".

Real Time Data Processing

The experience gained with the Michelson system has shown that real time processing is important. This is especially true with the speckle work because seeing changes can cause the repeatability to be poor even though the signal-to-noise ratio of a single observation is high.

It is also important to be able to change the observing program as new results are obtained. For example if an object is resolved at one wavelength, observations at other wavelengths may be useful. If it is not resolved there may be little point in collecting further data. A different example is W3 IRS 5. Our observations confirmed that it was double and because we knew this immediately we were able to observe it with a different scan direction and determine its position angle.

Control of Scan Direction

In addition to double stars several objects are known to be asymmetric (McCarthy et al. 1978). Therefore it is important to have some control over the scan direction. With the above telescopes the scanning could be either in right ascension or declination. Intermediate values would be useful and could be added in the future with some changes to the secondary mirror mounts.

The Optical System

The speckle interferometer was designed to work at the Cassegrain focus of the 154 cm and 229 cm telescopes of the University of Arizona. Some tests made at the former are discussed below. However all observations presented here were made at the latter. Both telescopes have $f/45$ secondaries which can, after some modifications, be used for scanning. The central obscuration of the 154 cm telescope is 0.16 times the diameter of the primary while the obscuration of the 229 cm telescope is 0.41. For the latter telescope a small mirror is mounted on the center of the secondary so that the detector sees the sky rather than the warm central structure.

The Michelson spatial interferometer is used as the photometer with the stage that holds the interferometer optics folded out of the way. The beam from the telescope is reflected from a dichroic mirror and into a side looking dewar. The visible light which passes through the dichroic is brought to a focus at an eyepiece used for centering. For some observations (McCarthy and Woolf 1980) the eyepiece was replaced by a slit and visible detector in order to monitor the size and relative motion of the infrared and visible images.

Scanning System

As mentioned, we felt it best to scan with the secondary mirror. If this is not done it is necessary to add extra mirrors to the system and along with them the extra background. Both telescopes had "hard stop" chopping secondaries which used solenoids to chop between two mechanical limits.

154 cm scanner. This telescope had a mechanism that could be attached to the secondary which allowed it to scan. This was a stepping motor, screw, lever arm arrangement that was originally used for scanning planets. The speed was great enough to scan through an object in about 0.1 seconds but the minimum step size was 0.28", twice that required for operation at 2.2 microns. Nevertheless we thought this would be a good system for our first speckle tests. A significant problem was vibration of the spider caused by the stepping motor, and an even greater problem was vibration of the telescope as a whole. It is driven in RA by a stepping motor operating at 89 hz. Although the telescope clearly cannot move in discrete steps at this frequency, the stepping did excite vibrations. These appeared to change with the orientation and balancing of the telescope in a way that we were unable to determine. Despite these problems, significant information was determined for the lower spatial frequencies.

Requirements of the 229 cm scanner. This secondary had no mechanism for scanning; therefore we decided to build a servo system. It had to be build so it can be put on and removed from the chopper without removing the mirror itself or disturbing its alignment since other instruments using the chopping secondary are scheduled adjacent to the speckle observing.

Some telescopes use servo secondaries for photometry but the requirements for speckle work are considerably different. Usually the need is for fast transitions between the two positions with only moderate stability at the limits. Since the positions are sometimes separated by over one arcminute considerable power is required. For

speckle scanning the principle requirement is for smoothness rather than speed. Also since it is scanned with a triangle wave and the turn-around is not important, only a small amount of power is needed.

Construction. The critical feature of the design is the fact that there is little friction which would result in jerky motion. The moving part of the chopper is hinged on a piece of spring steel. A linear motor was built which is attached to the chopper (Fig. 4). It consists of an aluminium arm stiffened with fiberglass and mounted on the hinged section. A stack of samarium-cobalt magnets is held at the end of the arm, surrounded by a coil attached to the fixed part of the chopper. Because of the high coercive force of the SmCo_5 magnets and the low power needed, no magnetic return path is required. The position sensor is a Kaman KD2300-1SU which is mounted on the fixed part of the chopper. It senses the distance to a piece of aluminium foil cemented to the back of the mirror by measuring RF eddy current losses.

A power supply regulator and preamp are located on the "ring" of the telescope at the outer edge of the spider while the rest of the electronics are located in the control room (Fig. 5). The derivative of the position signal is used for stabilizing the loop rather than having a separate velocity sensor. The error signal is integrated with a time constant of a few seconds to prevent drift.

Scanner performance. When installed at the telescope the scanner performs adequately for all wavelengths, although some improvements would be desirable. Superimposed on the triangle wave is high frequency noise with a peak-to-peak amplitude of about 0.1" (Fig. 6). This is larger than desirable, since it is half the size of the

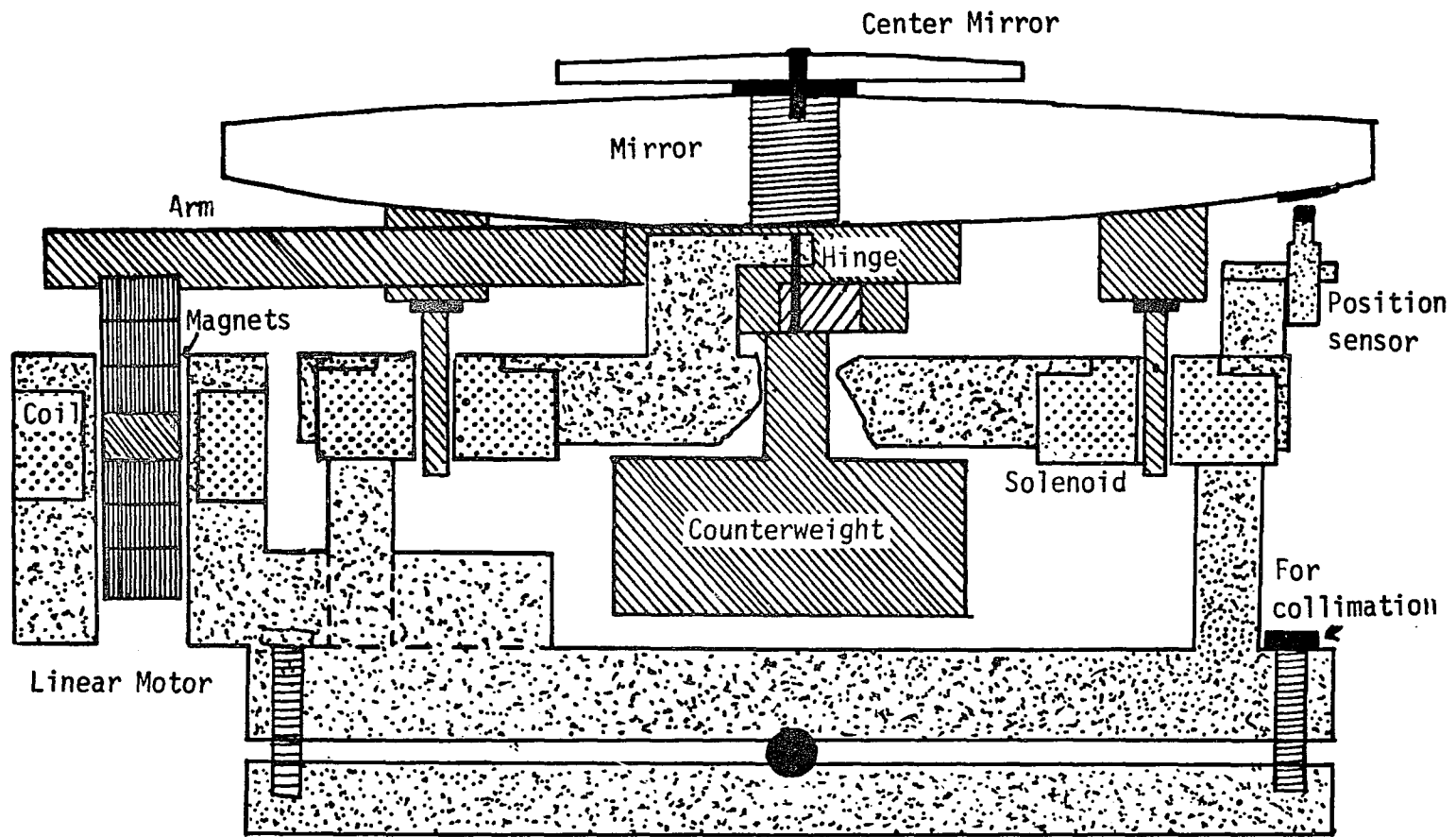


Fig. 4. The scanning secondary for the 229 cm telescope. -- This is a simplified schematic of the chopping secondary which was modified to perform linear scans.

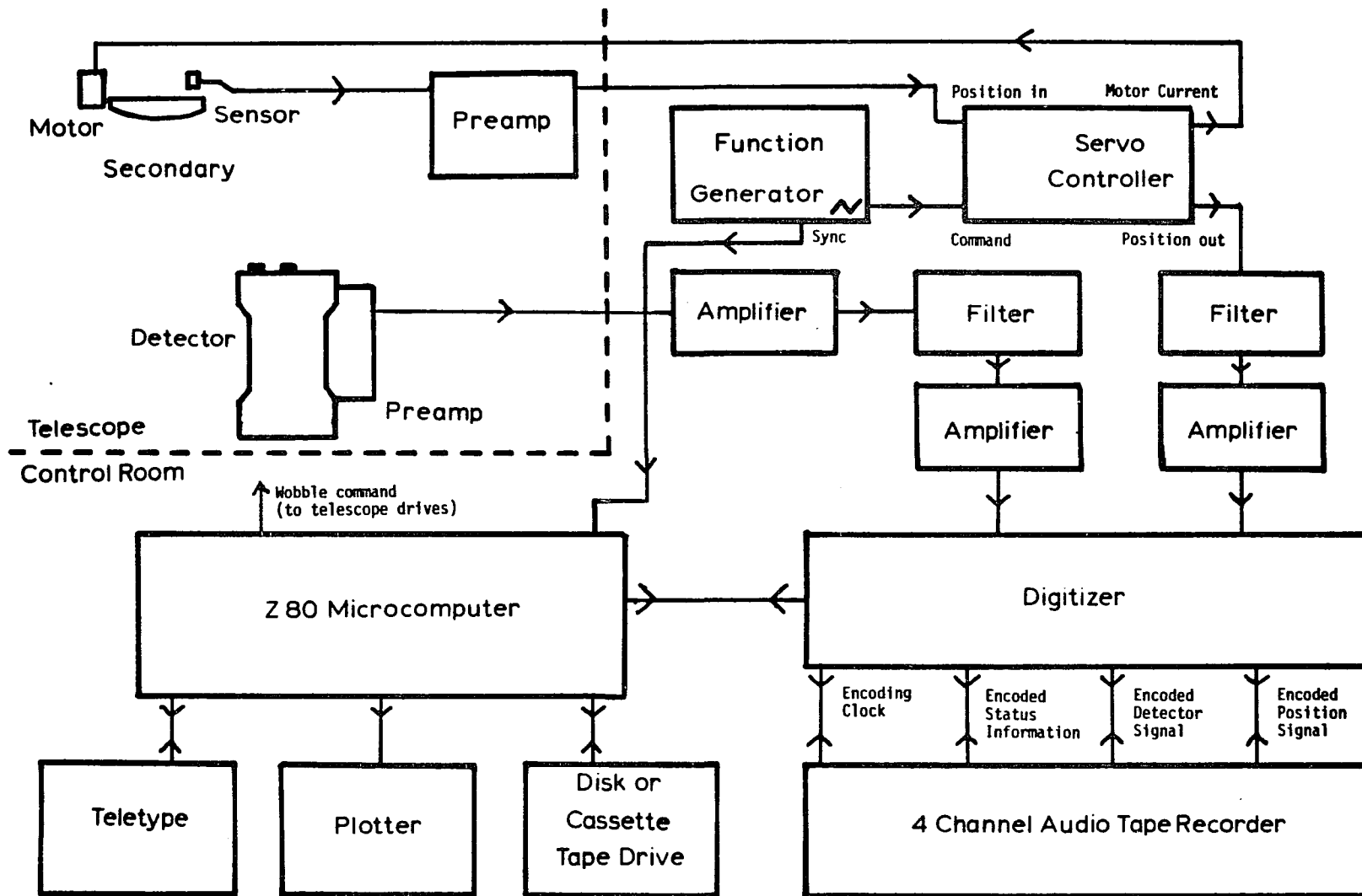


Fig. 5. Block diagram of the electronics and data system.

#605 Servo Position (Single Scan)

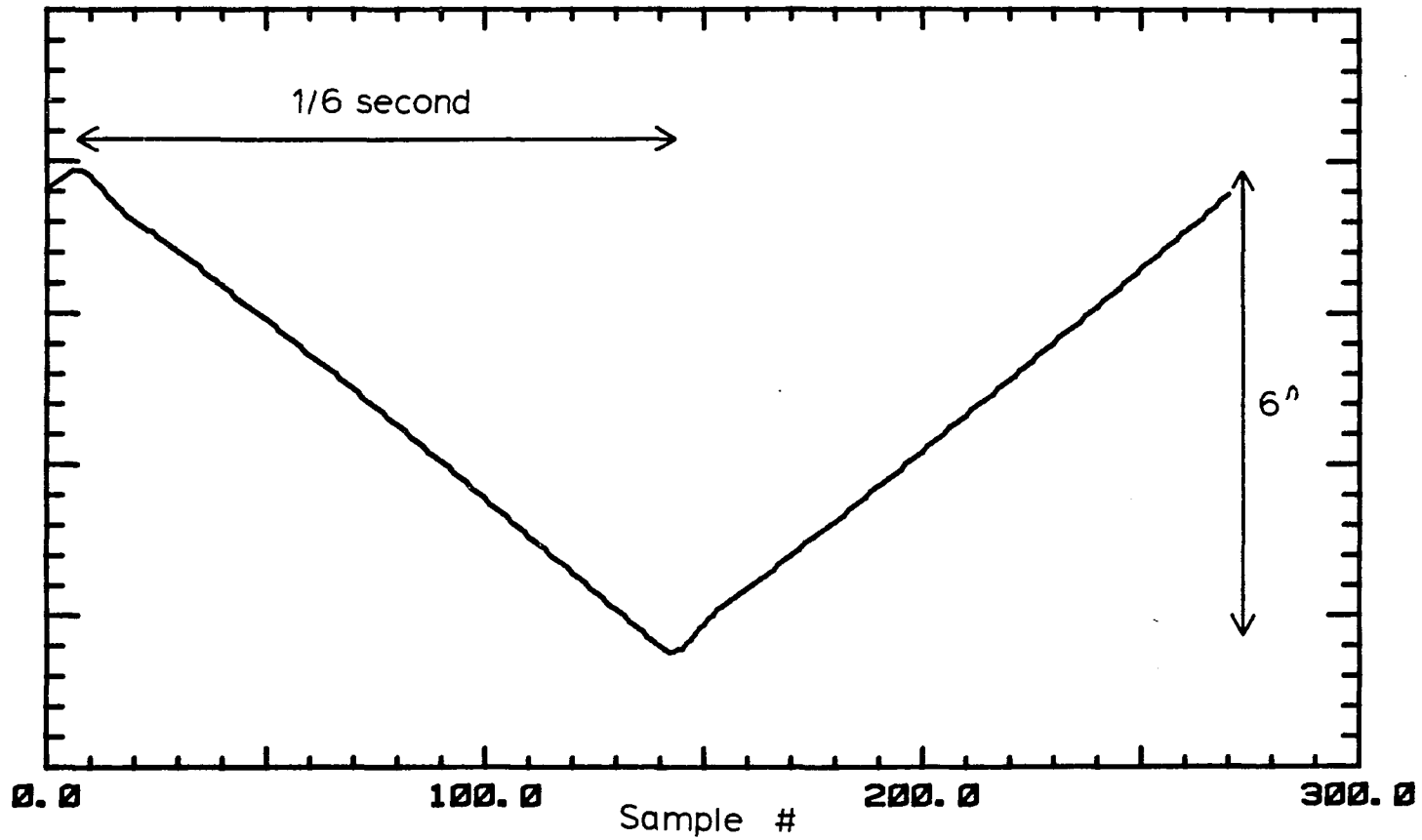


Fig. 6. The position sensor output for one scan.

smallest fringes. However the rms amplitude is considerably less and in fact the results of the speckle scans seem to indicate the noise is tolerable. The noise decreases as the gain of the servo is increased. However, as with all such servoes, this one becomes unstable at high gains. This occurs because of the phase shift between the sensed velocity and the resultant force trying to damp it. The most likely source of the phase shift is the arm holding the magnets. The gain that could be used varied somewhat from night to night.

The linearity of the scan is usually good to a few percent. In Fig. 6 the scan rate varies by about 5% over the central half but it is usually better than this. The turn-arounds at the corners of the triangle wave are not sharp, but the amplitude of the scan is large enough that only the center part occurs while on the object.

Possible improvements. The limitations of the servo result primarily from the fact that it is an add-on piece of equipment. These problems could be solved if the chopping secondary is rebuilt. For example, the motor which is located to the side of the secondary could be hidden behind the mirror. The power used is low enough that the motor is at ambient temperature but this still introduces some background. Also the new location would allow a stiffer coupling between the motor and the mirror and therefore a higher gain.

Dewar Optics and Filters

Three detectors were used: a helium cooled InSb for 2 microns, a nitrogen cooled InSb for 2 through 5 microns, and a bolometer for 8 through 12 microns. In all of these systems there is a filter slide or

wheel mounted on the cold surface along with an aperture slide or wheel which holds the focal plane slits. Table 1 gives the filter characteristics along with the maximum bandpass for coherence. All except the K and L filters meet this requirement. For these two filters there is a roll-off of the MTF at the higher frequencies. This is because the speckles of different λ are not coincident in the outer parts of the seeing disk. However for the K filter, detector noise dominates and therefore the wider bandwidth results in greater sensitivity at the lower spatial frequencies.

Behind the slit there is an off-axis Fabry mirror to form an image of the primary on the detector. This is standard practice in photometry because it improves the baffling over that provided by the cold stops in the front of the dewar. However this arrangement causes some complications when used in a speckle system.

Diffraction at the slit. The results given in chapter 2 assume that the intensity is measured in the focal plane. If this were the case then the observed $i(f)$ would be that predicted by equation 19 modified by the transfer function of the slit. That transfer function is given by

$$T_{\text{slit}}(f) = \text{sinc}(\pi f W/F) \quad (26)$$

where $\text{sinc}(x)$ is $\sin(x)/x$, W is the full width of the slit and F is the focal length. The widths of all the slits were chosen to be

$$W = F/2f_0 = F\lambda/2D \quad (27)$$

where f_0 is the limiting frequency of the telescope. Therefore

$$[T_{\text{slit}}(f)]^2 = [\text{sinc}(\frac{\pi f}{2 f_0})]^2. \quad (28)$$

Values for $T_{\text{slit}}(f)$ are listed in the last row of Table 2. The choice

TABLE 1

Filter Characteristics

Filter name	K_{He}	K_{N_2}	L	M	8	11.3	11.6*	12
Effective wavelength	2.22	2.23	3.6	5.0	8.4	11.3	11.57	12.5
Bandwidth	0.50	0.56	1.05	0.7	1.0	1.6	0.76	2.1
$\lambda^2/D\theta_s$	0.23	0.23	0.60	1.2	3.3	5.9	6.0	7.2

* The 11.3 micron filter was replaced with the 11.6 micron one after the first observing run.

$$K_1 = K_{\text{N}}$$

$$K_2 = K_{\text{He}}$$

of the width is a compromise between high $T_{\text{slit}}(f)$ near f_0 versus signal strength at lower spatial frequencies.

Although the above slit transfer function has been used by Chelli (1979) the intensity is not measured in the focal plane but rather at the detector after the light has suffered diffraction at the slit. If the diffraction were independent of the intensity pattern and direction of the incoming beam there would just be a loss of efficiency with no change in frequency response. However the diffraction depends upon both. For an exact solution it is necessary to calculate the intensity at the detector resulting from the regions at r , $r-\lambda f$, r' , and $r'-\lambda f$ on the objective. This factor would then be used in the integral in equation 19.

To simply estimate the magnitude of the effect, consider only the one dimensional problem, ignoring dependence along the direction of the slit. If the electric field comes from two entrance apertures there is a single spatial frequency and for this case the diffraction through the slit can be calculated analytically. The quantity of interest is actually the modulation of the intensity as the telescope is scanned (i.e., as the phase difference between the two apertures is changed). This modulation is given by

$$I(\theta) \propto \text{sinc} \left[\frac{k W}{2} \left(\theta + \frac{a}{F} \right) \right] \text{sinc} \left[\frac{k W}{2} \left(\theta + \frac{b}{F} \right) \right] \quad (29)$$

where the quantities are defined in Fig. 7. Basically, the intensity modulation is determined by the overlap of the diffracted beams from the two apertures.

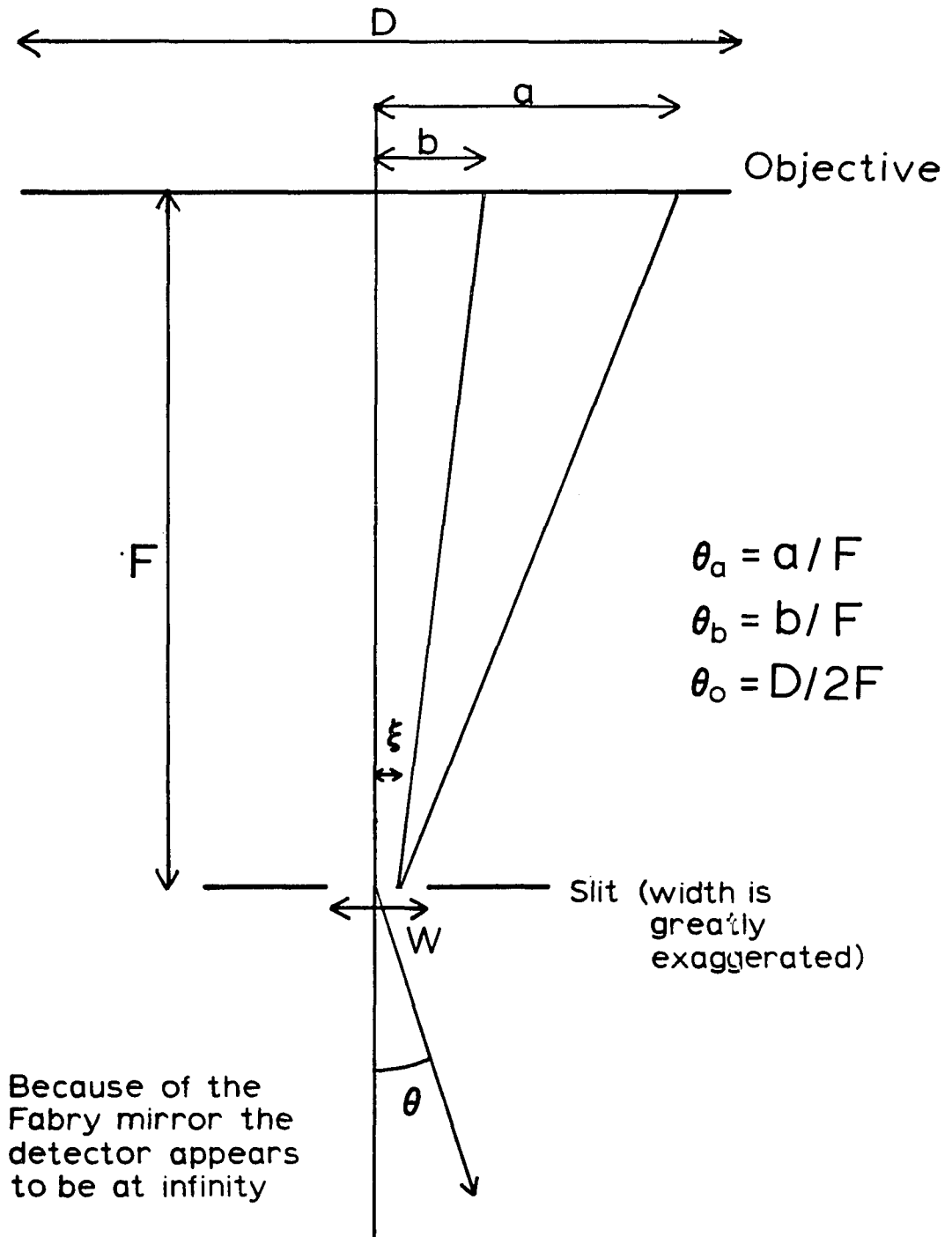


Fig. 7. Diffraction at the focal plane slit.

This intensity modulation must be integrated over the area of the detector to determine the system response. This was done for various positions of the two apertures and the results are presented in Table 2. The separation of the two apertures gives the spatial frequency. The results have been normalized to unity for the two apertures on-axis. For the on-axis case the efficiency is actually 0.47, that given by diffraction of a plane wave through the slit.

Table 2 shows the somewhat surprising result that the "transfer function" does not fall off at high frequency as fast as that for detection at the slit. This is because the diffraction is greater for the pattern that corresponds to minimum intensity at the slit. The main effect is a fall-off at the edge of the aperture since the diffracted beam is then centered on the edge of the detector. The maximum effect is less than 20% over the spatial frequencies of interest. Although this results in a different transfer function it does not effect the astronomical results because the transfer function is measured for each observation.

Detectors and Electronics

As mentioned above we have three detector systems. For 8 to 12 microns we used a gallium doped germanium bolometer with an NEP of 2.6×10^{-14} watts/hz^{1/2} when cooled to 1.2°K. However part of the time the limiting noise source was microphonics.

The N₂ cooled InSb detector was used for L and M band measurements and for a few bright objects at K. It was not "J flashed" or pumped to the N₂ triple point since it was primarily used at the

longer wavelengths. This detector uses the transconductance amplifier shown in Fig. 8. The response rolls off at high frequencies because of stray capacitance in the dewar (Fig. 9).

The third detector is the He cooled InSb one which was borrowed from the Steward FTS program. Its NEP is $\sim 2 \times 10^{-16}$. The preamp (Fig. 10) is a modified version of that used for the N_2 system. The feedback resistor is cooled to He temperature and unfortunately at this temperature it is nonlinear (i.e., it does not obey Ohms law). Therefore this dewar was designed to use capacitive feedback. Although the response is flat over the bandwidth of the FTS, the speckle interferometry requires a larger bandwidth and the response is not flat at the lower frequencies. For frequencies below $f_1 = 1/2\pi R_F C_F$ the detector is DC coupled (Fig. 11). Above this it begins to roll off and is supposedly compensated by the last stage of the preamp. If $f_2 = 1/2\pi R_2 C_2$ is chosen to equal f_1 then the response would be constant. However with the FTS dewar this is not the case, instead $f_2 = 16.8$ hz. Therefore the gain rolls off by a factor of about 4 between these two frequencies then is constant above f_2 . When necessary the reduction programs have been designed to compensate for this.

A complication was discovered after we finished the observing program. The feedback capacitance C_F shown in the diagram does not come from a discrete capacitor but from distributed capacitance in the dewar. This causes the roll-off to deviate slightly from that expected for a simple RC filter and therefore the preamp compensation is not exact. It was also found that this capacitance changed with the position of the aperture slide. Since the aperture slide did not exactly repeat in

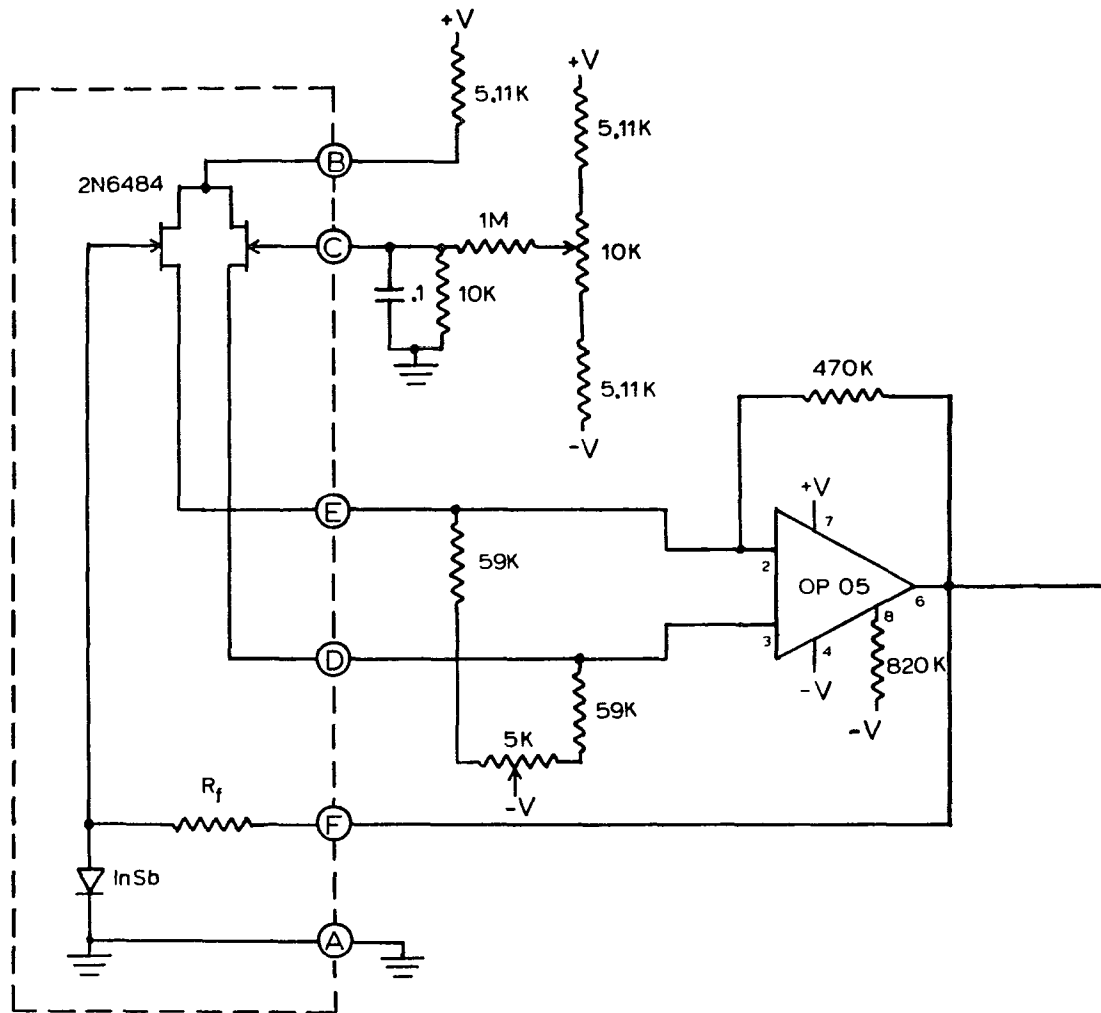


Fig. 8. The preamp for the N₂ cooled InSb detector.

Frequency response of N₂ cooled InSb detector

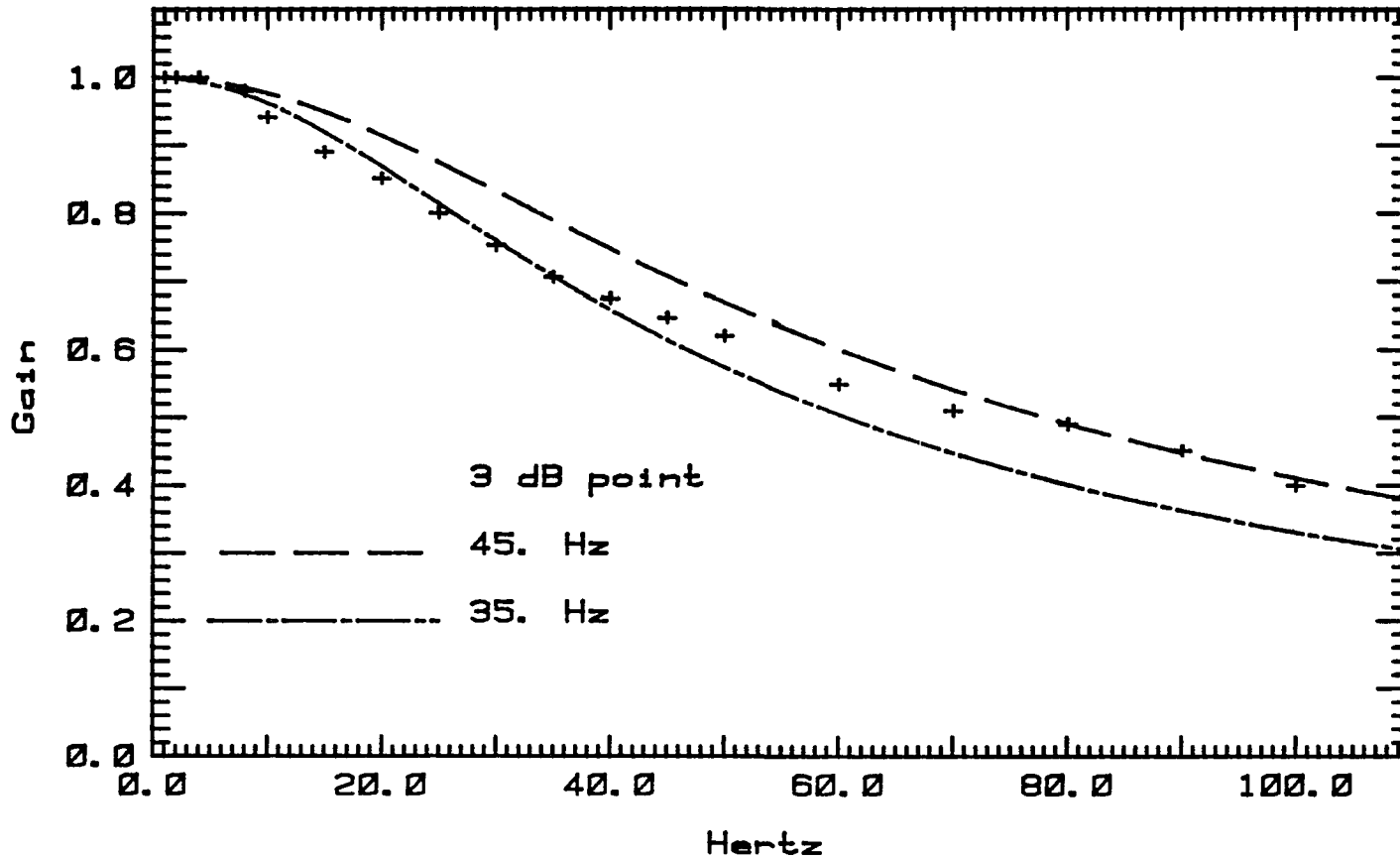


Fig. 9. The N₂cooled InSb frequency response. -- The crosses are the measurements and the two curves are the responses of single-pole filters.

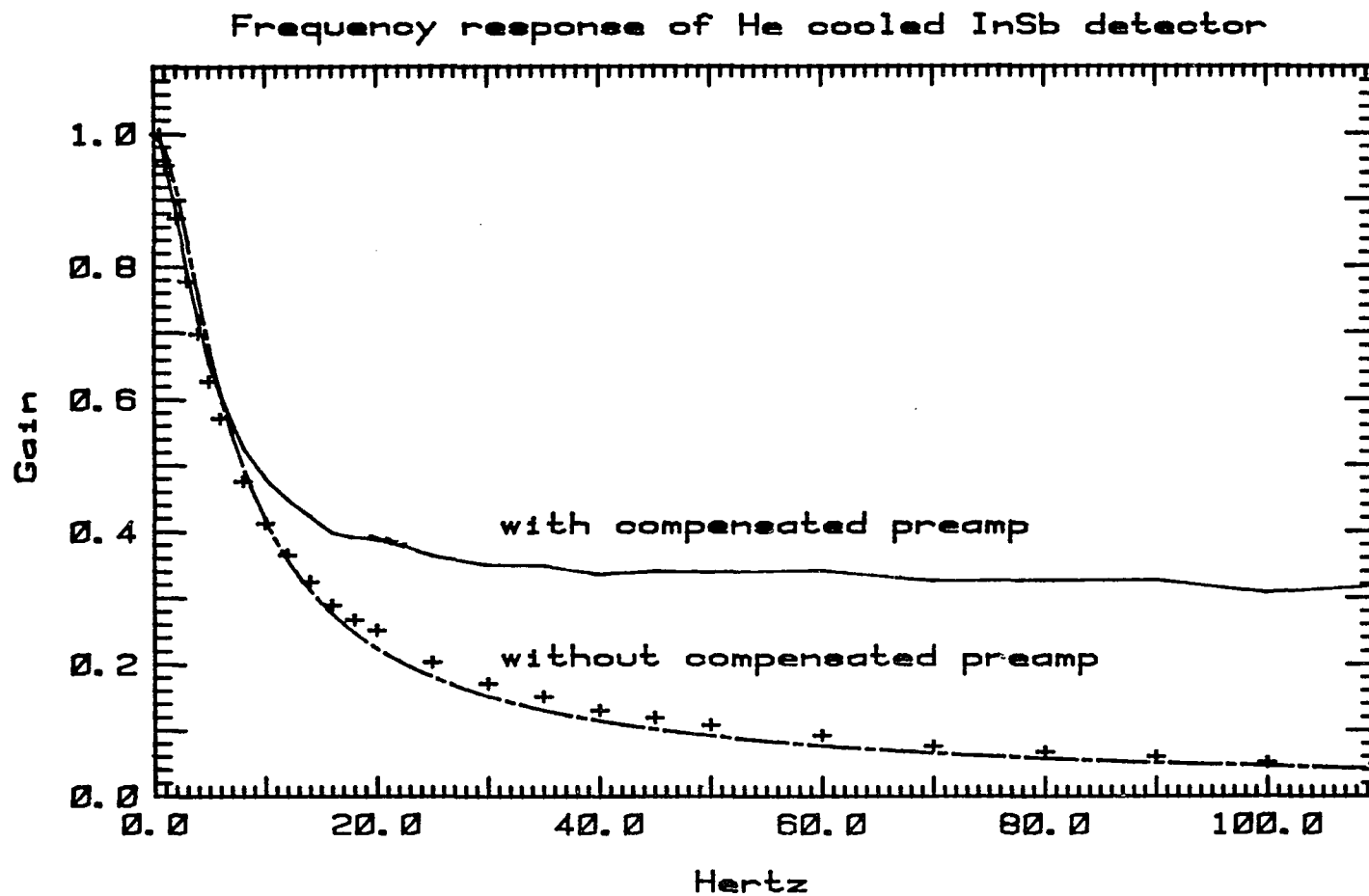


Fig. 11. The He cooled InSb frequency response. -- The crosses are the measurements and the dashed line is a single-pole filter fit to them. The solid line is the response with the compensating preamp.

position, the laboratory value of f_1 could not be used. Instead f_1 was estimated from the data itself.

The signal from the preamp is AC amplified with a cut-on frequency of 1.59 hz. For the photometry reduction it is again necessary to compensate for this. After being amplified the signal is filtered with an Ithaco model 4251. For the 229 cm telescope at 2 microns the 3db point of the filter is set to 300 hz, well above the 190 hz cutoff of the telescope. For other wavelengths a lower 3db point is used. After filtering the detector signal is digitized at 820 samples per second. Because the cut-off of the Ithaco is not perfectly sharp some power remains for a short distance above the Nyquist limit of 410 hz. This results in aliasing at the high frequencies but does not affect the ones of interest.

Data Recording and Processing

The data system used is the one originally built for the Michelson. It consists of a Z80 microprocessor running at 2.45 MHz with special hardware to perform 16 by 16 bit multiplications. The Z80 uses a Forth operating system. Most of the code is written in Forth but some high speed parts, for example the FFT, are written in assembly language. The program displays the visibility curve after each observation. The data is also recorded for later more refined processing.

The data recorder accepts two channels of analog data and digitizes them with 8 bit precision 820 times per second. This plus an 8 bit ID channel containing information such as scan direction and observation number are encoded and written on a four channel Teac tape

recorder. One of the analog channels is used for the amplified and filtered detector signal. The other is used either for the position output of the servo or for the visible light sensor.

Although the system was fairly reliable when first built it has deteriorated with time and problems in replaying the data have limited the amount of reprocessing that can be done. The most common failure mode is dropouts on the tape. This has little effect on such things as reprocessing the photometry measurements since these measure low frequencies. However the dropouts are catastrophic when attempting to Fourier transform the data to reprocess the speckle scans. Therefore it has been necessary to rely on the original real time processing.

Character of the Scans

The scanning servo is commanded by the triangle wave output of a function generator which was adjusted to give a frequency of approximately 3 hz. Therefore a scan in a single direction takes 167 ms. The amplitude is adjusted to be approximately 6" for the shorter wavelengths and twice this for the longer ones. For the short scans it takes 60 ms to scan through the seeing disk. Since the digitizer operates at 820 samples per second the scan is approximately 137 samples long.

Real Time Photometry

The brightness of the object must be known in order to normalize the visibility measurements. The electronics are AC coupled so the zero frequency point does not contain any real information and the 6 hz fundamental partially resolves the seeing disk. Therefore a small

number of scans are made before those which are Fourier transformed. The sky level is determined from the ends of these scans and the area under the center part is integrated.

Corrected Photometry

Because of the AC coupling of the amplifier and the unusual frequency response of the He InSb detector, the real time photometry has some errors. Also, it is desirable to use the same scans for the normalization and the transforms. Therefore programs were written to frequency compensate the recorded speckle scans so they have a constant response over the lower frequencies. First the scans are coadded then a recursive digital filter is used to compensate for the AC coupling. For the He InSb system the effects of the 16.8 hz treble boost are removed and a more appropriate boost frequency is applied (Fig. 12). Finally the area under the curve is computed. Since the filtering is a linear process the above procedure is equivalent to compensating the entire stream of data and then coadding.

Speckle Scans

The computer uses a sync signal from the function generator to recognize the start of a scan in a given direction and then accepts the first 128 points. A rough estimate of the sky level is subtracted and then the scan is transformed. The moduli squared of many such scans are coadded. After this the telescope is moved off the object and the process repeated, but this time the moduli squared are subtracted to remove the system noise power. Finally this result is normalized by the photometric brightness and the square root is plotted and stored. All

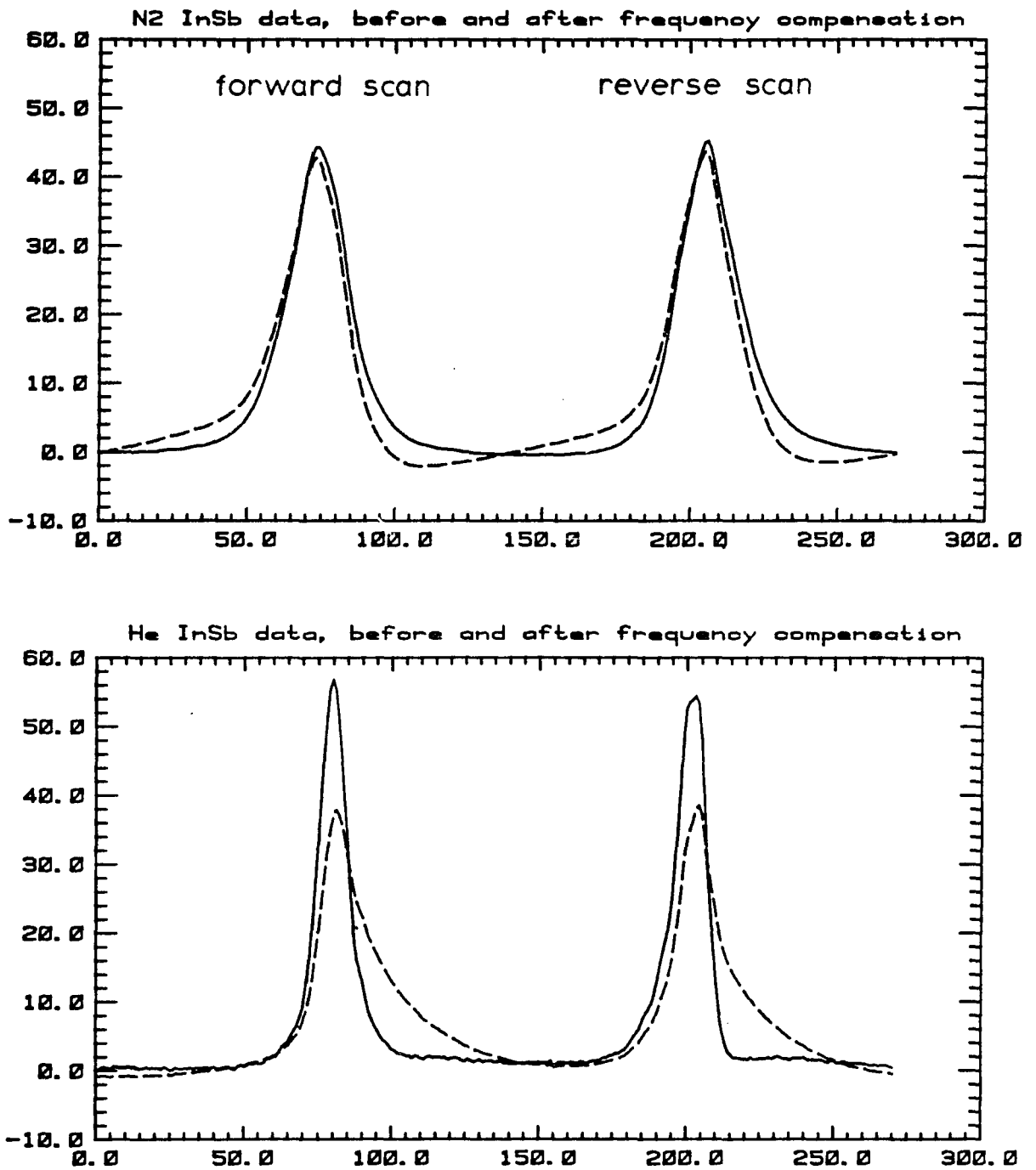


Fig. 12. The results of the digital frequency compensation. -- The dotted line shows the coadded scans before frequency compensation while the solid line shows them after it.

the scans in one direction are processed in real time. We planned to process the other direction scans from the recorded data but the problems mentioned have prevented much of that. The number of scans is varied depending upon the brightness of the object. For some there are 100 scans while for others there are 400.

The standard observing procedure is to choose a given wavelength and alternate between observations of a point source and the object of interest until consistent results are obtained. The ratio of these measurements is the visibility as defined by Michelson. The frequency compensation does not need to be applied to the power spectra themselves since this is automatically done when the data are normalized by the point source response.

CHAPTER 4

CALIBRATION AND PERFORMANCE

The following notation is used for identifying observations. Each is given a number of the form NOO or NNOO. N specifies the night while OO gives the number within that night. For example #435 represents the 35th observation on the 4th night. These numbers are listed on the visibility plots. The speckle interferometer was scheduled for 4 runs at the 229 cm telescope. Nights 1-3 are the first run, nights 4-5 the second, and nights 6-10 the third. No useful astronomical observations were obtained during the fourth run. Table 3 gives the dates of the observations.

Spatial Frequency Calibration

For each run it was necessary to calibrate the spatial frequency scale. This is equivalent to finding the distance on the sky that the scanner moves between digitizer samples. Several methods were used. The first was to calibrate the output of the position sensor by moving the telescope fixed amounts in declination as measured by the telescope encoders. The scanner then was commanded by a DC input to bring the star back to a given position in the eyepiece and the voltage output of the sensor was noted. Fig. 13 is a plot of telescope position versus scanner voltage. A least-squares fit to this gives $22.19 \pm 0.36''/\text{volt}$. The output of the position sensor was then fed into the digitizer while the scanner was running. A least-squares fit for the part of the scan

Table 3
 Dates of Observations

Observation #	UT Date	Julian Day
100	October 31, 1979	2444177.5
200	November 1, 1979	178.5
300	November 2, 1979	179.5
400	December 3, 1979	210.5
500	December 4, 1979	211.5
600	February 4, 1980	273.5
700	February 5, 1980	274.5
800	February 6, 1980	275.5
900	February 7, 1980	276.5
1000	February 8, 1980	277.5

The dates are given for 0^h UT which is 17^h Mountain Standard Time, the time at the beginning of the night.

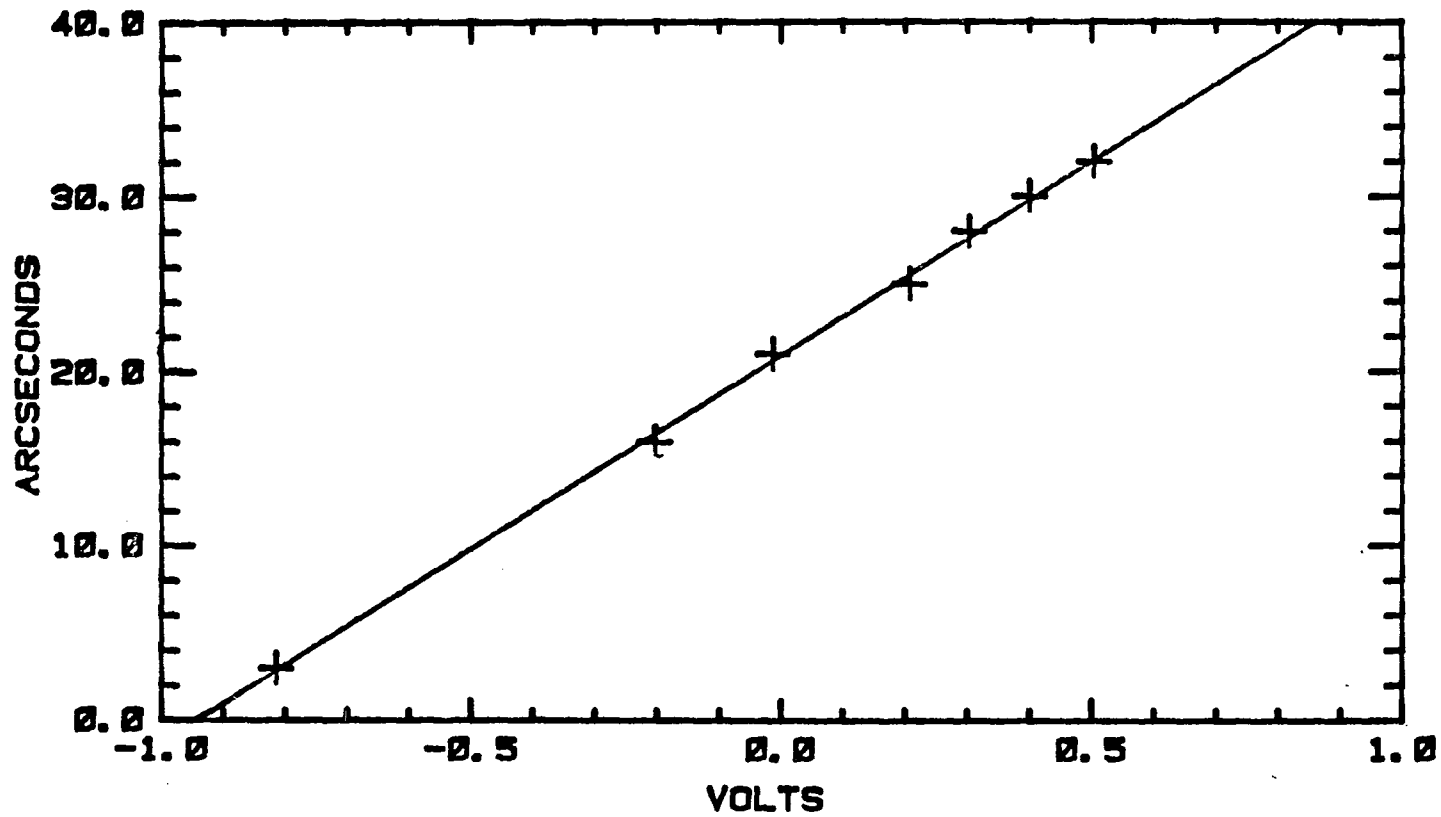


Fig. 13. Scanner angle vs. position sensor voltage. -- The line is a least-squares fit with a slope of 22.19 ± 0.36 arcseconds/volt.

coinciding with the seeing disk gives 2.160 ± 0.001 mv/sample. Together these numbers give a scan rate of 0.05762 ± 0.00078 "/sample.

An alternate method used to calibrate the system was to observe double stars of fairly wide separation with position angles close to the scan direction. There was an unexpected problem with this method. The position angles and separations for doubles published in many reference works are based upon orbits computed in the 1960's or earlier. Although the orbits are based upon over 100 years of observations this still represents a small arc for the wide doubles and thus the predicted elements are uncertain. Therefore the stars are slowly deviating from the predictions and errors of over 10% exist. Recent measurements are scarce since most of the present visible speckle work concentrates on smaller separations.

One wide double that has been measured is Alpha Psc = ADS 1615 (McAlister 1978). The measured separation for 1976.86 is $1.953'' \pm 0.011$ and the position angle is $286.6^\circ \pm 0.2$. To correct the orbit by Rabe (see Finsen and Worley 1970) the separation predicted for the date of our observations was multiplied by the ratio of the observed to predicted separation for 1976.86. The predicted position angle was increased by the difference between the observed and predicted position angle for 1976.86. Since the corrections are on the order of 10% this procedure is sufficiently accurate. For 1979.84 the separation is then $1.912''$ and the position angle is 284.5° . The east-west component of this is $1.851''$.

Fig. 14a shows the coadded and frequency compensated scans for Alpha Psc. The two peaks were each fitted with a gaussian and the

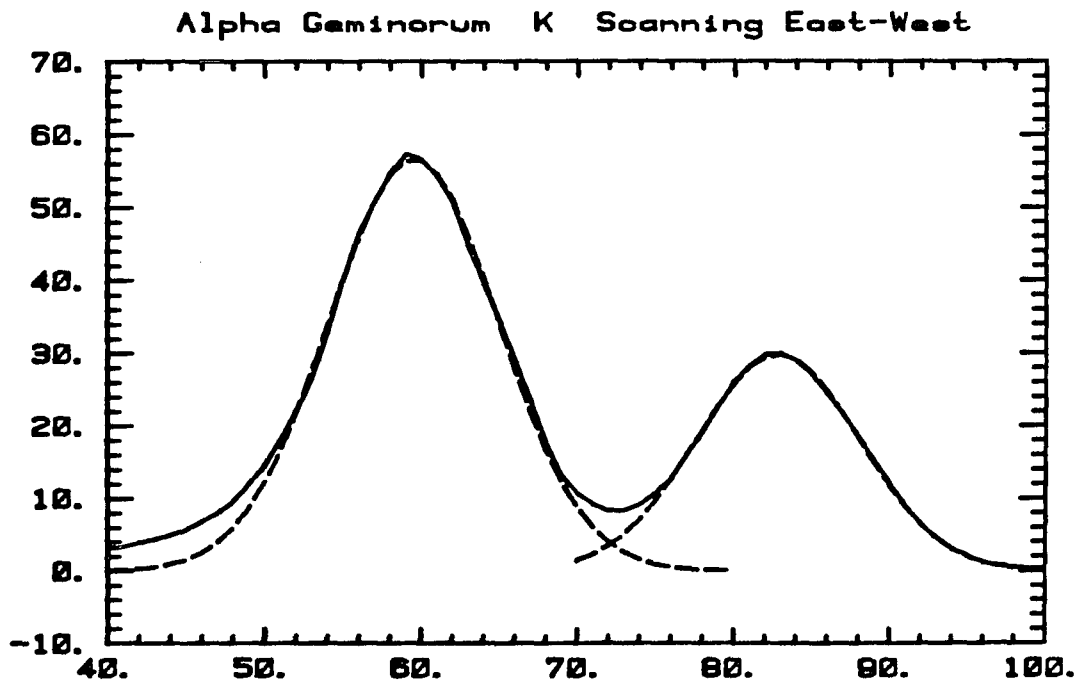
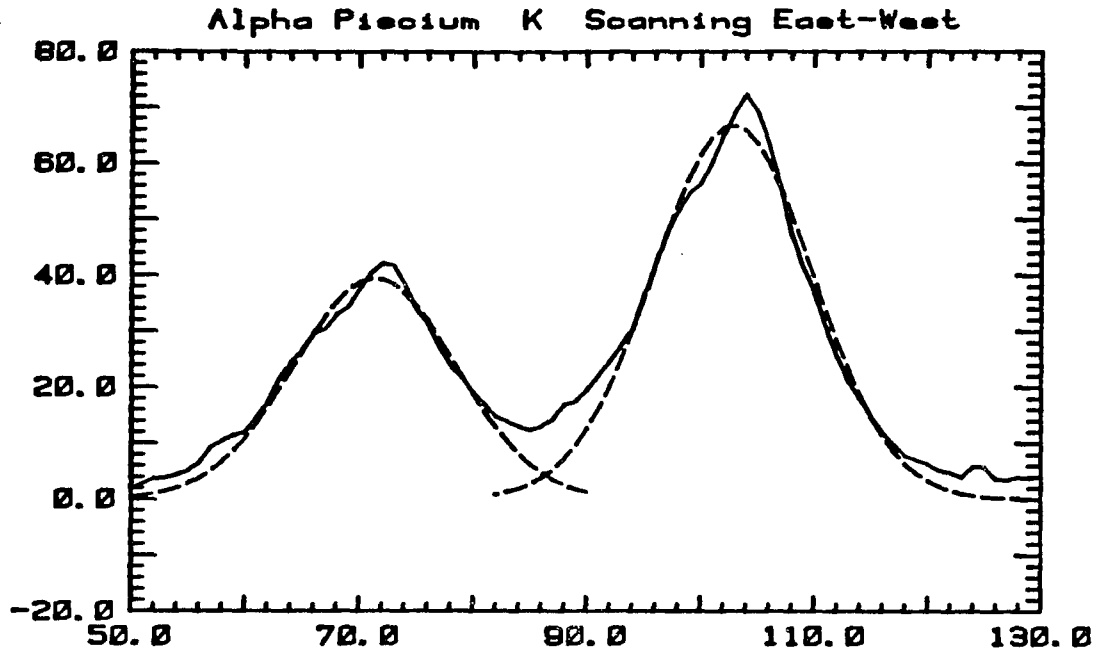


Fig. 14. Coadded scans of Alpha Psc and Alpha Gem. -- The Alpha Psc scans are slightly asymmetrical because of telescope drift during the measurement. For the Alpha Gem data the gaussian fits very well.

distance between them was found to be 31.47 ± 0.5 samples. For wide separations this is a more convenient method than using the Fourier transformed data. This separation corresponds to 0.05888 ± 0.0009 "/sample which agrees with the previous result to within the errors. The average of these, 0.05825, was adopted for this night. Since the error in the voltage calibration was primarily in the angle measurement rather than the volts/sample, the above step size was used to give 22.43"/volt. For the first run the voltage was only recorded once although it was monitored on an oscilloscope and did not appear to change. Therefore the above calibration was used throughout that run.

For the second observing run the voltage from the servo was continually recorded. During that run Alpha Gem was observed and the coadded scans are presented in Fig. 14b. The separation is 23.34 ± 0.5 samples. Using the above voltage calibration and the measured voltage/step this corresponds to 2.20 ± 0.5 ". There are two published orbits for Alpha Gem. The orbit by Muller predicts an east-west separation of 2.27" while that of Rabe predicts 2.21" (Meeus 1971a). In view of this uncertainty the voltage calibration from the first run was also used for the second run. This is equivalent to assuming an east-west separation of 2.20" for Alpha Gem.

For the third observing run (#600-#1000) some changes were made in the sensor which changed the voltage calibration. To recalibrate it Alpha Ori was observed with a double slit placed in the beam at the bottom of the interferometer mounting plate. This resulted in interference fringes with spacing of

$$a = \lambda L/S \quad (30)$$

where L is the distance from the slits to the focal plane and S is the distance between slits. In this case $L = 54.25 \pm 0.51$ cm and $S = 0.894 \pm 0.0056$ cm. The effective wavelength for a 3000 °K black-body given the filter and atmospheric transmission is 2.203 ± 0.01 microns. Therefore the fringes had a spacing of 0.01337 ± 0.00016 cm which is equivalent to $0.2687''$ given a plate scale of $2.01''$ per mm. The square root of the power spectrum is shown in Fig. 15. The peak occurs at 22.88 ± 0.30 which means $0.0480 \pm 0.0006''$ /sample or $20.65''$ /volt. The voltage was monitored for all observations and $20.65''$ /volt was used to convert to $''$ /sample. Although the calibration is good to 2% or better the nonlinearities of the scan limit the accuracy of the results to approximately 3%.

Position Angle

The position angle of the scanner is fixed by the mounting plate of the secondary and is believed to be accurate to within a few degrees. However it is still necessary to orient the slit perpendicular to the direction of the scan. This was done by first rotating the instrument approximately 90° so that the scans were along the slit. If this were exactly the case then the detector signal would rise steeply as the image moved onto the slit, remain constant as it travelled along it, and then fall steeply when it reached the other end, independent of the centering. When the angle is not correct movement of the telescope perpendicular to the slit changes the signal as shown in Fig. 16. The instrument angle was adjusted to null this effect. This could be done within $\pm 3^\circ$. The instrument was then rotated 90° so the scans were

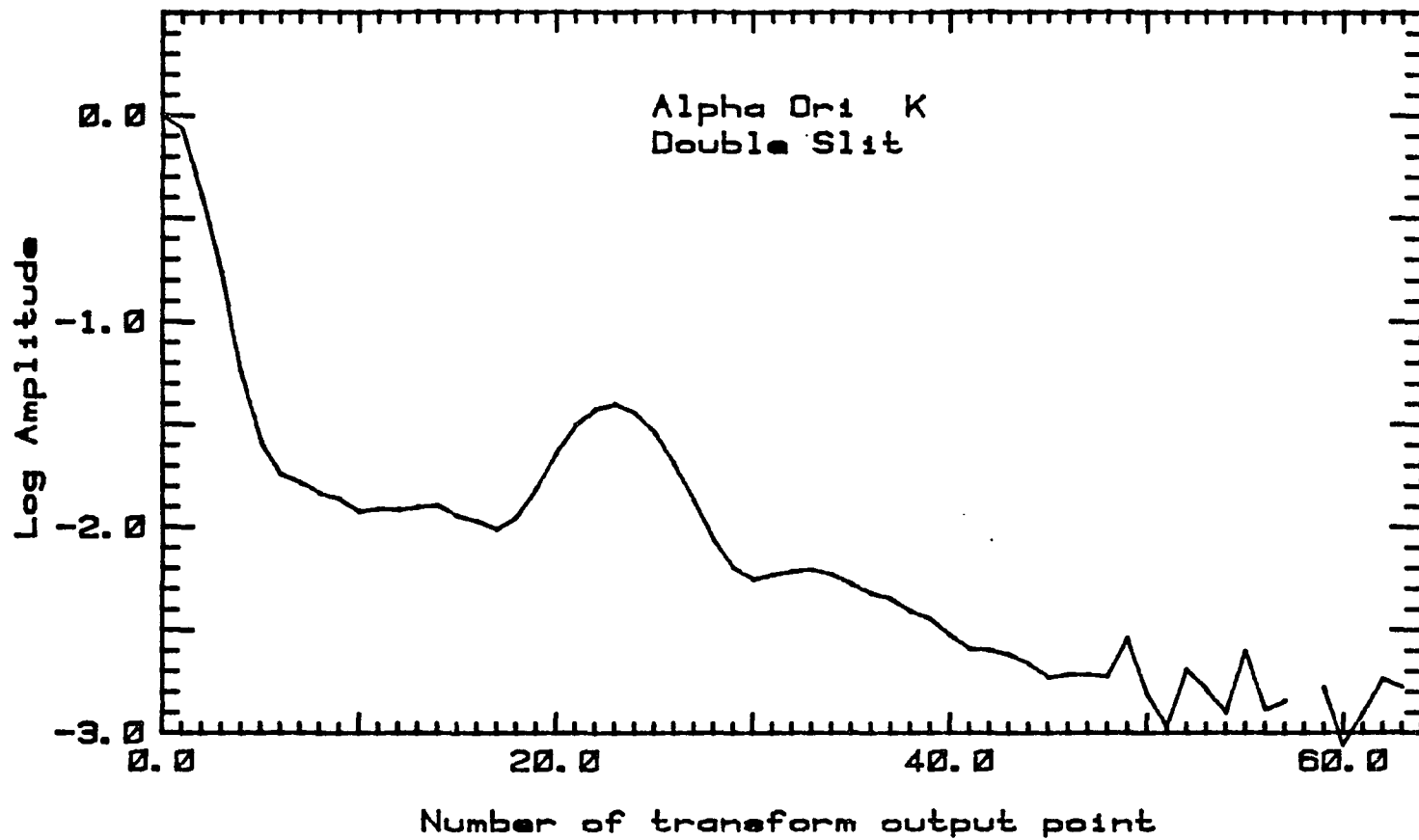


Fig. 15. Transform for a double slit. -- The square root of the power spectrum is shown. A double slit was placed in the beam to produce interference fringes of a known size in order to calibrate the scan rate.

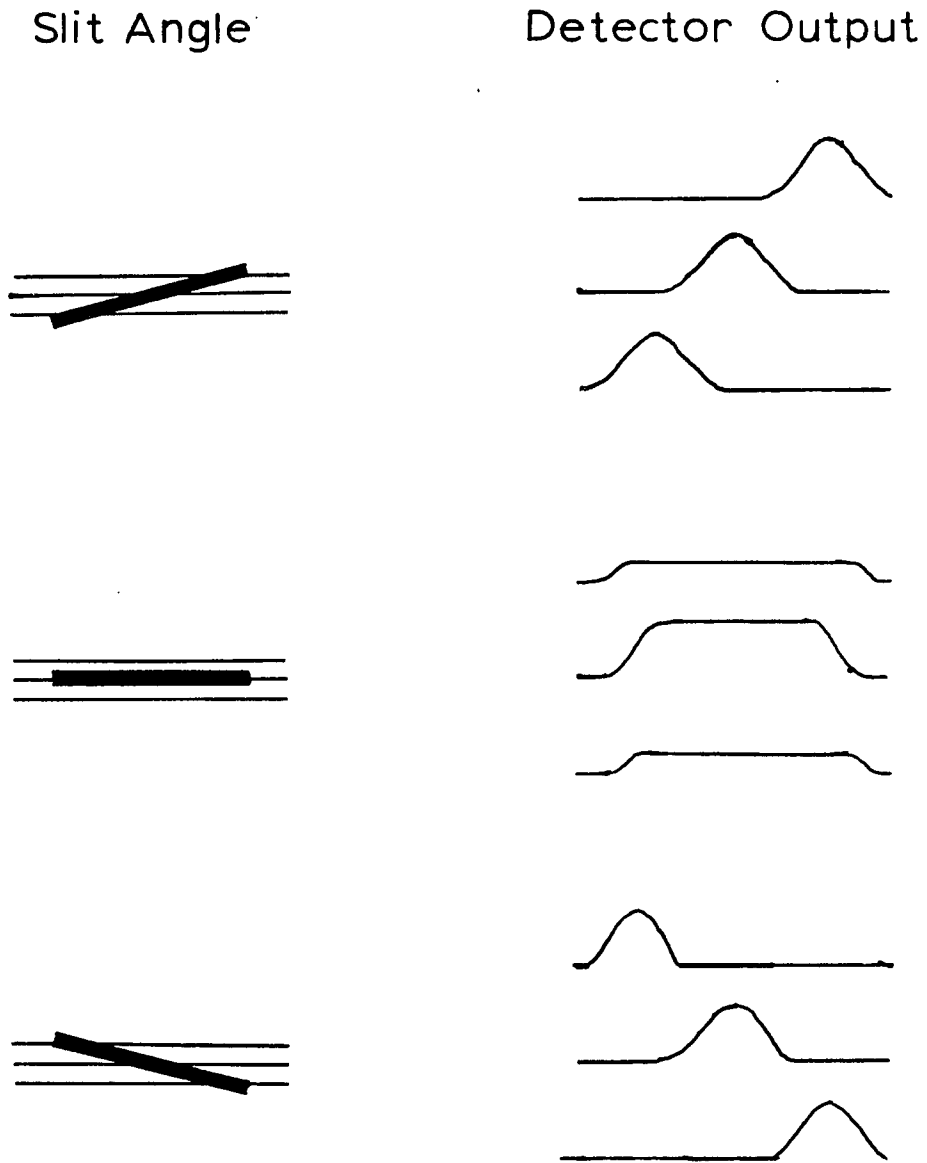


Fig. 16. Position angle adjustments. -- The detector output is shown for various slit angles as a function of the centering.

perpendicular to the slit. The final accuracy of the scanning position angle is approximately $\pm 5^\circ$.

Sensitivity

Although the responsivity and noise of the detectors can be measured in the lab, the efficiency of the entire system can only be measured at the telescope. The system responsivity is lower because of atmospheric attenuation and the extra reflections. For the longer wavelengths the noise is determined by the background. Also, excess noise can be introduced by numerous sources at the telescope.

System Responsivity

The system efficiency was measured using the N_2 cooled InSb detector since it was not subject to the frequency response effects of the He cooled InSb or the temperature dependence of the bolometer. The responsivity is $\eta(eR_f/h\nu)$ where e is the charge of an electron, $R_f = 1.6 \times 10^{10}$ is the feedback resistance, $h\nu$ is photon energy, and η is the system efficiency. The last term includes such things as filter and diffraction losses, detector quantum efficiency, and atmospheric attenuation. The responsivity was measured in the lab using large focal plane apertures and found to be 4.25×10^9 volts/watt or equivalently 0.28 amps/watt. This corresponds to $\eta \sim 0.37$ which is approximately that expected for a window transmission of 0.9, a filter transmission of 0.8, and a quantum efficiency of 0.6. With the slits in place the K and the M efficiencies fell to ~ 0.13 on axis. This is a factor of 0.35 rather than the 0.47 predicted. The extra loss is most likely caused by the aberrations of the field mirror for the larger f ratio beam.

From observations of several stars of known brightness the efficiency at the telescope was found to be ~ 0.055 at K and 0.036 at M. This additional loss can be partially explained by reflection losses at the three mirrors, the vignetting of the outer part of the beam, and atmospheric attenuation. The mirrors could cause a loss of ~ 0.85 while the vignetting would be ~ 0.9 . The objects observed were at ~ 1.2 airmasses and although the extinction was not measured reasonable values would be a transmission of 0.84 for K and 0.66 for M. When these factors are included there remains an attenuation of 0.66 at K and 0.55 at M that cannot be readily explained. The system responsivities for these filters along with those of the bolometer and He cooled InSb are listed in Table 4. These are the responsivities at 6.4 hz, the fundamental of the scan frequency. The responsivities that correspond to 0.7 of the telescope cut-off frequency are also listed.

System Noise

The noise spectra for the various detectors and filters were determined from the transforms of the sky scans and are shown in Fig. 17. Also shown are the NEP's derived from these spectra and the measured frequency response. For the K filters, detector noise dominates and the NEP is worse at high frequencies. For the M filter, the background noise dominates and the NEP is independent of frequency. The microphonics and pickup that sometimes dominated the bolometer noise can also be seen. However since the underlying noise has a $1/f$ character the NEP is actually better at higher frequencies.

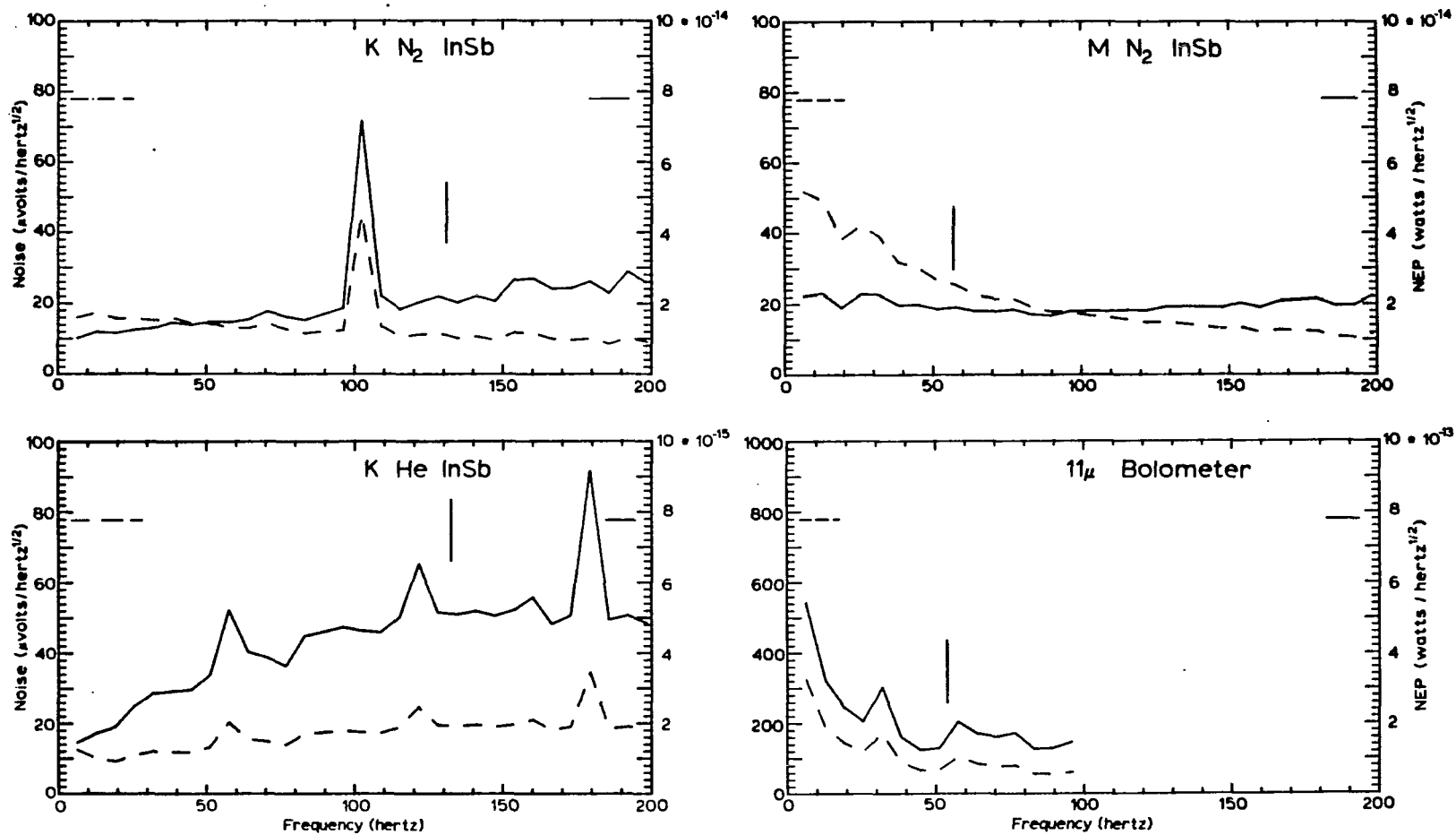


Fig. 17. Noise spectra and NEP's. -- The dashed curves are the noise spectra measured from the sky scans. The solid curves are the system NEP's determined from these spectra and the system efficiencies measured at the telescope. The vertical bars mark the $0.7 f_0$ point.

Limiting Magnitudes

The definition of limiting magnitude is somewhat arbitrary. Not only is it necessary to state the integration time and the signal-to-noise ratio required, it is also necessary to specify the spatial frequencies of interest and the seeing. The signal-to-noise ratio will drop sharply beyond 0.7 times the cut-off frequency because of the sharp drop in the MTF (Fig. 3). Therefore the limiting magnitude is defined here as that which will give a signal-to-noise ratio of 5 in the visibility at 0.7 times the cut-off frequency. Appendix A is a derivation of the signal-to-noise ratio for faint objects where detector or background noise is greater than the "noise" caused by the random nature of the speckle images. For a given spatial frequency the signal-to-noise ratio of the measured visibility is

$$\frac{1}{2} \left(\frac{F_{\lambda} \Delta\lambda A_t M \frac{W}{L}}{NEP_s} \right)^2 \sqrt{T t} \quad (31)$$

T is the integration time, t is the time for one scan, W is the slit width ($\lambda/2D$), L is the scan length, A_t is the telescope area, M is the MTF for that spatial frequency, and NEP_s is the system NEP for the corresponding temporal frequency. These magnitudes and the assumed parameters are listed in Table 4. The system efficiency would be considerably better with dewar optics optimized for speckle interferometry, so limiting magnitudes are also listed for such a system.

The actual observations agree well with these predictions. The faintest object observed at K was Mon R2 IRS 3 which is +6.5. Only the

Table 4
Limiting Magnitudes

	K_{He}	M_{N_2}	11	
$0.7 f_0$	3.5	1.5	0.67	cycles / arcsec
Noise ($0.7 f_0$)	18.	28.	< 50.	$\mu\text{volts} / \text{hz}^{1/2}$
Responsivity (6.4 hz)	8.6×10^9	2.3×10^9	$\sim 1. \times 10^9$	volts / watt
($0.7 f_0$)	3.7×10^9	1.4×10^9	$\sim 8. \times 10^8$	volts / watt
NEP _{system}	4.9×10^{-15}	$2. \times 10^{-14}$	$< 6. \times 10^{-14}$	watts / $\text{hz}^{1/2}$
W (slit width)	0.10	0.21	0.52	arcseconds
L (scan length)	6.0	6.0	12.5	arcseconds
t (scan time)	0.16	0.16	0.16	seconds
T (integ. time)	120.	120.	120.	seconds
r_0	45.	110.	281.	cm
MTF	0.1	0.16	0.2	

The limiting magnitude is defined as the flux that will give a signal-to-noise ratio of 5 at $0.7 f_0$.

Flux	4.5	20.	200.	Jy
Magnitude	5.5	2.2	-1.8	

With dewar optics which were optimized for speckle interferometry the efficiency would increase by a factor of ~ 4 . The 5 micron background would also be decreased. For 11 microns a shorter scan would be better. Given such a system the limiting magnitudes would be:

Magnitudes	7.0	4.0	0.0
------------	-----	-----	-----

low frequencies had a useful signal-to-noise ratio. At M the faintest object observed was NGC 2264 IRS which is approximately 1.3.

Systematic Errors

There are three sources of error which need to be mentioned. The first results from the high frequency noise in the scanner. This causes low spatial frequencies in the image to contribute higher frequencies to the detector output. This error is only significant for the K filter since at longer wavelengths the amplitude of the motion is much less than the highest spatial frequency present. However even at K another effect seems to dominate.

The second source of error has been pointed out by Foy et al. (1979). As they state the finite length of the scan can transfer power from low to high spatial frequencies. For stationary signals the result of many transforms is

$$\langle |i(f)|^2 \rangle = \langle |I(f)|^2 \rangle \star \text{sinc}^2(2tf) \quad (32)$$

$\langle |I(f)|^2 \rangle$ is the true power spectrum and $\text{sinc}^2(2tf)$ is the transform of the "window" function giving the length of the scan. Because the true power spectrum decreases steeply with frequency and sinc^2 is always non-negative this will transfer power from the low frequency peak out to the high frequency range.

However they ignore the fact that the image is a non-stationary signal; the statistical properties of the signal are not constant along the length of the scan. In fact for scans much longer than the seeing disk the signal is zero at the ends of the scan. The convolution theory

states that the finite transform gives the true transform convolved with the transform of the window, in this case a sinc function. However the sinc function oscillates around zero and if the true signal is zero everywhere outside the window then the convolution just reproduces the original transform. The derivation of the above equation from the convolution theorem assumes the signal is stationary. In this case that assumption is not valid.

Some explanation might be useful. For stationary signals the value at the end of the scan will in general not equal the value at the beginning. The finite Fourier transform "assumes" the signal has a period equal to the length of the scan and therefore sees the discontinuity between these two points. This effect transfers power from one frequency to another. For signals that are zero at the ends of the scan this does not occur.

Instrumental effects can however cause the signal to be nonzero at the ends. For example if the detector sees a changing background then a ramp will be superposed on the signal and this will add power which falls off as $1/f^2$. The problems which occur in our data result from a different source, namely the non-flat frequency response of the detectors and amplifiers. The frequency response causes the baseline to slope at amounts proportional to the signal. Furthermore poor centering can cause discontinuities between the end of one scan and the beginning of the next. Therefore power at high frequencies can be introduced which will fall off as $1/f^2$. This problem is worse for the He InSb than for the N_2 InSb or the bolometer. A solution would be to run the data through the compensating filters mentioned above before

transforming it but difficulties with the data recorder have made this impractical.

One way to estimate the magnitude of the effects is to examine the power spectra of point sources. These spectra should fall quickly to zero beyond the cut-off frequency of the telescope. The amount of power above this frequency is a measure of the power introduced by the above problems. Fig. 18 shows the measurements for two wavelengths. The effect is negligible for the long wavelengths. For most of the K measurements it contributes less than 10% of the amplitude out to $0.7 f_0$, however for some observations it can be quite significant. This is especially true for the first observing run where a faster scan rate was used. Beyond $0.7 f_0$ it affects most of the observations. When this occurs for the object and the point source there is a tendency for the visibility curve to approach some constant value independent of the real visibility. Those observations which are affected by this error will be noted.

The third systematic error results from a simplification in the real-time processing. When the square roots of the power spectra were computed, if the power was negative (i.e., the power was greater on the sky scans) then the result was set to zero. Because of this the averages of very noisy data sets will have a positive bias. Only a few observations were noisy enough that the measured power was negative and this will be noted when they are discussed.

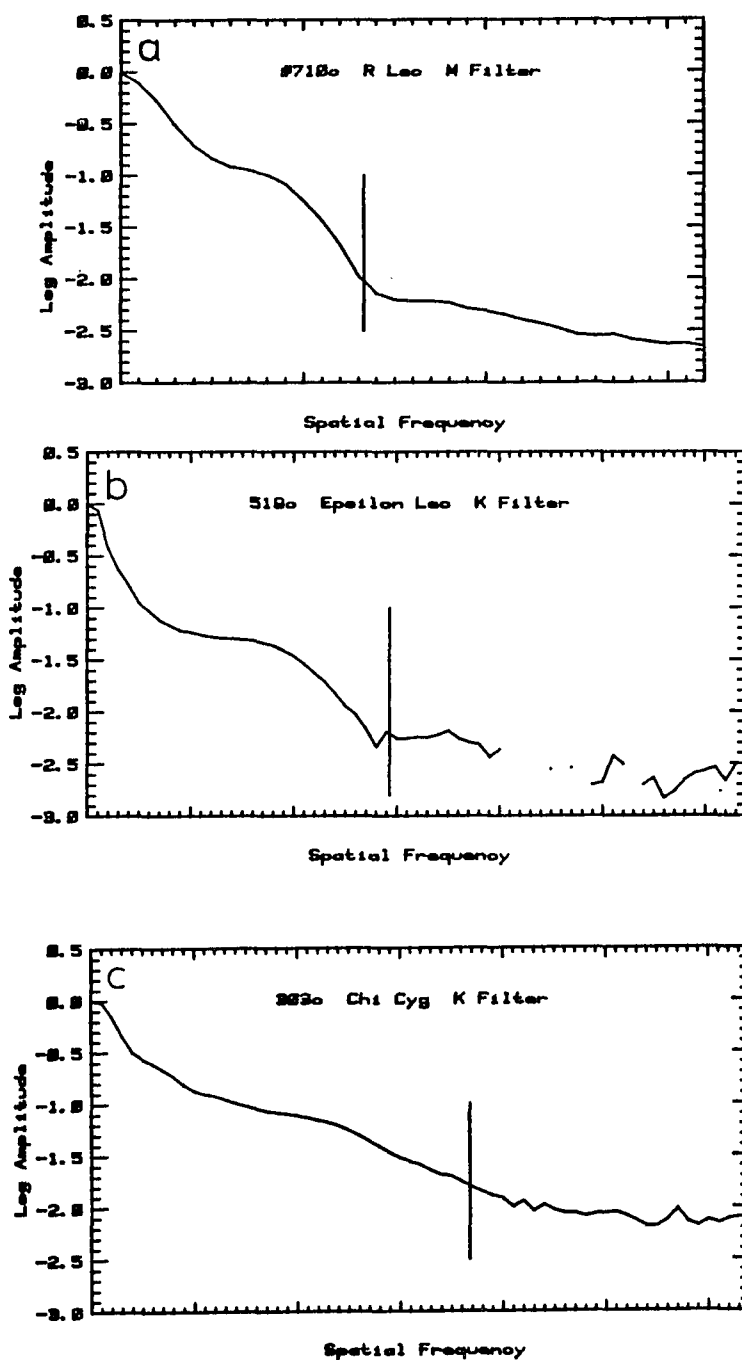


Fig. 18. Effects of the finite scan length. -- For long wavelengths (a) and for most observations at shorter wavelengths (b) the power falls off quickly beyond the limiting frequency of the telescope marked by the vertical line. However for some observations (c) instrumental effects add power at high frequencies and therefore distort the measured visibility. The curve is not plotted where the measured power is negative.

Observed MTF

Fig. 18 shows that the transforms have at least the general shape expected from the theoretical MTF. However in order to make a detailed comparison the data must be corrected for the frequency response of the detectors. This has been done in Figs. 19 and 20 which show results for the K and M filters of the N₂ cooled InSb. The first figure shows two observations taken 20 minutes apart. The differences between them are representative of the changes that can occur on this time scale. Minor differences between the observed values and the theoretical curves can be explained by the effects of the finite width of the slit and the bandwidth of the optical filters.

Test Objects

Several types of objects with known visibility curves were used to test the interferometer.

Double Stars

The visibility curve for a double star is given by

$$V(f) = \text{SQRT} \{ 1 + [2c/(c+1)]^2 [\cos (2 sf) - 1] \} \quad (33)$$

where s is the separation and c is the brightness ratio. Fig. 21 shows a measurement of Alpha Psc scanning north-south. A least-squares fit of the above equation is also shown. The differences between the two curves are primarily due to changes in the MTF between observation of the double and the point source. This shows the need for several observations of each object. The separation of 1.912" and the position angle of 284.5° derived from visible measurements correspond to a

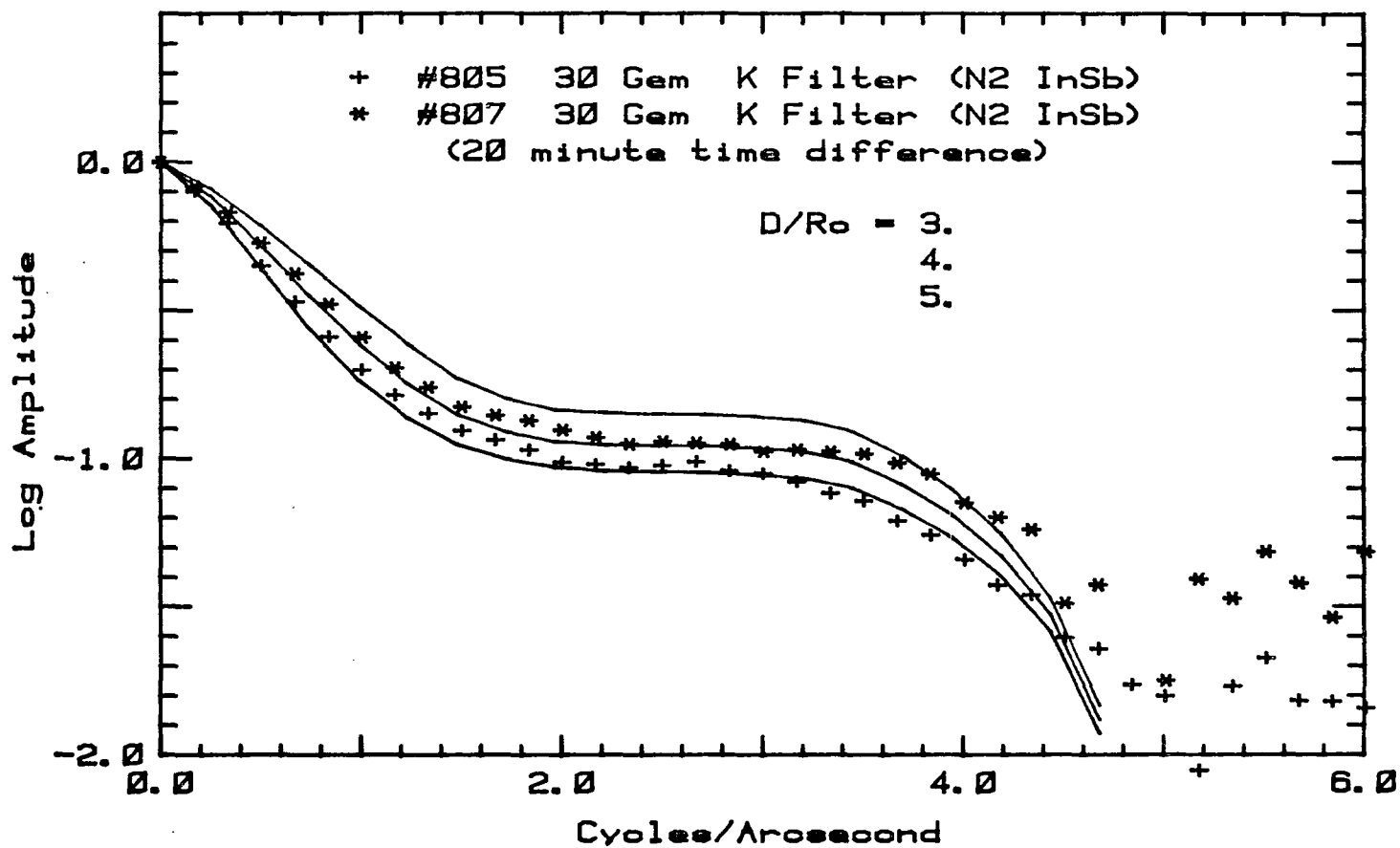


Fig. 19. Observed MTF for the K filter. -- The square root of the power spectra are shown after having been corrected for the dewar frequency response. The two sets of data were taken 20 minutes apart and are typical of the changes that can occur. The solid curves are theoretical MTF's for the indicated values of D/r_o .

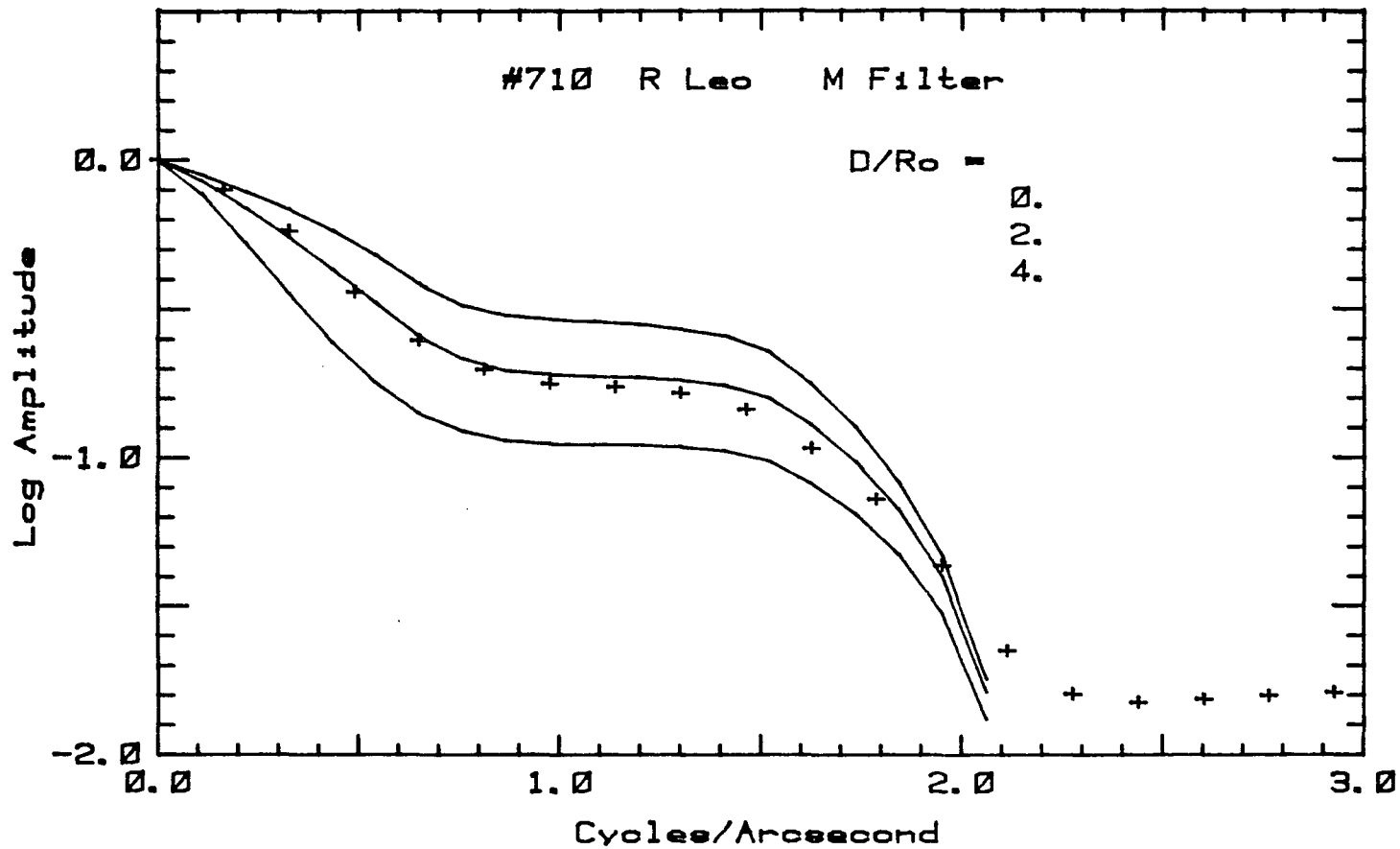


Fig. 20. Observed MTF for the M filter. — The square root of the power spectrum is shown after having been corrected for the dewar frequency response. The solid curves are theoretical MTF's for the indicated values of D/r_0 .

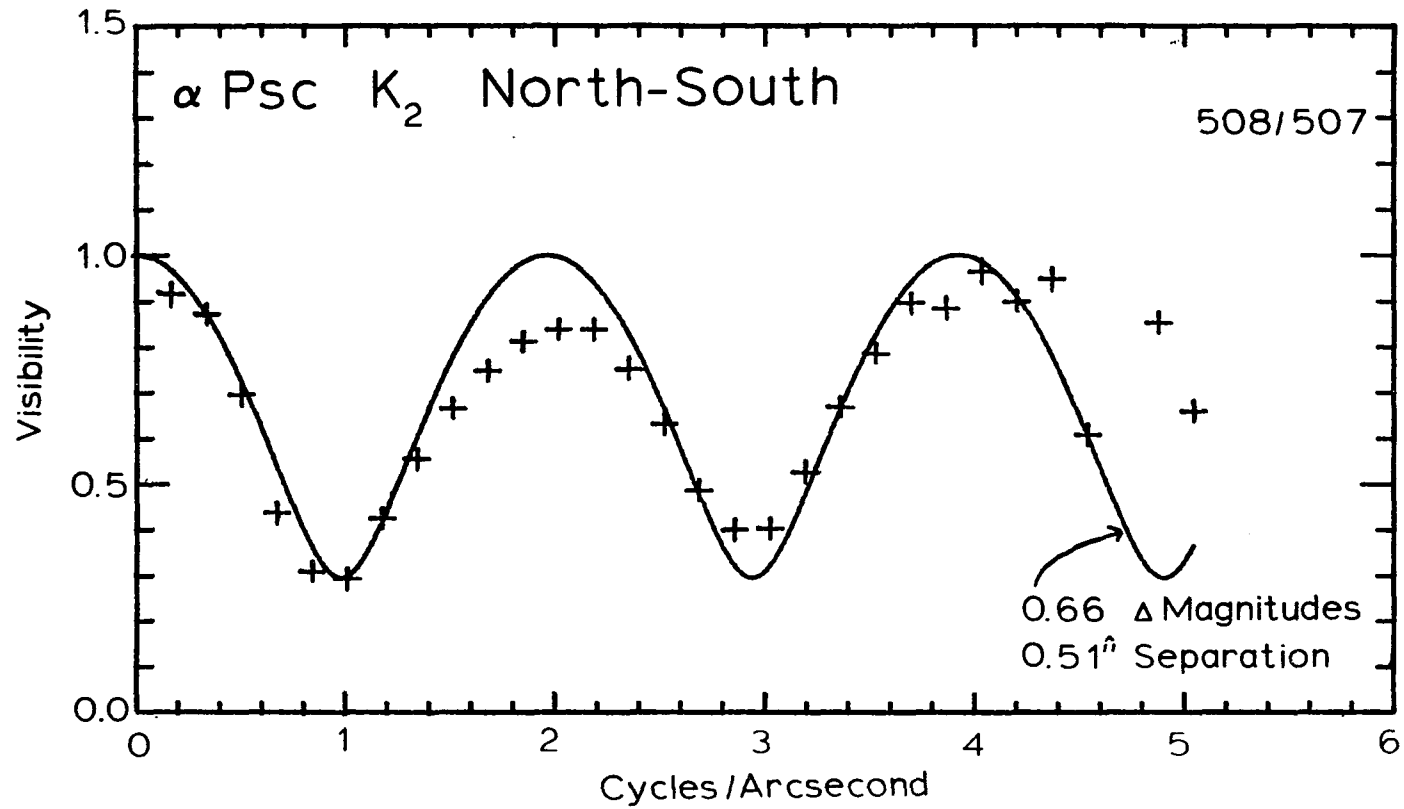


Fig. 21. Alpha Psc visibility. -- The north-south visibility which is the small component of the separation was measured at 2.2μ . The solid curve is a least-squares fit with a separation of $0.51''$ and a difference in magnitudes of 0.66 .

north-south separation of $0.48''$. The difference between this and the least-squares fit value of $0.51''$ is due to the error in slit position angle.

Asteroids

Several of the larger asteroids have brightnesses near the limits of the He detector and their diameters have been determined by several independent techniques. The two primary methods are radiometry (Morrison and Lebofsky 1979) and polarimetry (Dollfus and Zellner 1979). These yield accuracies of 10%. A few asteroids have been measured by visible speckle interferometry and some have precise diameters determined from stellar occultations. Since the asteroids are expected to have subdued albedo features they are good test objects which approximate uniform disks except for possible limb darkening.

Vesta. We observed this object on several nights. The data from the best of those nights is shown in Fig. 22a. A uniform disk is an excellent fit to the data. Also shown is a least-squares fit for a Lambert sphere which results in a 14% larger diameter. As can be seen there is virtually no difference between these curves except at the high frequencies. This is the region where small albedo features could affect the curves so there is little hope of determining both limb-darkening and diameter from speckle interferometry alone.

On the date of the observations Vesta was 1.70 AU from the earth. The uniform disk diameter of $0.410'' \pm 0.020$ then corresponds to 506 ± 25 km while the Lambert sphere is 574 ± 15 km. The radiometric diameter is 530 km while the polarimetric is 578 km. The uncertainties

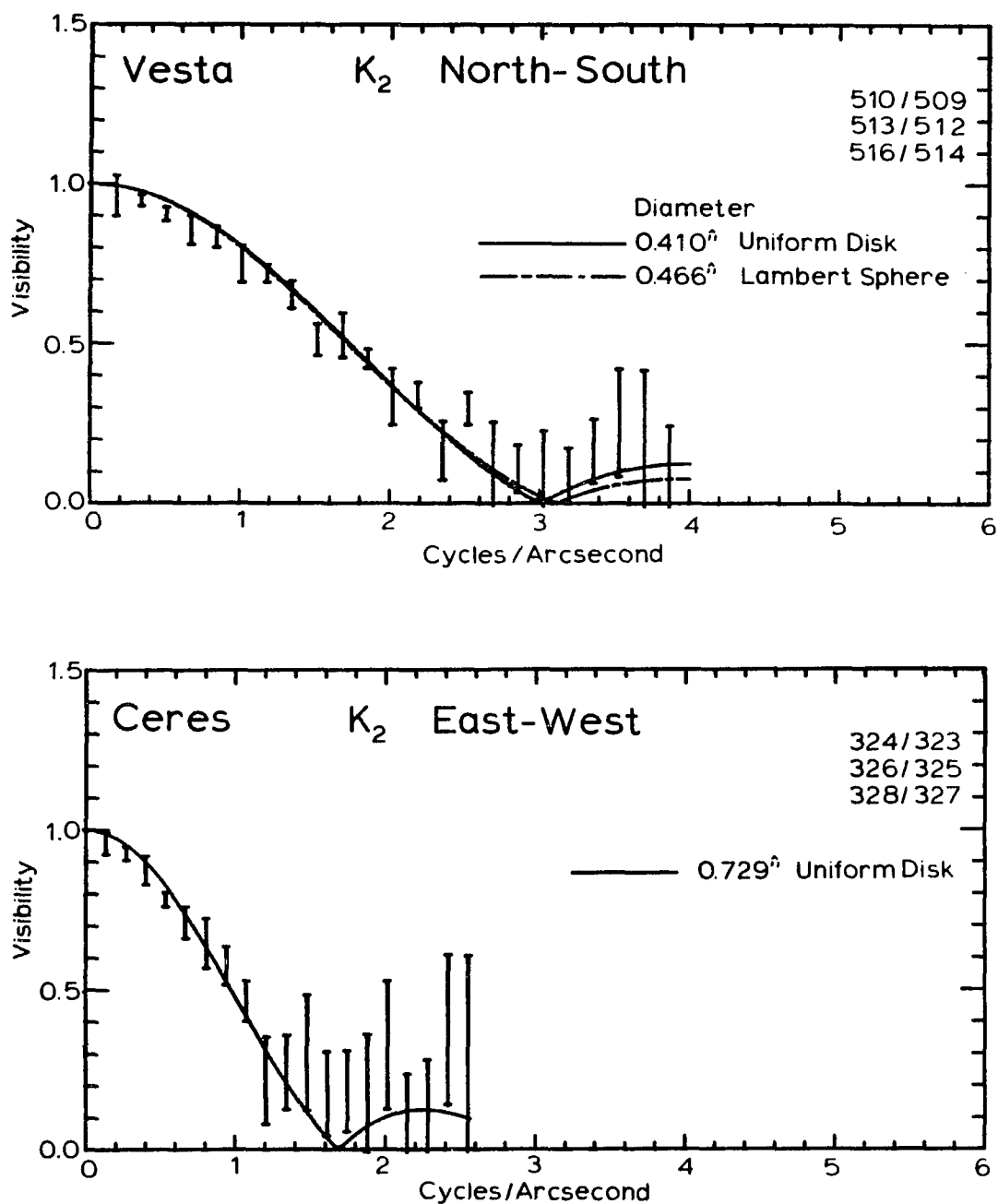


Fig. 22. Vesta and Ceres visibilities. — The data can be fit with either a uniform disk or Lambert sphere model. The diameters from these agree with those determined by radiometry and polarimetry to within the errors. For those data sets where the power in the sky scans was greater than in the object scans the result was set to zero. This causes a positive bias in the data beyond the first null.

in all these measurements prevent a derivation of the limb-darkening from the combined data however future observations of one of the asteroids for which an occultation diameter exist would allow such a determination.

Fig. 22b shows the visibility curve for Ceres. The uniform disk diameter is $0.729'' \pm 0.06$ which corresponds to 1081 ± 89 km. The radiometric diameter is 1014 km and the polarimetric is 1016 km. The results are equal to within the error-bars if the limb-darkening is small.

Galilean Satellites

The visibilities for Ganymede and Callisto are shown in Fig. 23. It can be seen immediately that there is a great difference between these objects and the asteroids. Here the visibilities drop off quickly due to the large size of the objects but level out at 0.3 or 0.4. If this behavior occurred closer to the limiting frequency of the telescope it might be attributable to the systematic errors mentioned earlier. However it occurs in a region where the MTF is still quite large. (The eventual rise in the Ganymede visibility beyond 2 cycles/arcsecond is probably due to such errors.)

Voyager images show much small-scale structure such as bright crater rims. These contribute a significant fraction of the total light since the surrounding material is of fairly low albedo. This unresolved structure causes the high visibility. Since these high albedo features are almost certainly water frost it would be interesting to observe in

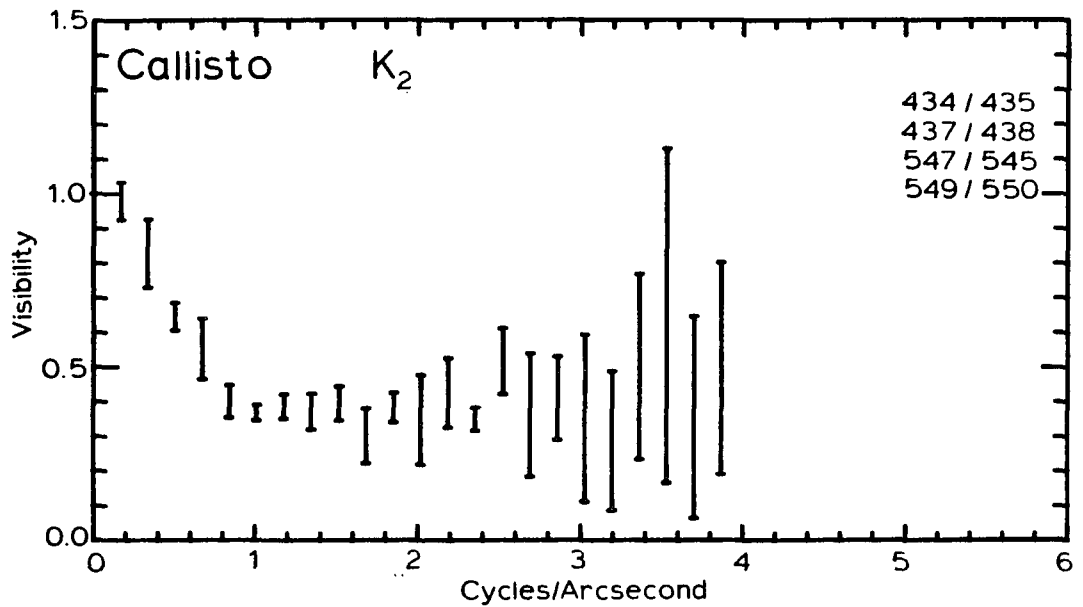
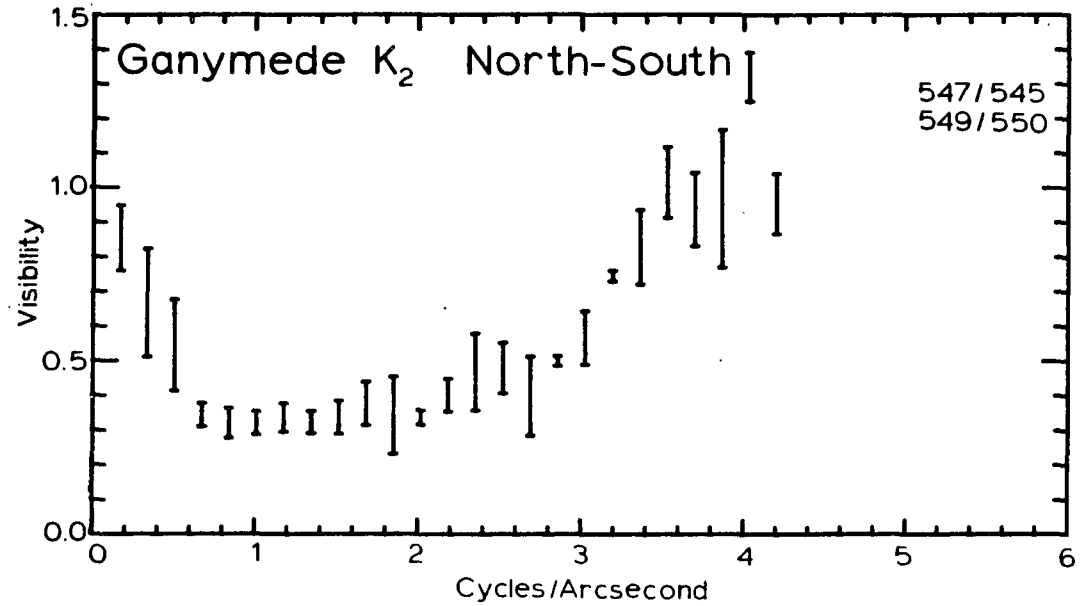


Fig. 23. Ganymede and Callisto visibilities. -- The visibilities do not fall to zero since there is unresolved structure in the images. The region beyond 2 cycles/arcsecond and the exact value of the flat section may be affected by the systematic errors discussed earlier.

the 2 micron absorption feature. At this wavelength the disk should appear more uniform.

These satellites are an example of speckle interferometry's ability to obtain information on objects which are not symmetrical. Even though an image is not reconstructed it is still possible to study the statistical properties of the small-scale structure.

CHAPTER 5

OBSERVATIONS

The objects observed can be divided into two categories; protostars, and evolved stars undergoing mass loss. For the first group the radiation arises from the dust which surrounds the object during collapse. High resolution measurements can determine the number of luminosity sources. When combined with detailed models they can measure the distribution of the dust, and perhaps the dynamics of the dissipation of this "cocoon". For the evolved stars the radiation arises from dust condensing during the mass loss. Here size measurements are useful in determining rates of mass loss and in some cases the past history of the loss rates.

Protostellar Objects

There are a large number of unresolved infrared sources similar to the Becklin-Neugebauer object which are believed to be protostars. They have a low temperature black-body like spectrum with 10 micron silicate and 3.1 micron ice absorptions (Merrill, Russell, and Soifer 1976). Their luminosities range from 10^3 to greater than $10^5 L_{\odot}$. However they lack the radio continuum emission expected from the HII regions which should surround main sequence stars of this luminosity.

There are two common explanations (Werner, Becklin, and Neugebauer 1977). The first is that the star has not yet reached the main sequence and has a temperature too low to produce Lyman-continuum

photons. The second is that although the star may be producing ionizing photons the HII region has not yet expanded enough to be detectable. Both require that the object be extremely young. Evidence that some objects are in the second stage is provided by emission of the Brackett α recombination line at 4.05 microns. This is a more sensitive indicator of compact HII regions than radio continuum emission (Simon, Simon, and Joyce 1979).

Brackett γ has also been detected in several of these objects (Thompson and Tokunaga 1978, 1979) and like $B\alpha$ this indicates an extremely compact HII region. For some of these objects the emission measure $N_e^2 V$ is greater than that of a zero age main sequence star (ZAMS) of the measured luminosity and they cite this as evidence for extra UV luminosity from accretion.

We have observed W3 IRS 5, S140, Mon R2 IRS 3, BN, GL 490, GL 2591, and NGC 2264. W3 was clearly resolved as a double and S140 was found to have a size of approximately 0.7". Mon R2 IRS 3 may have a similar size but the observations are noisy. BN was marginally resolved while upper limits were determined for the remaining objects.

W3 IRS 5

W3 is one of the most thoroughly studied regions of star formation (Wynn-Williams, Becklin, and Neugebauer 1972). It shows a range of objects from well developed HII regions to radio quiet IR sources with no $B\alpha$ emission. IRS 5 is one of the latter (Simon et al. 1979). In addition it is the site of H_2O maser activity. IRS 5 was first determined to have a double like character from slow slit scans at

10 microns (Wynn-Williams 1976). The present 5 micron speckle observations confirm it is a double and determine the precise orientation and relative brightness of the components.

The visibility curves for east-west as well as north-south scans are shown in Fig. 24. A least-squares fit gives an east-west separation of $0.757''$ and a north-south separation of $1.01''$ which corresponds to a total of $1.26'' \pm 0.06$. For the assumed distance of 3 kpc (Wynn-Williams et al. 1972) this corresponds to 3780 AU. The uncertainty of 5% results entirely from the calibration. Since the phase information is lost there would normally be an ambiguity about the orientation. However during moments of good seeing the components could be distinguished on individual scans. The fainter component was to the east and the north. Therefore the position angle is $37^\circ \pm 5$. The brightness ratio is 0.586 ± 0.029 for the east-west scans and 0.528 ± 0.014 for the north-south ones. The north-south curve was normalized by setting the first point to 1 because of problems with the photometry reduction. Therefore the brightness ratio from the east-west scans is more reliable.

Elsässer and Staude (1978) have proposed a bipolar nebula model to explain the high polarization of these objects. At first the speckle results might appear to support such a model but a detailed examination of the visibility shows this is not the case. In a bipolar nebula one would expect the size of the two lobes to be comparable to the separation between them. However if that were true then the individual sources would be partially resolved at the higher spatial frequencies and the second maximum of the visibility curve would be depressed.

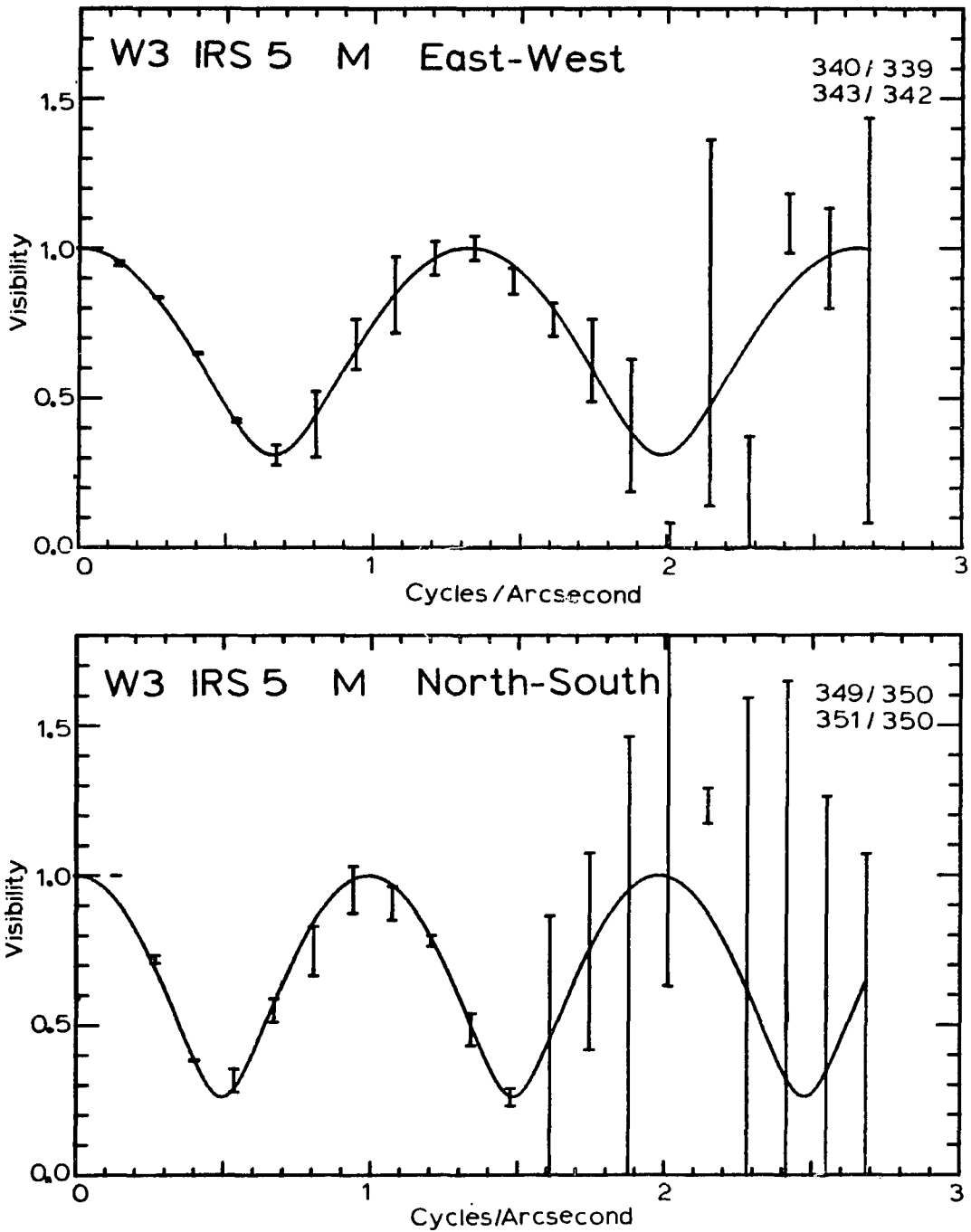


Fig. 24. W3 IRS 5 visibilities. -- The curves are least-squares fits for a double star. The east-west data give a separation of $0.757''$ and a brightness ratio of 0.586 while the north-south data give $1.01''$ and 0.528 . Because of problems with the photometry reduction, the north-south data were normalized by setting the first point to 1. This results in a slight positive bias.

Fig. 25 shows the east-west data along with several visibility curves generated by assuming the two components are uniform disks of equal size. One is forced to conclude that the diameter of the brighter source is less than $0.25''$. The visibility is less sensitive to the size of the fainter source so this could be slightly larger. Further evidence against the bipolar model comes from the polarimetry of Dyck and Lonsdale (1979) shown in Fig. 26b. The 3.8 micron polarization angle of 84° bears no clear relation to the position angle of the double. If the polarization results from scattering, it must occur within the individual components.

Fig. 26c from Genzel et al. (1978) is a VLBI map of the H_2O masers. It is impossible to make a detailed comparison because the absolute positions of the infrared sources relative to this map are not known. The separation between the two main centers of activity is roughly comparable to the separation of the infrared sources but the position angle for the radio is 20° rather than 37° . Also the southern center of activity has no counterpart in the infrared.

Measurements of the relative brightness over a range of wavelengths are needed in order to understand this complex object. Most previous observations have measured the combined flux and there is no guarantee that their spectra are similar. For example the measurements at 10 microns (Wynn-Williams 1976) indicate the sources have different amounts of silicate absorption. If one does assume that the spectra of the two components are the same then the color temperature of 350° and combined 4.8 micron flux of 59 Jy (Wynn-Williams et al. 1972) determine

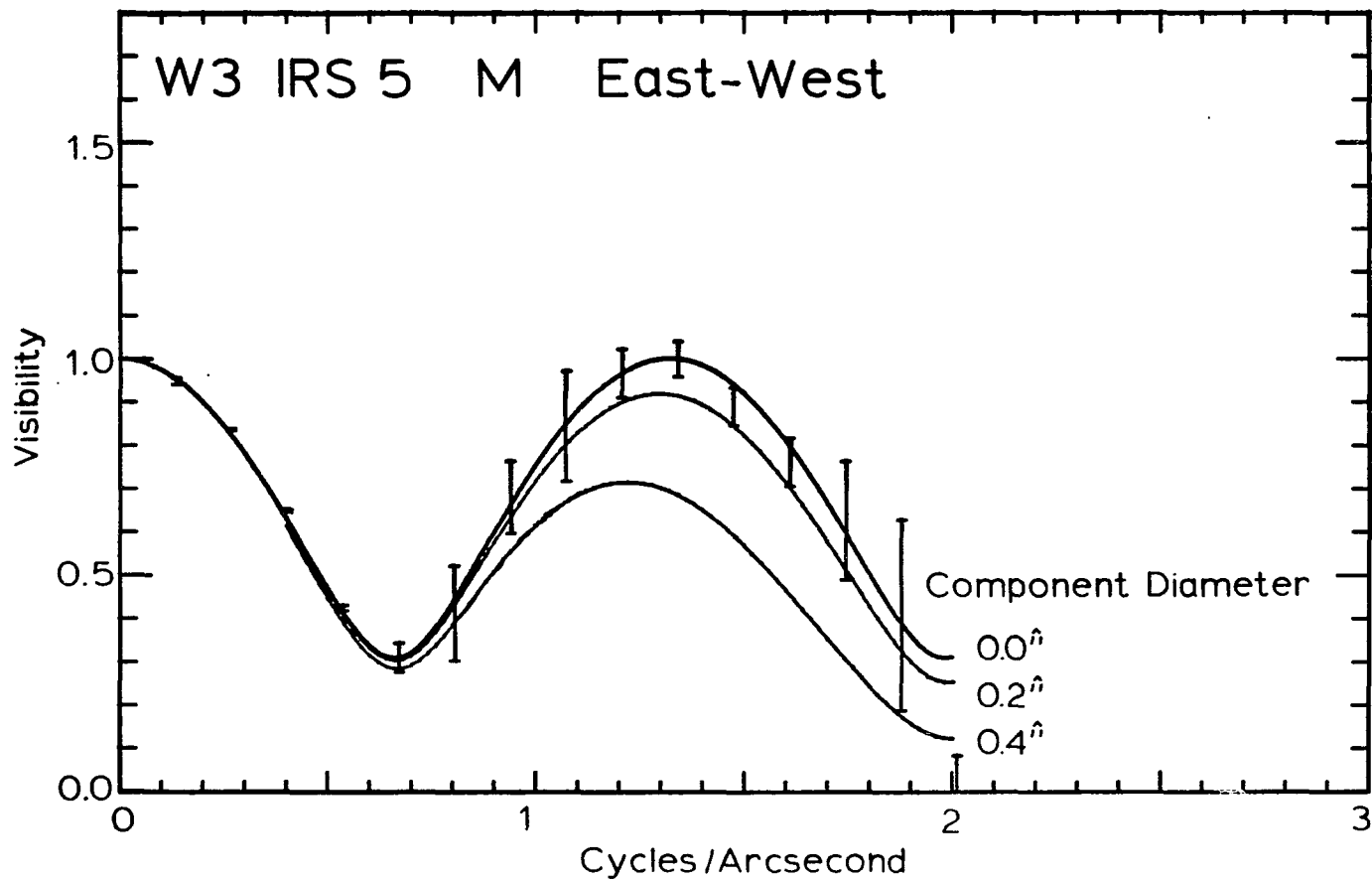


Fig. 25. Size limits for IRS 5 components. -- The solid lines are theoretical curves for double stars where the individual components are uniform disks of the indicated size.

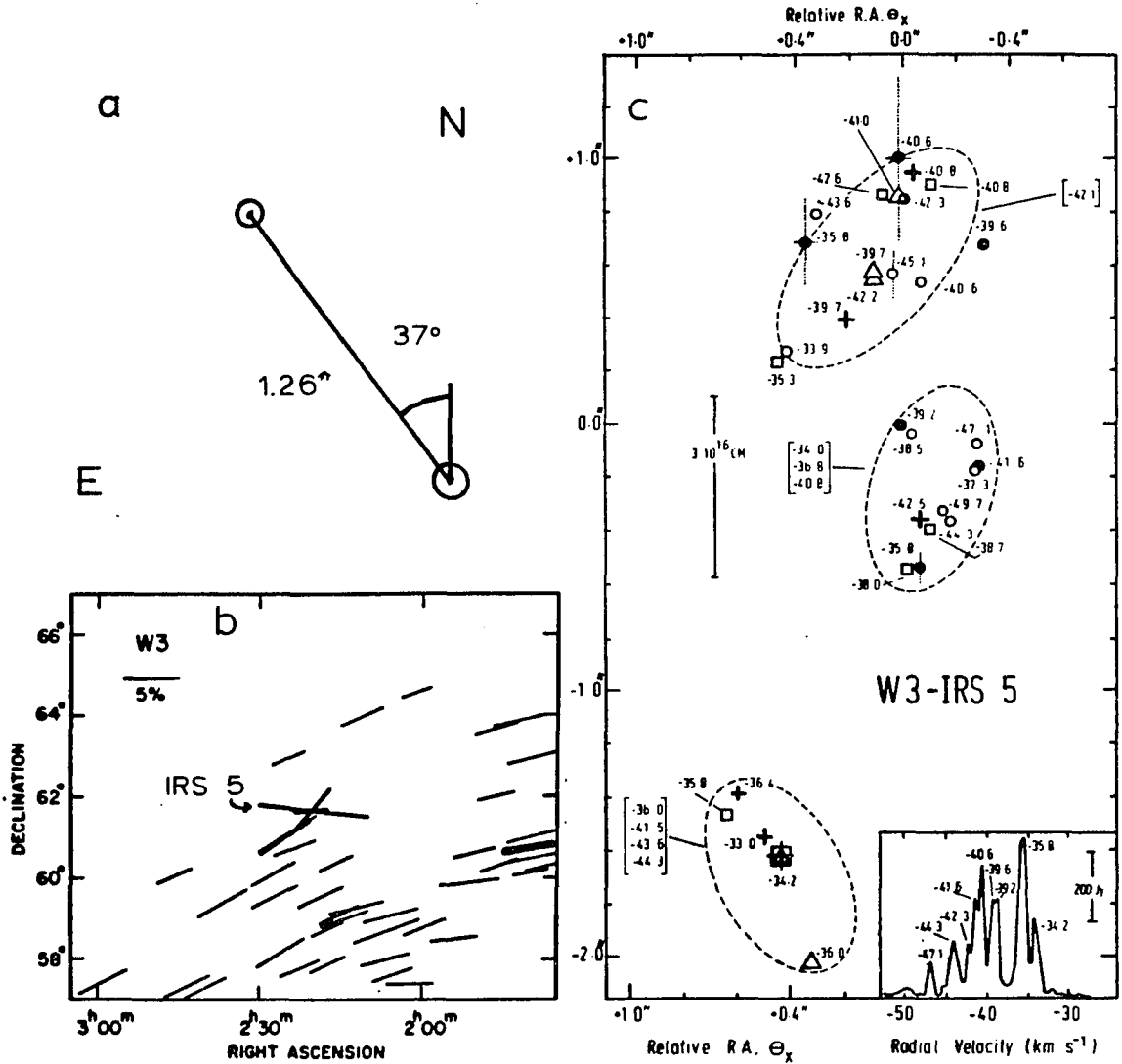


Fig. 26. W3 IRS 5 orientation, polarimetry, and H_2O masers. — The orientation is that determined from the speckle observations. The observations of Dyck and Lonsdale give the polarization of three objects in W3 as well as the orientation of the galactic magnetic field. The H_2O maser map contains data from a variety of sources as plotted in Genzel et al.

a black-body diameter of 0.17" for the brighter component. Since the upper limit is 0.25" it appears to be optically thick.

Determining the size of the individual components as a function of wavelength should be an important goal of future observations. Some objects such as GL 2591 increase in size between 2 and 10 microns. The measurement of the size of the components across the silicate absorption would be useful for determining the dust distribution (Kwan and Scoville 1976). In some studies the size of the overall double has been used in comparisons with other objects. However since the two sources are discrete the individual sizes of < 750 AU would be more appropriate.

S140

Sharpless 140 is a molecular cloud that has been studied because of its supposed simplicity. It does not contain the multitude of HII regions and other sources present in the W3 complex and therefore is simpler to interpret. However on a smaller scale Blair et al. (1978) have found several sources at 2 microns although a single one, S140 IR, is by far the brightest and dominates the long wavelength emission. Its spectrum is similar to BN. No radio continuum is observed and Simon et al. (1979) as well as Dinerstein, Lester, and Rank (1979) place upper limits on the B_{α} emission.

Dinerstein et al. have also obtained a 0.9 micron CCD image. Four discrete nebulous objects are observed which are approximately 5" in size and distributed in a region 20" across. Beichman (reported in Tokunaga et al. 1978) finds three 10, 20, and 25 micron sources in this same region although the positions are not given. The brightness of one

source is 10 times that of the others and it has a half-power diameter of $< 10''$.

Fig. 27 shows the observed visibility at K. The object is clearly resolved. There is some evidence for a two component structure with approximately half of the radiation coming from a $1.5''$ region and the rest unresolved. However this data is affected by the errors that add energy at high spatial frequencies so it should not be over-interpreted. A uniform disk fit to the data would give a diameter of approximately $0.8''$. The distance is estimated to be 910 pc (Crampton and Fisher 1974) so the size is on the order of 900 AU. The object was measured with the Michelson interferometer in November 1979. The M visibility was 0.55 ± 0.1 at 3.1 cycles/arcsecond. Without further measurements it is impossible to tell whether this also indicates half the flux from an extended region. A uniform disk fit to this single point would be $0.17''$ which is considerably smaller than the above size.

Mon R2 IRS 3

Mon R2 is a compact HII region with several infrared sources (Beckwith et al. 1976). The brightest of these is IRS 3 which appears to be offset from the radio continuum source. It has been studied in the far infrared by Thronson et al. (1980). IRS 3 has a spectrum similar to the above objects and again no B_{α} has been detected (Simon et al. 1976). Beckwith et al. have resolved the source at 8.7, 9.5, 11.2, 12.5 and 20 microns using slow declination slit scans. The full width for a Gaussian source is $0.4''$ outside the silicate band but is $0.2''$ at 9.5 and 11.2 microns. They state that this could reflect either size

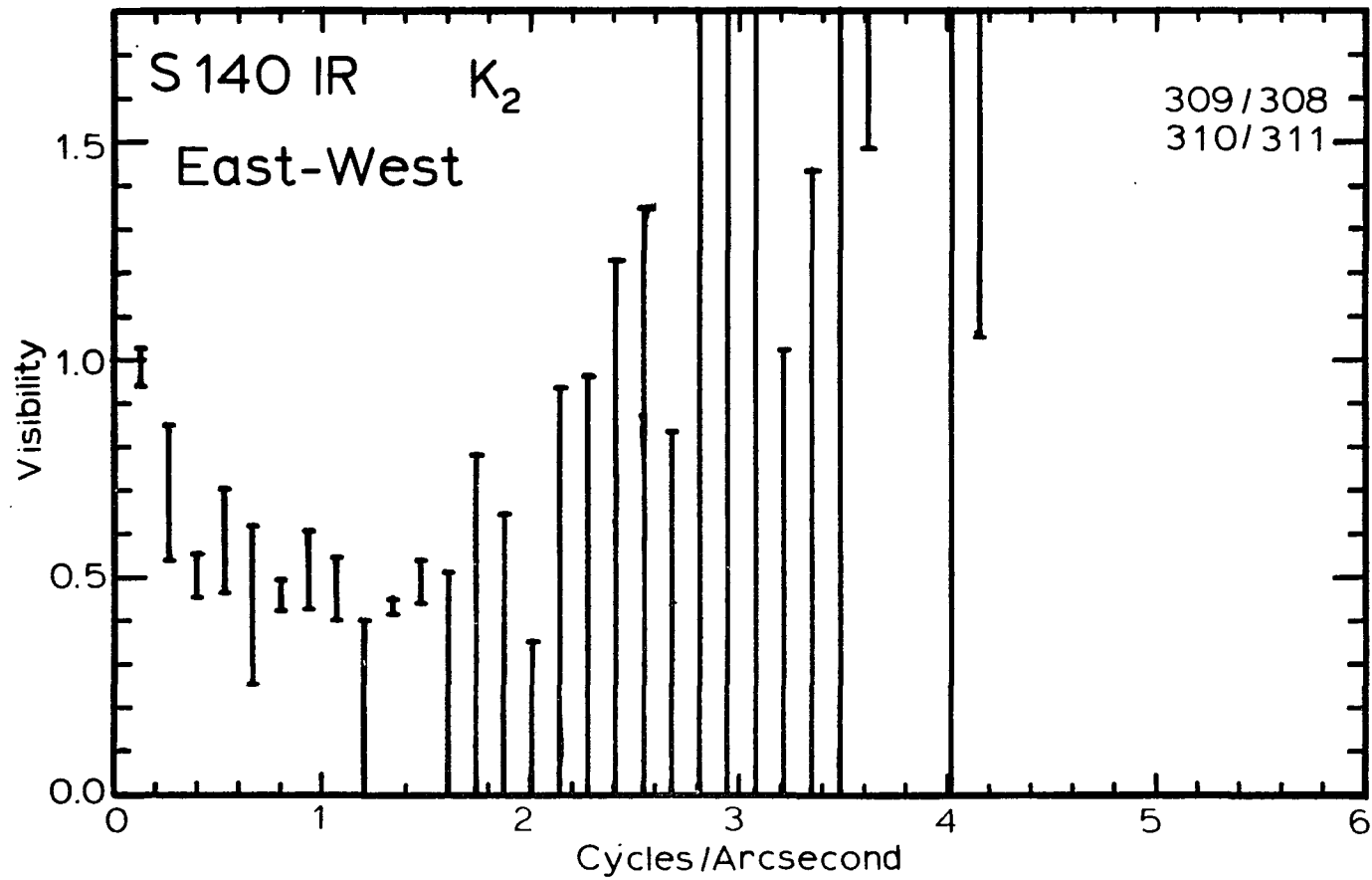


Fig. 27. S140 IR visibility. -- There is some indication of an extended component contributing half the flux.

variations of a single source or different silicate absorptions for the components of a double source.

It is important to decide between these two models. If it is double then this helps explain the low Lyman-continuum relative to total luminosity. If it is a single source the change in size through the silicate feature is the opposite of that expected from the model of Kwan and Scoville (1976). The conventional interpretation is that the absorption arises from intervening grains while the underlying source is either a black-body or has 10 micron emission. Kwan and Scoville propose that for these objects the silicate feature is produced by the lower temperature in the outer parts of a continuous distribution of dust. Their model predicts larger sizes in the silicate feature while the conventional model predicts a more constant size. Future speckle observations at 10 microns should resolve this.

The present observations were made at shorter wavelengths. Fig. 28 shows the visibility for 2 micron east-west scans. This source is near the present sensitivity limits of the speckle system so the results are very noisy. Two independent sets of measurements are shown and they both indicate the source is resolved. Little more can be said from this data except that a size on the order of 1" is indicated. Since the distance is believed to be 950 pc this size is similar to that of S140.

BN

BN is the prototype of these objects. The one significant difference from the three above is that it has B_{α} emission. At 500 pc

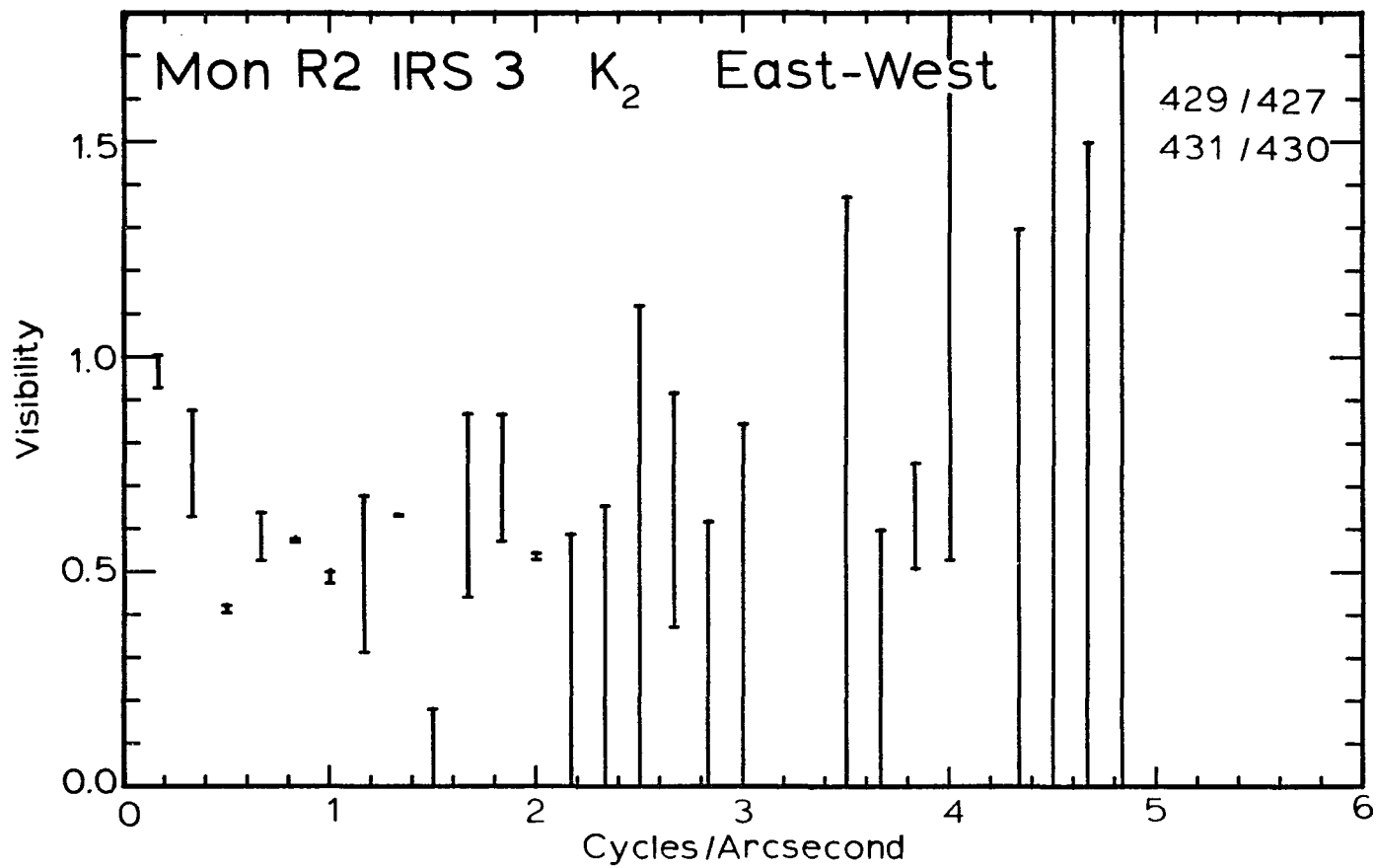


Fig. 28. Mon R2 IRS 3 visibility. -- The size is on the order of 1" but the data are too noisy to permit an accurate fit.

it is also the closest and therefore the best studied. Data from two nights are presented in Fig. 29. The object appears to be slightly resolved with a diameter between 0.10" and 0.15". However small effects such as this can be produced by seeing changes. Although the results seem to repeat it is safer to regard the 0.15" as an upper limit. The data from the second night indicates that 10% of the flux comes from a larger region but again this must be regarded with suspicion until higher quality observations are obtained. Foy et al. (1979) have determined upper limits of 0.1" at 4.8 microns and 0.08" at 3.5 microns for this source. At 500 pc 0.1" corresponds to 50 AU so this source is significantly smaller than those discussed above.

GL 490

This is the only object we have observed besides BN which shows B_{α} emission (Simon et al. 1979). Thompson and Tokunaga (1979) have also detected B_{γ} . The latter observations indicate that the source has a UV luminosity greater than a ZAMS star and this is one of the objects for which Thompson and Tokunaga suggest UV radiation caused by accretion. Harvey et al. (1979) have measured the far infrared emission and recently Lada and Harvey (1980) have detected a bipolar outflow of gas using CO mapping.

The visibility was measured at 2 microns scanning east-west (Fig. 30). The diameter is less than 0.2" and for a distance of 900 pc this corresponds to 180 AU, again significantly less than that of the first three objects discussed.

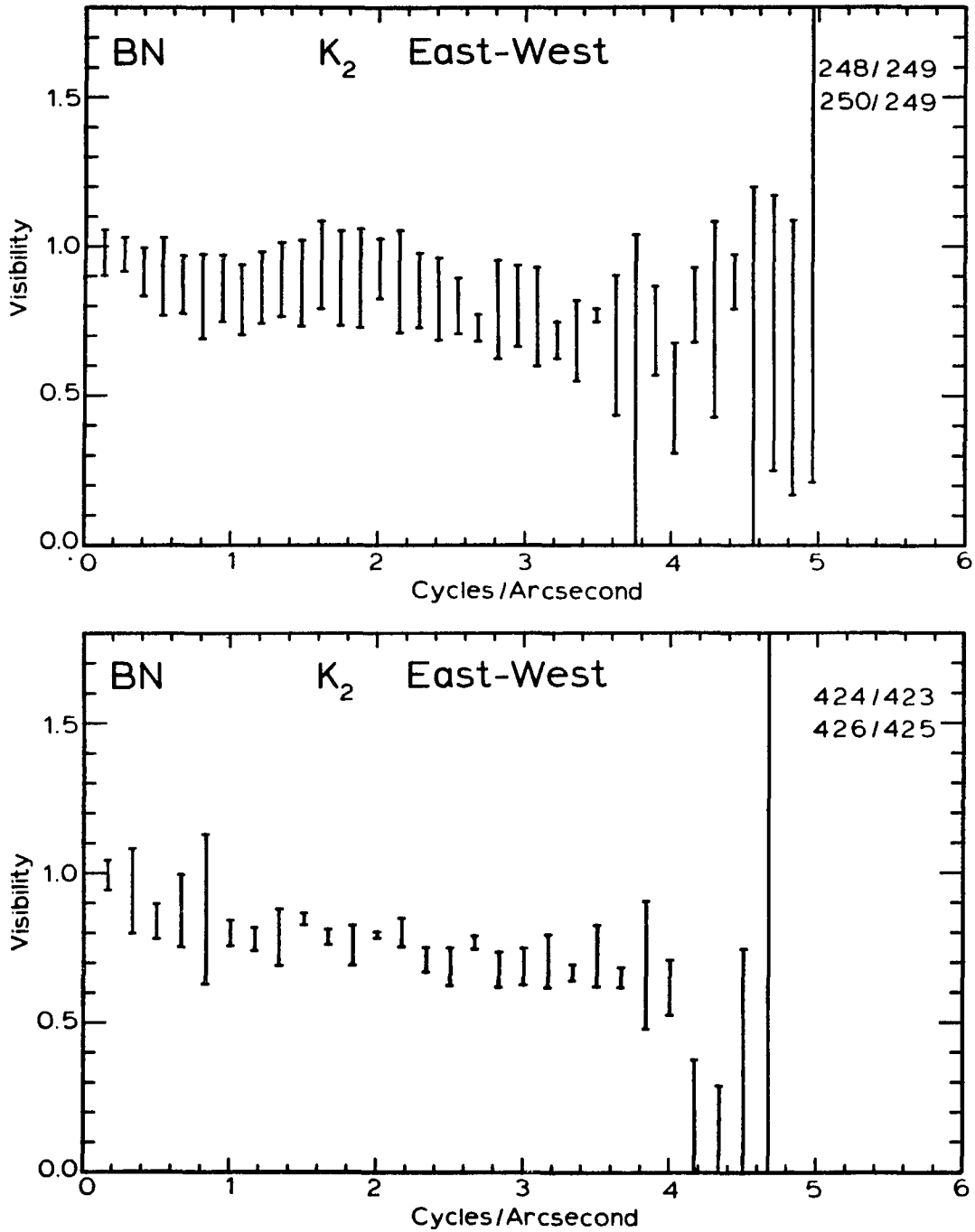


Fig. 29. BN visibilities. -- Two independent sets of data are shown. There is some indication that the object is resolved but for the present an upper limit of $0.15''$ is adopted.

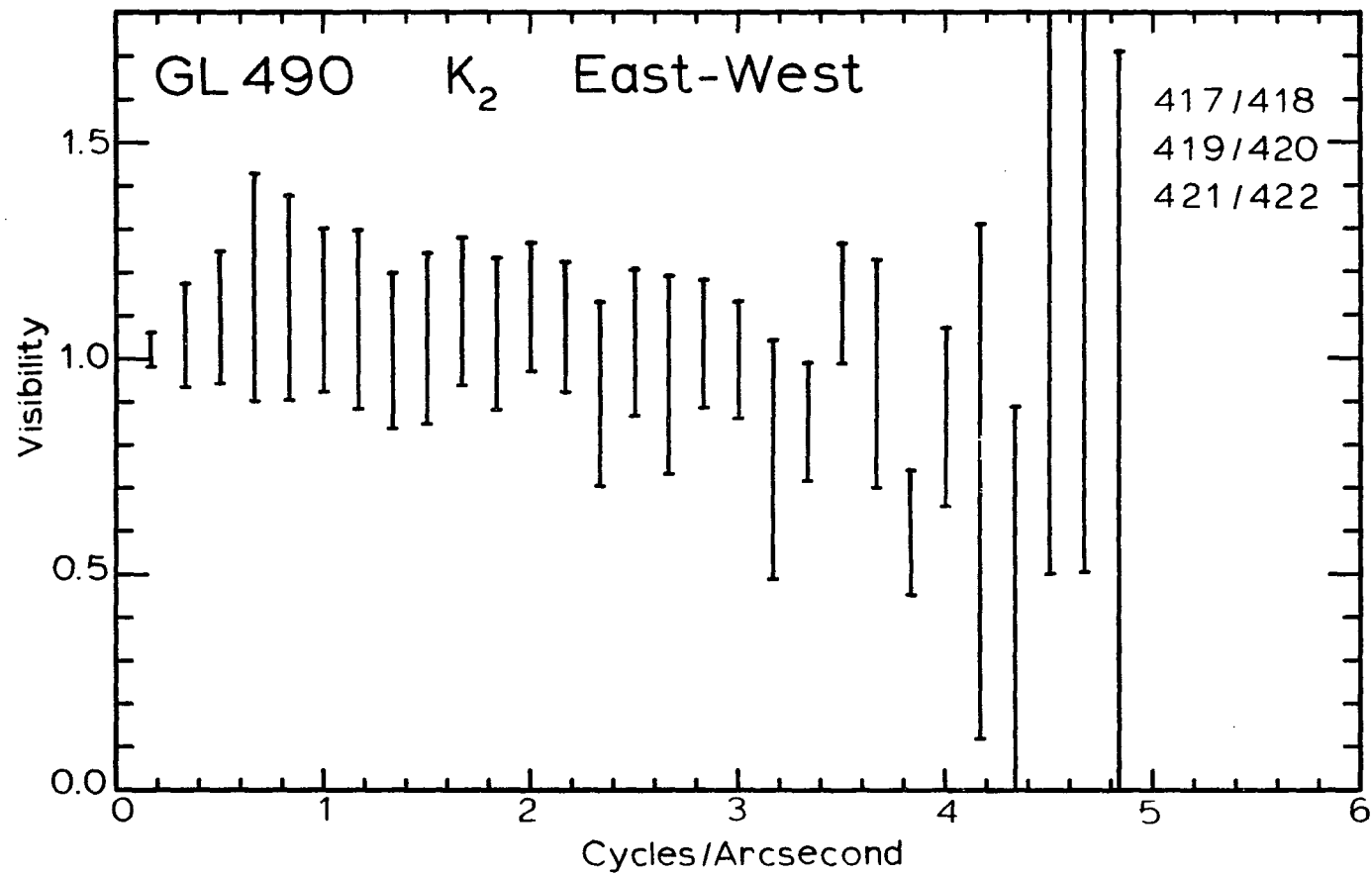


Fig. 30. GL 490 visibility. — The diameter is less than 0.2".

GL 2591

This source was originally believed to be associated with a compact HII region observed in the radio. However careful position measurements by Wynn-Williams et al. (1977) proved that they were separated by 7". Spectrophotometry has been obtained by Merrill and Soifer (1974). An upper limit to the B_{γ} flux is given by Thompson and Tokunaga (1979) who suggest that a dust cloud surrounds the star and prevents an HII region from enveloping it. They further suggest that the nearby HII region mentioned above may result from a hole in this dust cloud which allows ionizing photons to escape in that direction.

A single observation of the visibility for north-south scans with the K filter is shown in Fig. 31. The seeing was not very stable during these observations therefore a conservative upper limit of 0.2" is placed on the diameter. This is consistent with the 0.07" limit which Foy et al. (1979) have derived for 3.5 microns. These measurements are less than the $0.5'' \pm 0.3$ size at 12.5 microns derived by Wynn-Williams et al. from slow slit scanning. More observations are needed at intermediate wavelengths and at different position angles.

The distance to this source is relatively uncertain (Merrill and Soifer 1974) and might range from 1 to 3 kpc. Adopting a value of 1.5 kpc leads to an upper limit of 300 AU.

NGC 2264 IRS

This infrared source is associated with an optical nebula (Allen 1972). The luminosity of $3.5 \times 10^3 L_{\odot}$ has been determined by the far infrared measurements of Harvey, Campbell, and Hoffmann (1977). B_{γ} has

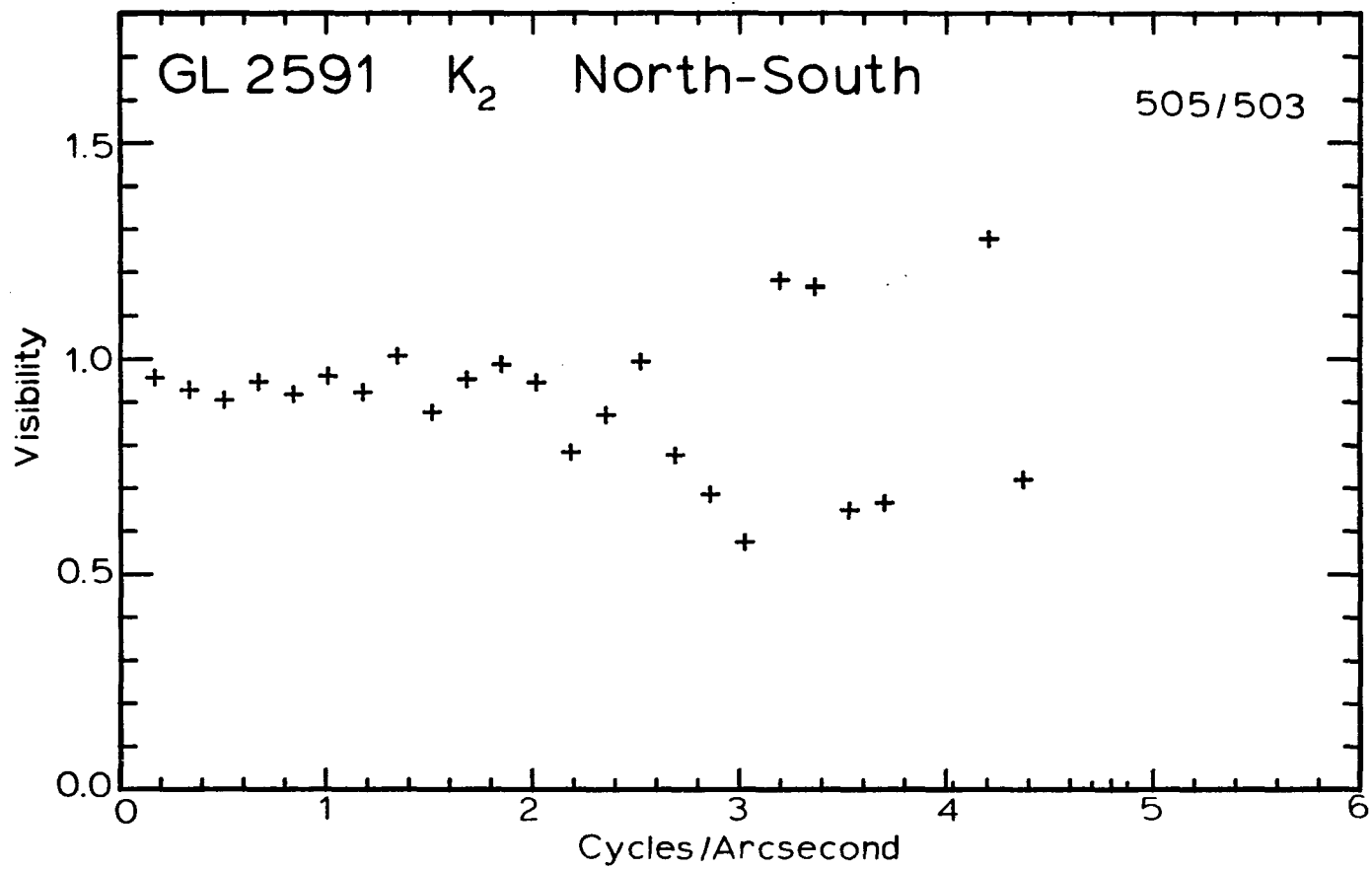


Fig. 31. GL 2591 visibility. --- The diameter is less than 0.2".

been detected by Thompson and Tokunaga (1978) in excess of what would be expected for a ZAMS star of this magnitude. They interpret this as evidence for excess luminosity from an accretion shock.

We have measured this object with both the K and M filters in a north-south direction. The visibility curves are shown in Fig. 32. Since only single measurements were obtained a conservative upper limit of 0.25" for both wavelengths is adopted. For an assumed distance of 800 pc this is 200 AU. The M-L color temperature is 700^o and the K and M magnitudes indicate a black-body diameter of less than 0.05" so it is not surprising that the object is unresolved.

Summary

Both S140 and Mon R2 IRS 3 have sizes on the order of 800 AU and the diameter of the brighter component of W3 IRS 5 (although at a different wavelength) is comparable. This is considerably larger than the upper limits set for BN (<50 AU), GL 490 (<180 AU), GL 2591 (<300 AU) and NGC 2264 IRS (<200 AU). It is difficult to understand the distinction between these objects since their spectra are similar. Although three of the objects in the latter group show recombination line emission this is not true of GL 2591.

The brighter component of W3 IRS 5 has an upper limit less than twice the black-body size. The only other object observed at 5 microns has a black-body size too small to be measured. These comparisons cannot be made for the 2 micron observations. On the exponential side the black-body curve is extremely sensitive to temperature. Given the uncertainties in estimating the color temperature the black-body sizes

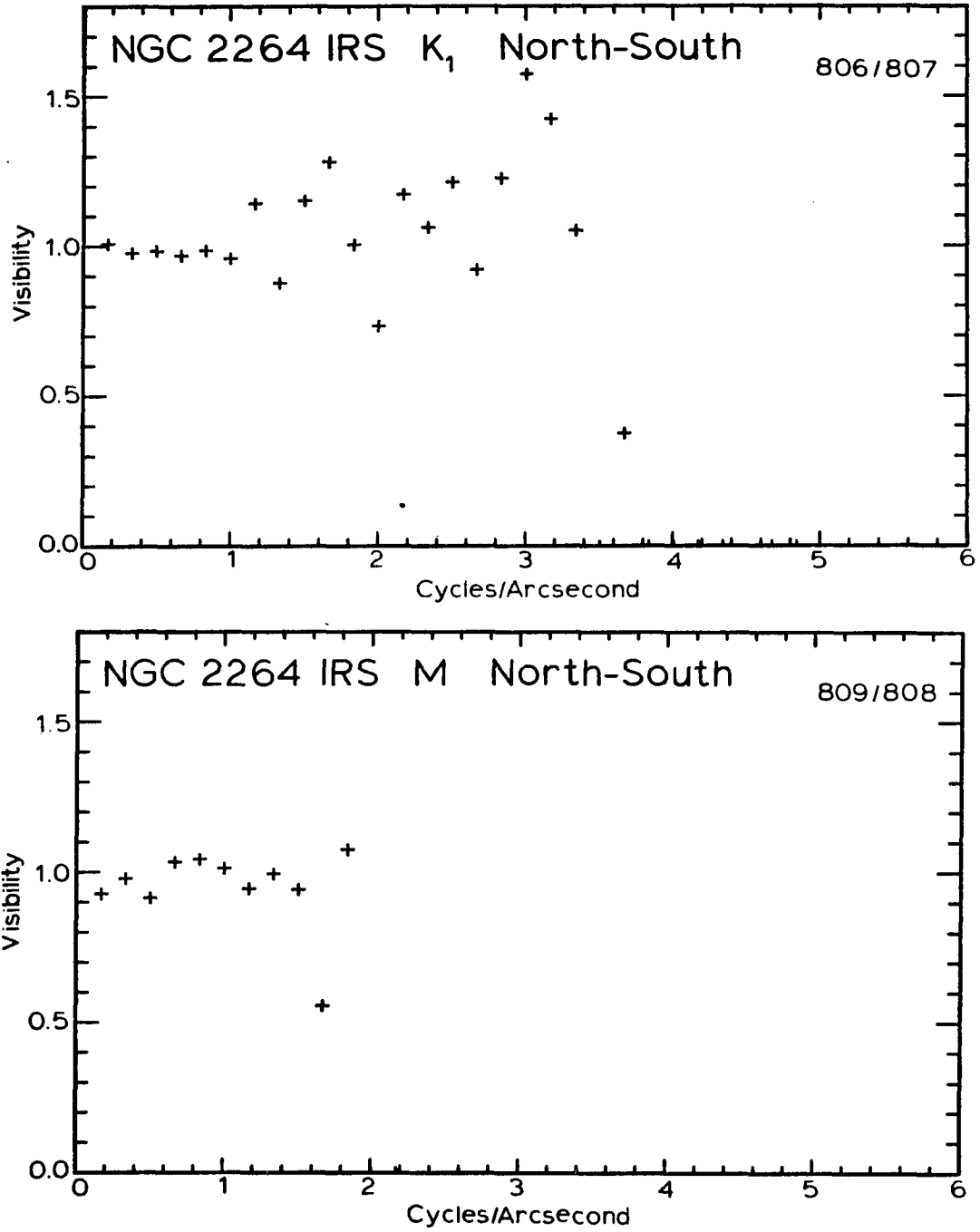


Fig. 32. NGC 2264 IRS visibilities. -- The diameter is less than 0.25" at both wavelengths.

are not sufficiently accurate. More detailed modeling is necessary but unfortunately most published ones do not predict short wavelength diameters.

The principle need in the future is for greater wavelength coverage. Our observations concentrated on 2 rather than 5 microns because of the higher resolution and also the greater sensitivity of that detector. However the above results indicate that there are advantages to the longer wavelengths. The size of the objects may increase towards longer wavelength (e.g., GL 2591) and they are certainly brighter. The interpretation may also be simpler. A very important area will be determining sizes throughout the silicate band, and perhaps the same can be done for the 3.1 micron ice feature.

Evolved Stars

The study of stars undergoing mass loss has been one of the principle activities of the Michelson interferometry program. It has resolved shells around IRC+10216, Alpha Ori, VY CMa, and Omicron Ceti, as well as several other objects. An important goal of the speckle program has been to extend the wavelength and spatial frequency coverage of these objects. Several papers on the Michelson observations have been published and the reader will be referred to them for a general discussion of the implications of the measured visibilities. The following is a discussion of the additional information obtained by the speckle system for IRC+10216 and Alpha Ori. For the remaining objects the visibility curves are merely presented with short comments on the results.

The speckle interferometer has obtained good wavelength and position angle coverage of IRC+10216 and further determined the wavelength dependence of the asymmetry detected by McCarthy et al. (1980). The speckle observations also have determined the diameter of the silicate shell surrounding Alpha Ori which was resolved by McCarthy et al. (1977b). New measurements of the visibility of VY CMa were obtained and upper limits were placed on the sizes of several other stars.

IRC+10216

IRC+10216 is a late-type variable carbon star with a period of 600 days. Visible photographs show an $\sim 1'' \times 2''$ image where the direction of elongation is $\sim 30^\circ$ (Becklin et al. 1969, and McCarthy and White 1980). The 1 micron polarization is 20% and is perpendicular to the elongation (Shaw and Zellner 1970) while the polarization is considerably less at longer wavelengths (Capps and Knacke 1976). The object was first resolved in the infrared by a lunar occultation (Toombs et al. 1972). Those observations indicated that at the shorter wavelengths 85% of the light came from a $0.4''$ disk and the rest from a $2''$ shell while at 10 microns each component contributed half. McCarthy and Low (1975), McCarthy et al. (1977), Sutton et al. (1979), Selby et al. (1979), and McCarthy et al. (1980) have measured it at a variety of wavelengths. The last work summarizes the state of the spatial observations up to this time.

Rather than the discrete two component model proposed by Toombs et al. the interferometry showed a smooth brightness distribution that

could be roughly approximated as gaussian. The object was found to be elongated at 2 and 5 microns. At 5 microns the north-south and east-west visibilities were approximately the same at 1 cycle/arcsecond but diverged beyond this. There were no observations at both position angles for smaller spatial frequencies. The Michelson results also showed the 5 micron visibility varied with phase although it was only monitored consistently at 1.8 cycles/arcsecond. From limited position angle coverage Sutton had proposed a spherically symmetric model for 11 microns.

Figs. 33 and 34 show the recent speckle observations. Also plotted are the Michelson results and 2 micron results of Selby et al. The latter observations lie significantly above our speckle data. This may be evidence for visibility changes at 2 as well as at 5 microns. The speckle observations show that at 2 microns the asymmetry exists at all spatial frequencies while at 8 microns the asymmetry is not apparent out to 1 cycle/arcsecond. They suggest that the outer part of the envelope radiating most of the 8 micron flux is fairly symmetrical but cannot rule out asymmetry at the higher spatial frequencies corresponding to the hotter core of the object.

The 5 and 11 micron visibilities calculated by Crabtree and Martin (1979) with a spherically symmetric model are shown in Fig. 33. The model fits the north-south 11 micron data but predicts slightly too high a visibility at 5 microns. Axially symmetric models could presumably be developed to fit both position angles.

There are two possible ways to explain an asymmetry in the infrared shape. The simplest explanation would be that the mass

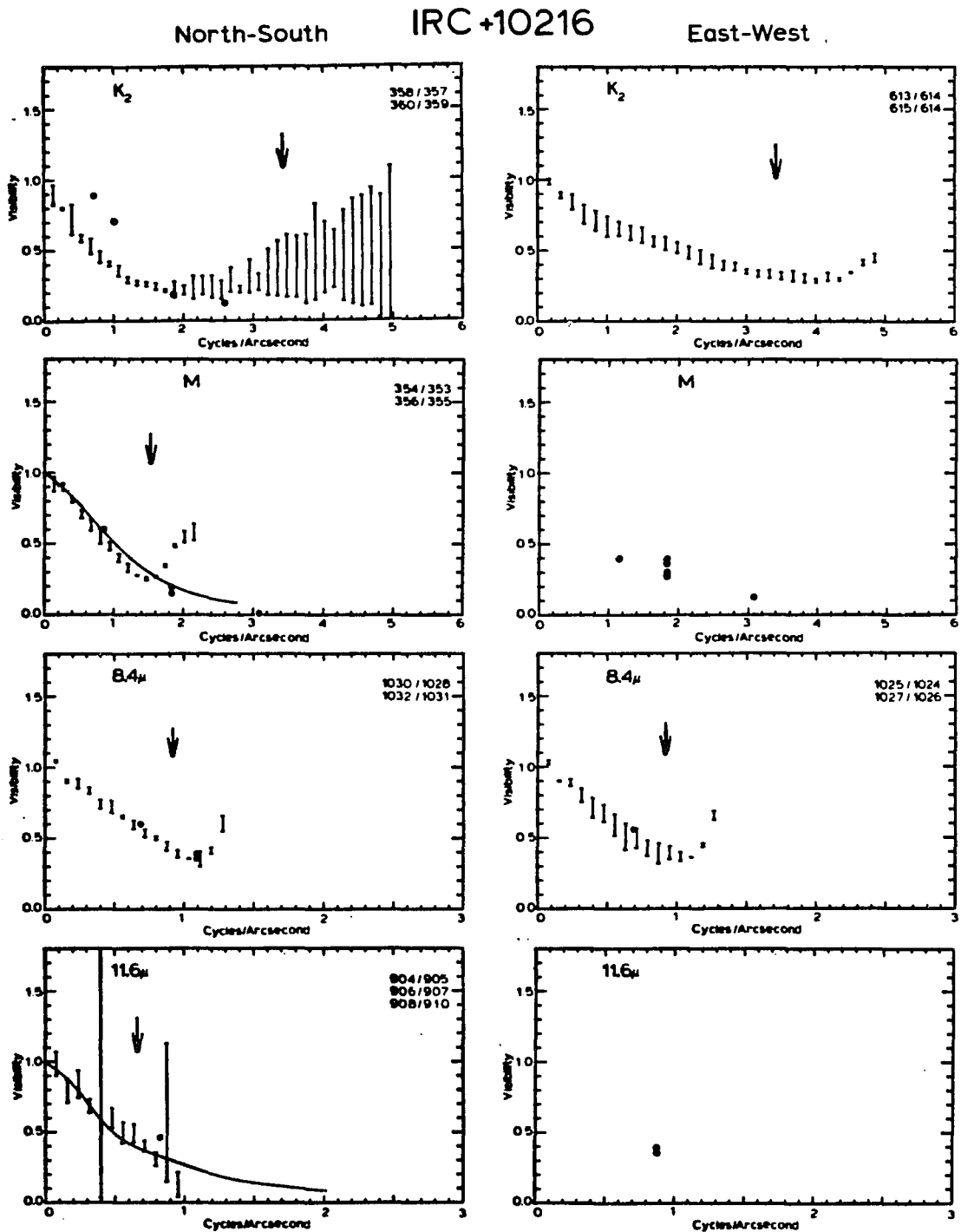


Fig. 33. IRC+10216 visibilities. — The solid curves are the models of Crabtree and Martin, the open circles are from Selby et al., and the solid circles are the Michelson observations. For the Michelson work the 11.3μ rather than the 11.6μ filter was used. Systematic errors affect the speckle observations beyond the $0.7 f_0$ point marked by the arrows.

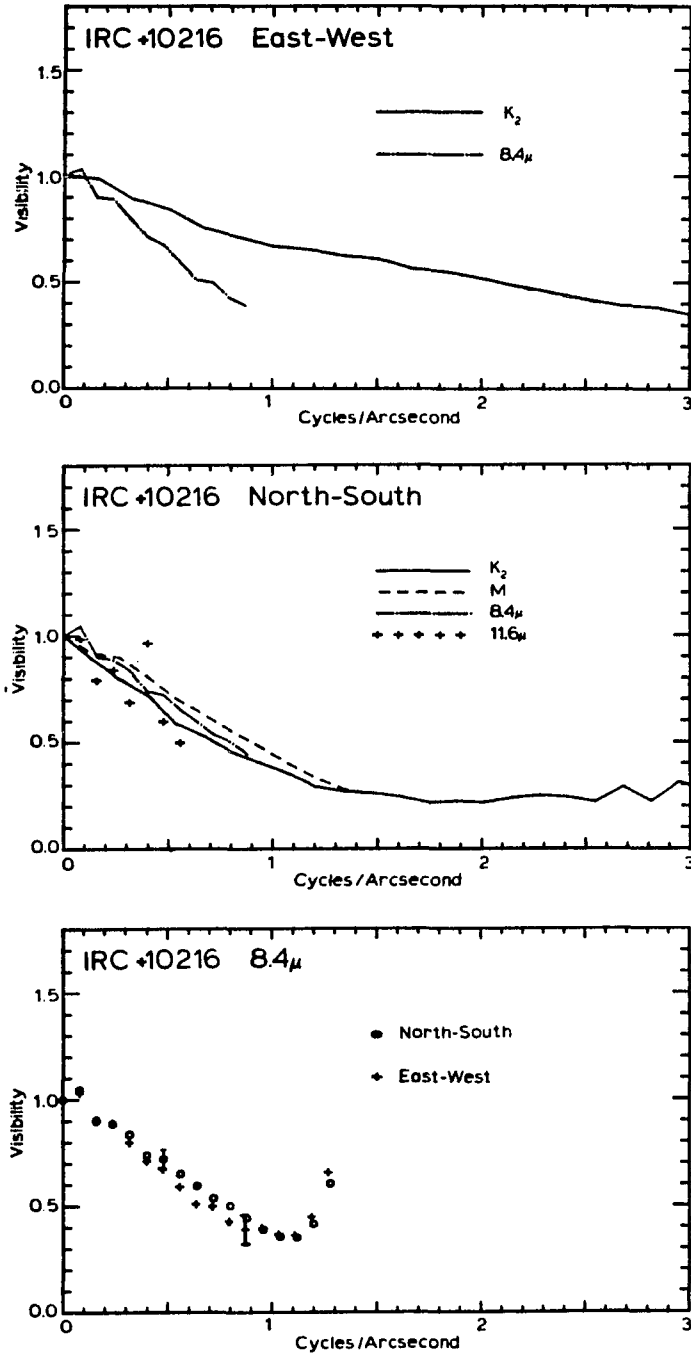


Fig. 34. Comparison of IRC+10216 visibilities. -- The data from Fig. 33 are replotted.

distribution is asymmetric at the emitting region. This is supported by the CO maps of Wannier et al. (1979) which indicate an elongation out to $> 30''$. However it is then hard to understand why the 8 micron shape is more symmetrical. An alternative explanation would be a symmetrical mass distribution at a distance but asymmetries close to the star (for example a disk) which blocked light and therefore lowered the temperature of parts of the envelope. Detailed models will be necessary to discriminate between these two possibilities.

Alpha Ori

This is an M2Iab star undergoing mass loss (Weymann 1962). The circumstellar shell which surrounds it has been previously resolved in the 10 micron emission feature. However all previous observations (McCarthy et al. 1977, Sutton 1979) have been at high enough spatial frequencies to completely resolve the shell. Therefore they provide only lower limits on its size. They do show that between 0.63 and 0.76 of the flux comes from an unresolved source. There is some debate about whether it is entirely from the star or part is from chromospheric emission or dust at small distances.

Fig. 35 shows the 11.6 micron speckle observations. They indicate that 0.37 of the flux comes from a shell approximately $4''$ in size. The visibility increases beyond 0.5 cycles/arcsecond because NML Tau, the "point source" used for this object, is partially resolved (Fig. 36). However the measurements of Sutton and McCarthy show that the visibility is in fact flat to greater than 5 cycles/arcsecond.

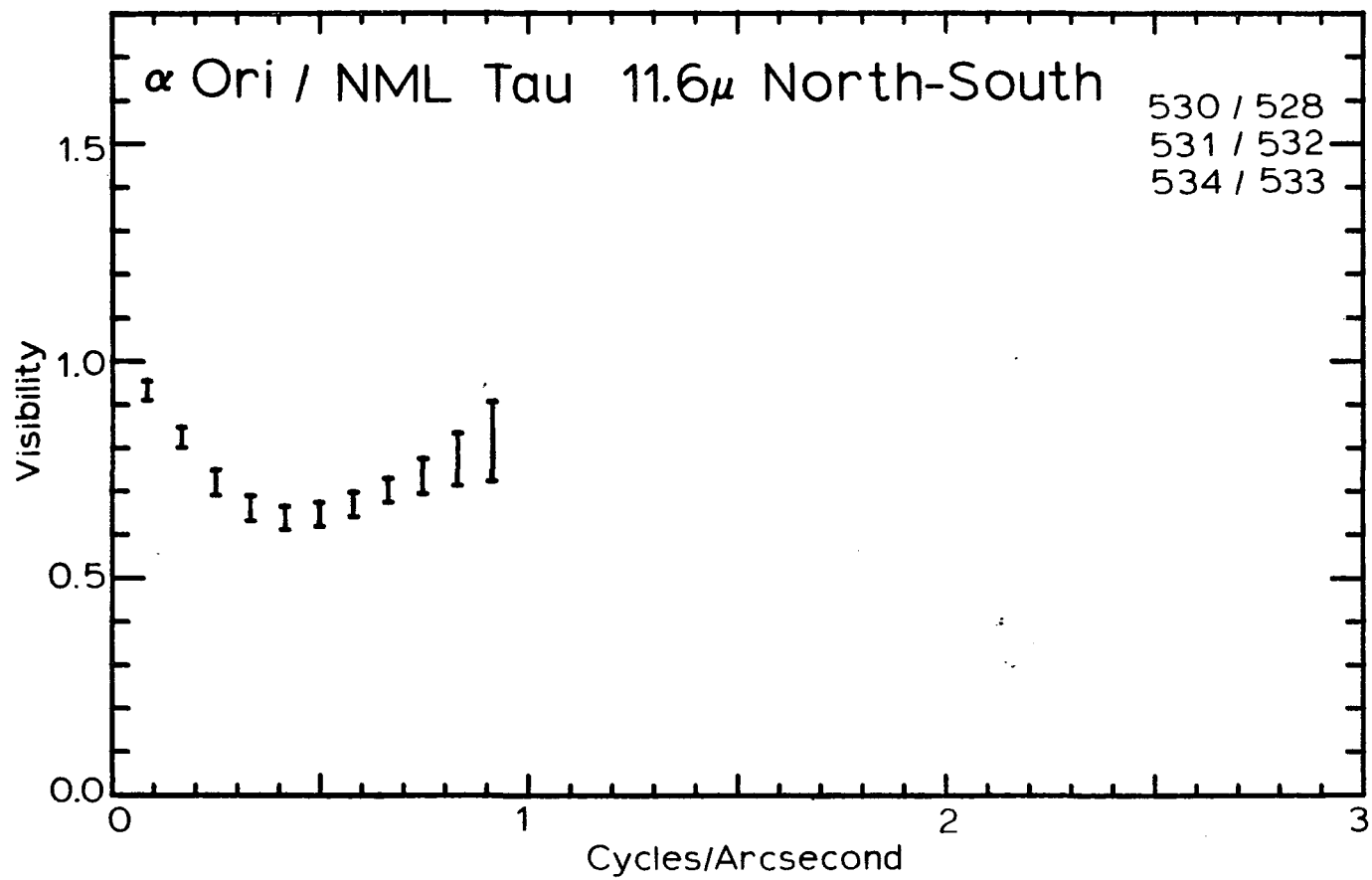


Fig. 35. Alpha Ori visibility. -- The resolved shell has a size of $\sim 4''$ and contributes 37% of the flux. The curve turns up at the end because NML Tau is slightly resolved.

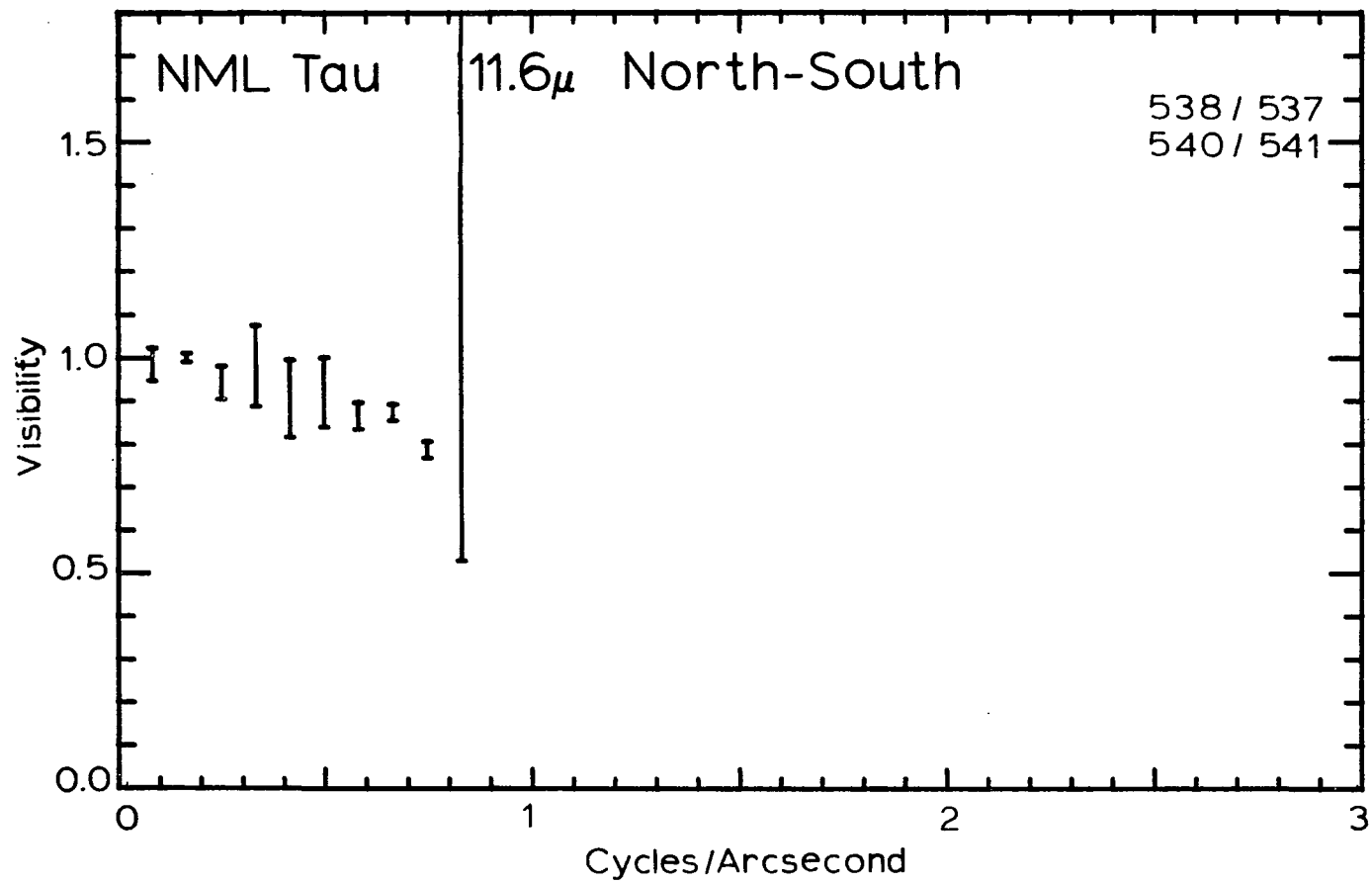


Fig. 36. NML Tau visibility.

The resolved flux of 0.37 agrees with Sutton but is somewhat greater than the 0.25 measured by McCarthy et al. After the baseline of 0.63 is subtracted the shape of the visibility curve can be fit equally well with a $4.0'' \pm 0.5$ uniform disk or a gaussian of diameter $3.1'' \pm 0.4$ at the $1/e$ points. This corresponds to more than 60 stellar radii.

VY CMa

This M3-5 oxygen rich supergiant is another object studied extensively with the Michelson interferometer (McCarthy 1978). Fig. 37 shows the 2 and 12 micron visibilities. These are the first observations at 2 microns and place an upper limit of $0.15''$ on the size at this wavelength. At 12 microns a uniform disk diameter is approximately $1.2''$ however this is a relatively poor fit and a more centrally peaked intensity distribution is needed. Since McCarthy has shown it is asymmetrical more observations will be needed to characterize this object.

Omicron Ceti

This prototype of the Mira variables has been resolved at 8, 10, and 12 microns (McCarthy et al. 1978). One observation suggests the visibility is variable. The present observations (Fig. 38) place the following upper limits on the near-infrared size (assuming a uniform disk): $0.2''$ at 2.2 microns, $0.2''$ at 3.5 microns, and $0.3''$ at 5 microns.

Other Objects

Figs. 39 through 43 give the visibility curves for IRC+10011, RX Boo, R Hyd, W Hyd, and CIT 6. These objects were all unresolved.

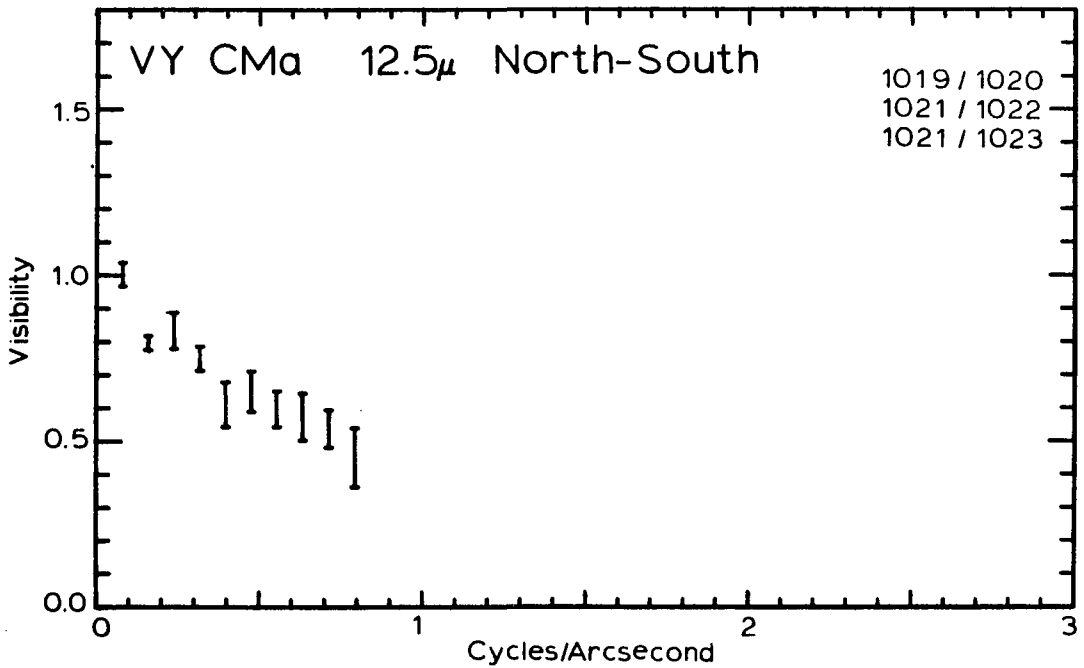
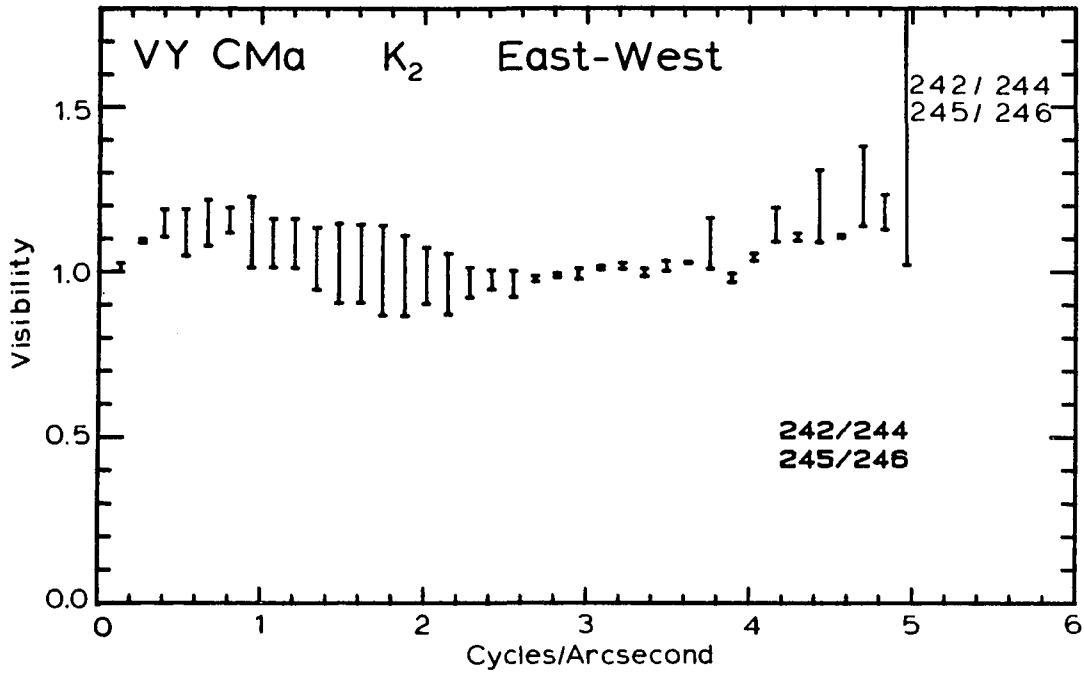


Fig. 37. VY CMa visibilities. -- The 2.2μ diameter is less than $0.15''$. The 12.6μ uniform disk diameter is $\sim 1.2''$ however a more centrally peaked intensity is indicated.

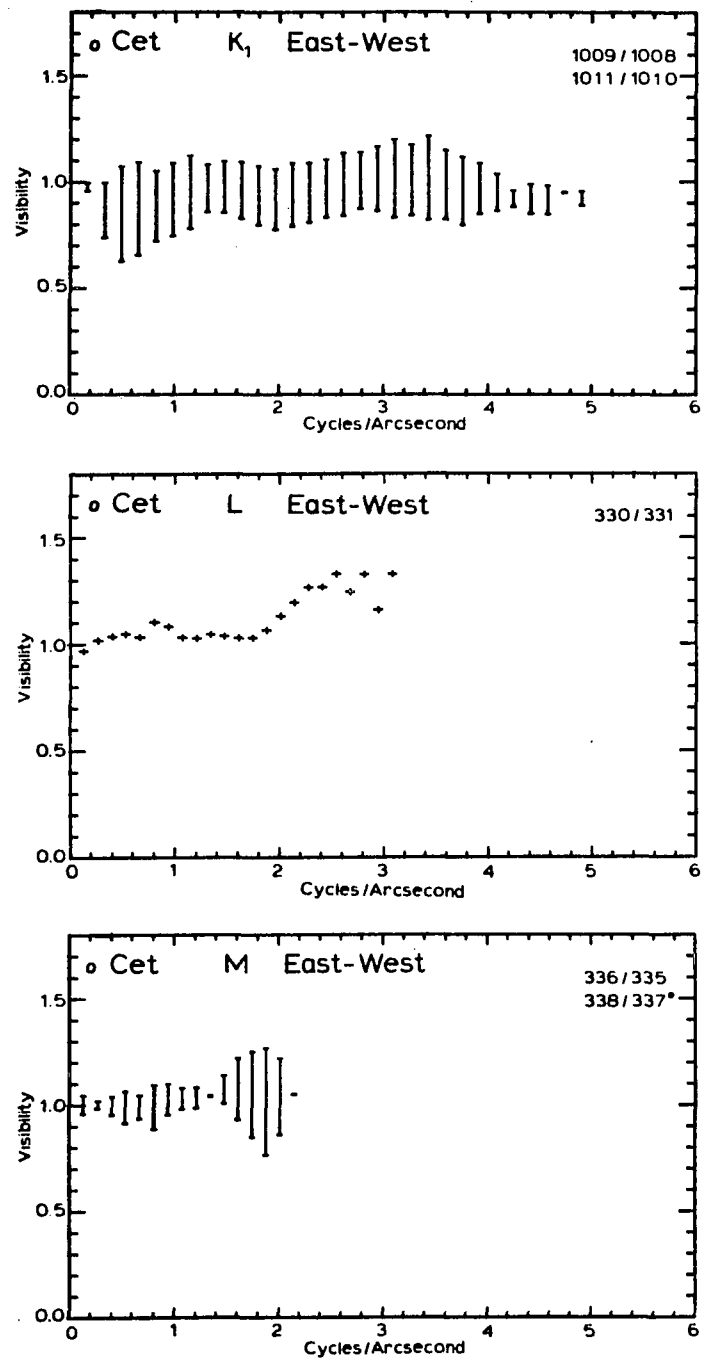


Fig. 38. Omicron Ceti visibilities. -- The diameter is less than 0.2" at 2.2 μ and 3.5 μ , and less than 0.3" at 5 μ .

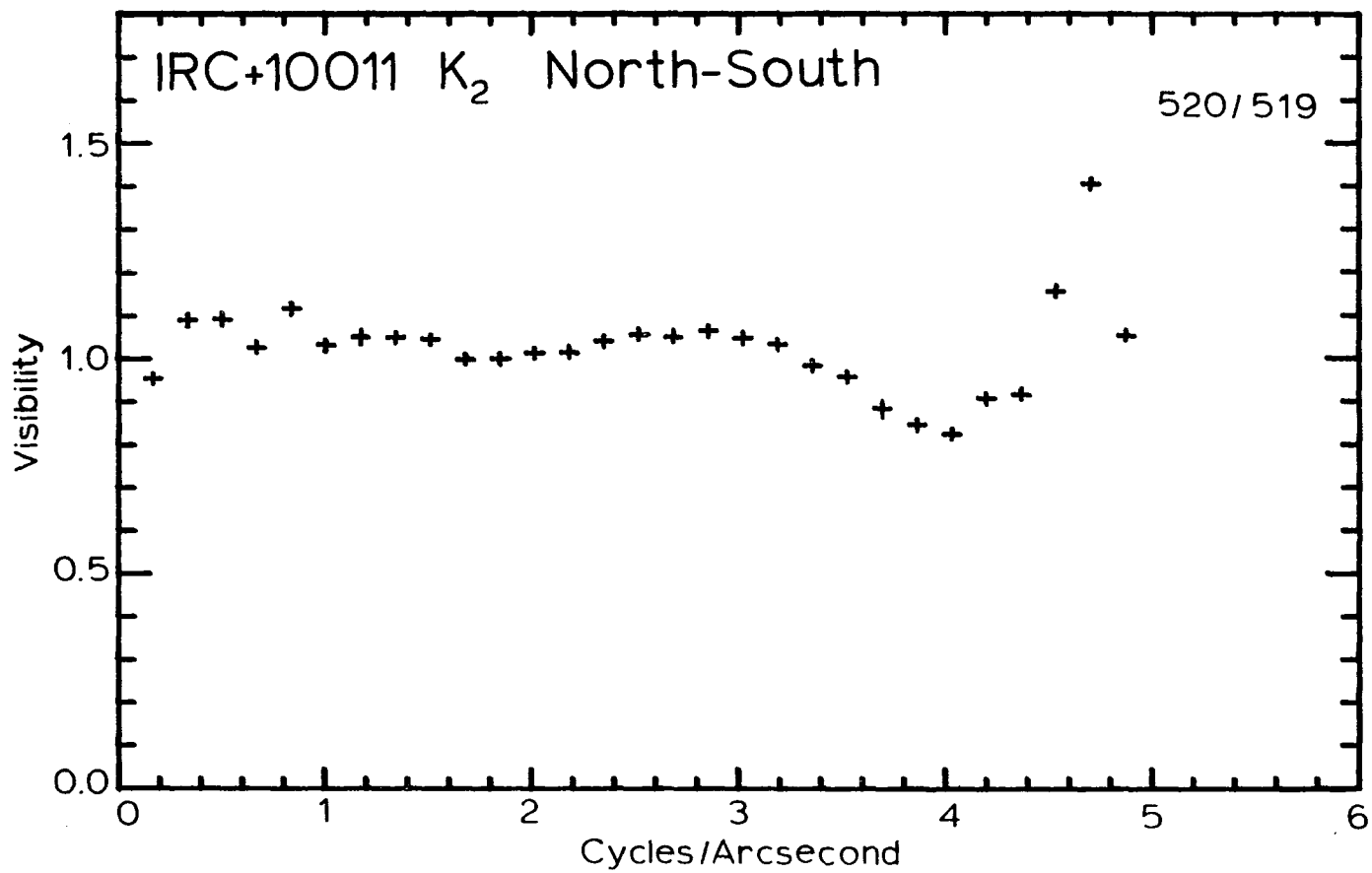


Fig. 39. IRC+10011 visibility. -- The diameter is less than 0.15".

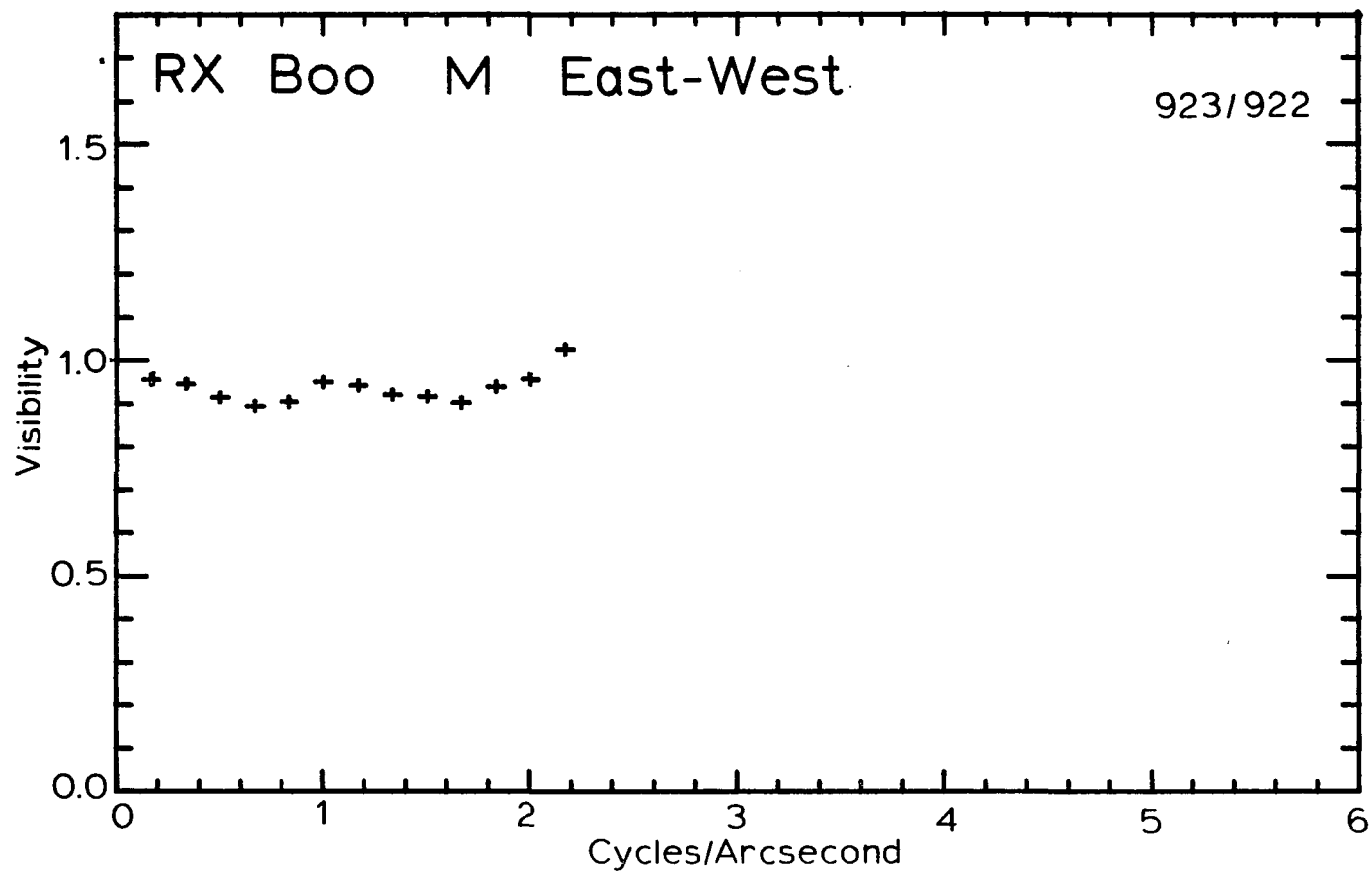


Fig. 40. RX Boo visibility. -- The diameter is less than 0.3".

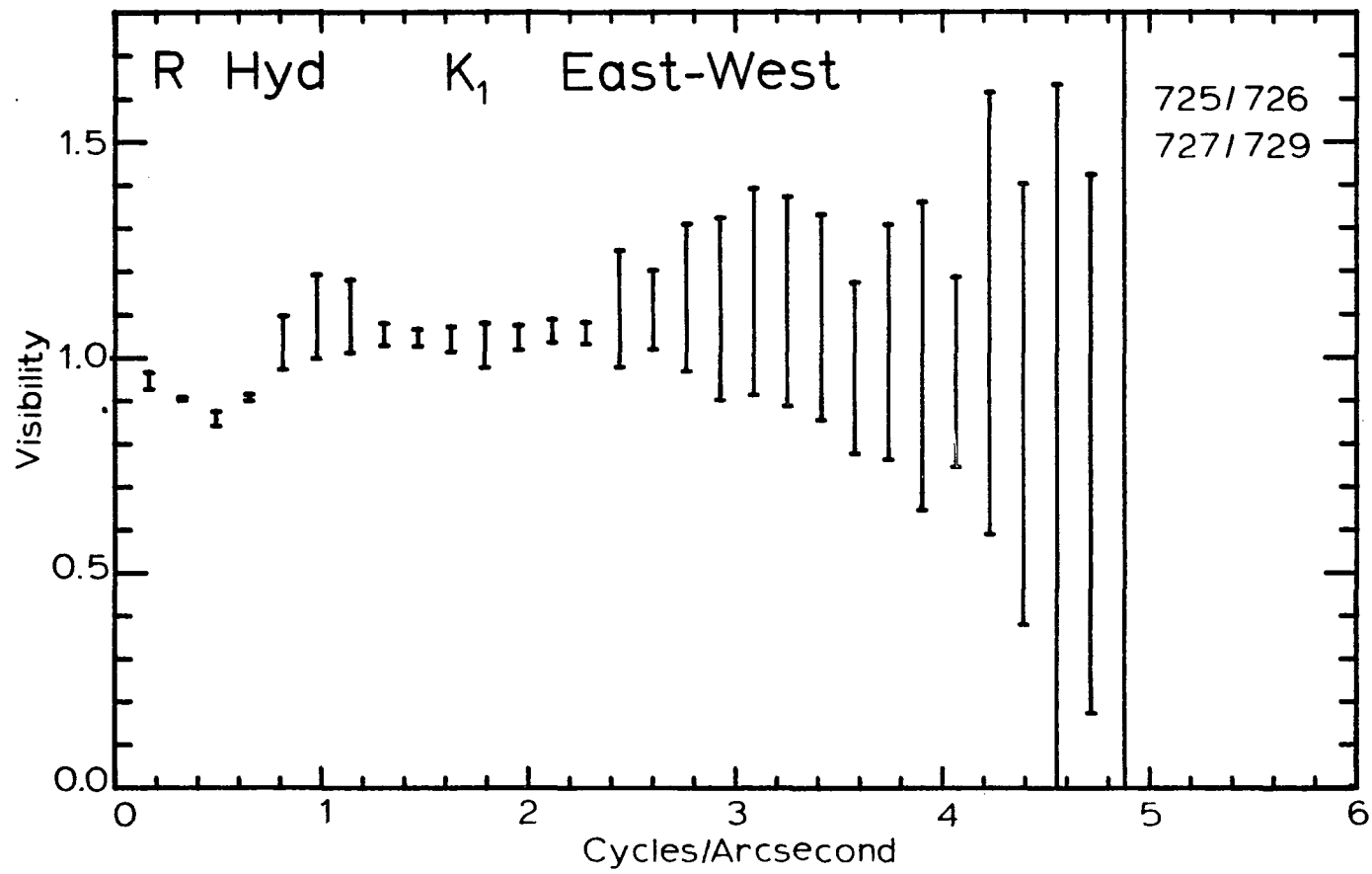


Fig. 41. R Hyd visibility. -- The diameter is less than 0.2".

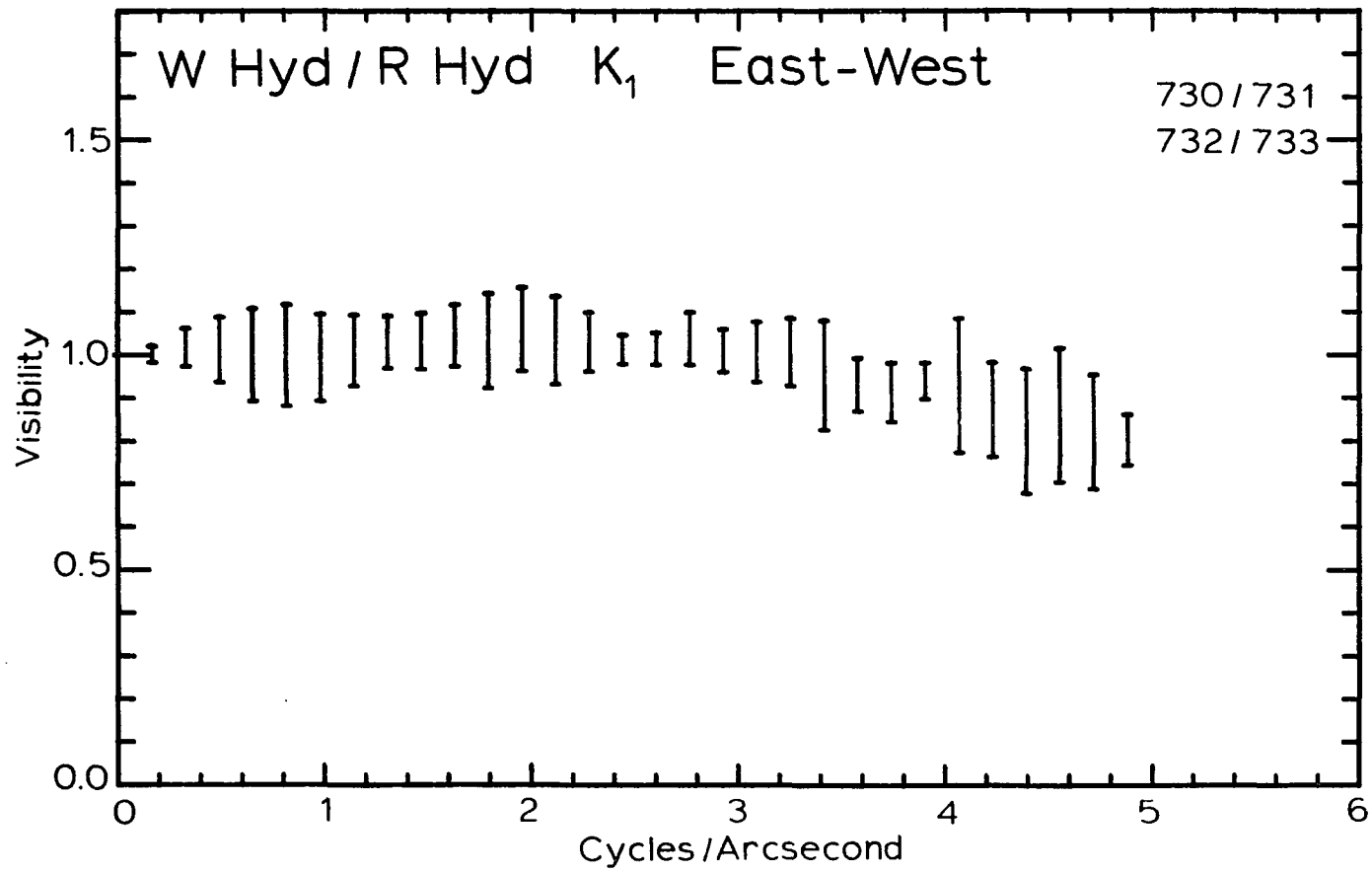


Fig. 42. W Hyd visibility. -- The diameter is less than 0.15".

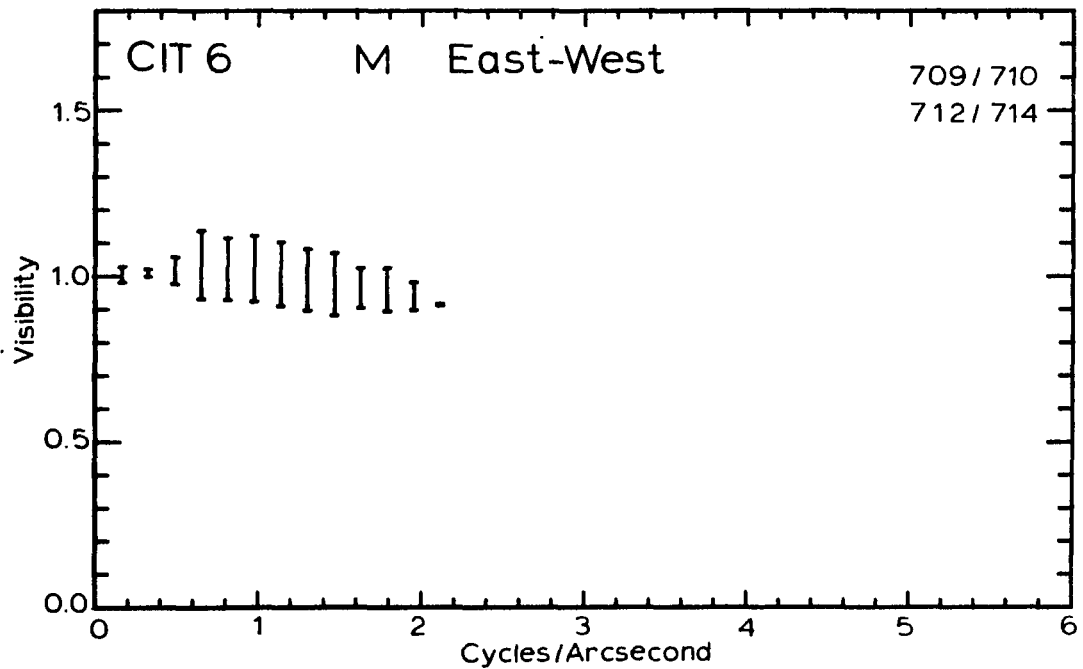
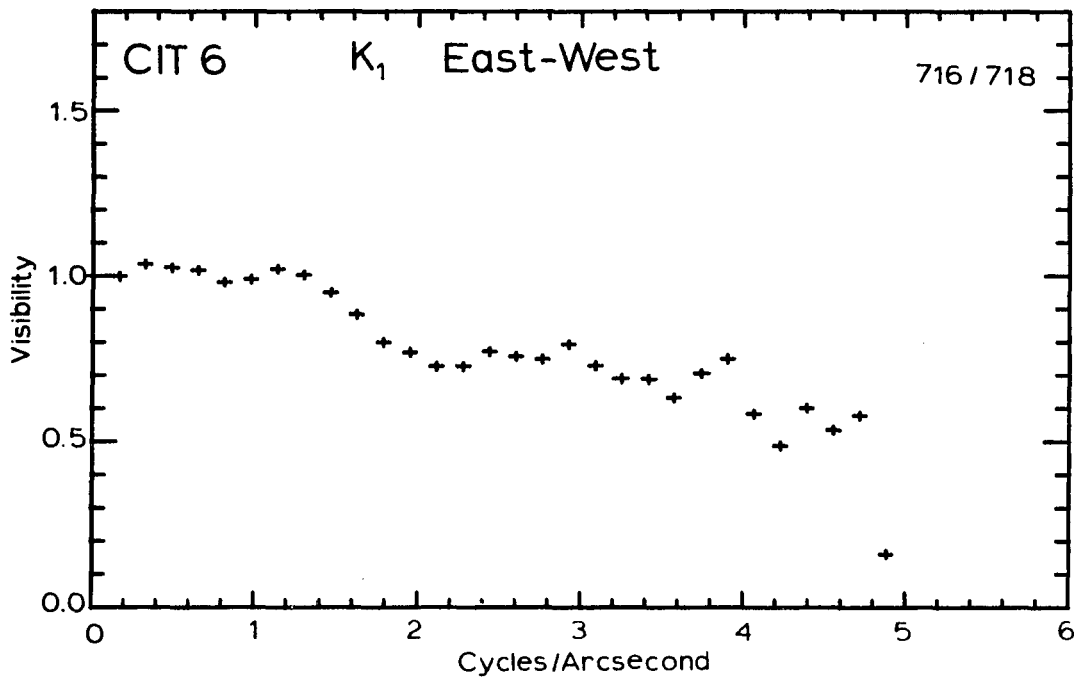


Fig. 43. CIT 6 visibilities. -- The diameter is less than $0.3''$ at 2.2μ and less than $0.25''$ at 5μ .

The upper limits are: IRC+10011 K < 0.15", RX Boo M < 0.3", R Hyd K < 0.2", W Hyd K < 0.15", CIT 6 K < 0.3", M < 0.25".

CHAPTER 6

SUMMARY AND FUTURE PLANS

The goals of this research have been to build a prototype speckle interferometer, to gain a better understanding of the requirements and limitations of speckle interferometry, and to extend the wavelength and spatial frequency coverage for the types of objects originally observed with the Michelson system. These goals have been accomplished, but much work remains to be done to improve the instrument and to extend the observations.

The speckle system has been built using equipment commonly available for infrared photometry. The chopping secondary was modified for fast scanning. Existing dewars were also used but this is one area where the requirements of speckle are different. The InSb dewar provided by Rieke and Lebofsky is the state of the art for photometry and spectroscopy and its excellent sensitivity in large part compensated for the diffraction losses with the speckle system. However a dewar designed to avoid these losses would result in more than a factor of 3 increase in sensitivity and would clearly be an important part of any future improvements. In addition the baffling should be improved to reduce the background for longer wavelengths. However even with the present sensitivity there are a large number of objects which can be observed.

This work has pointed out some misconceptions about the effects of the slit in the focal plane (chapter 3) and the effects of the finite length of the scan (chapter 4). In addition it has provided a basis for comparing the Michelson and speckle techniques. Sibille et al. (1979) define a merit factor in terms of signal-to-noise ratio for equal amounts of information and equal observing time. The speckle technique has a clear advantage. However a single merit factor can rarely describe the true advantages of one instrument over another. The Michelson cannot easily be used to provide the many spatial frequencies which are essential for interpreting objects such as W3 IRS 5 and IRC+10216. In addition, since the Michelson is usually operated with a fixed baseline, the visibilities at different wavelengths refer to different spatial frequencies and this complicates the analysis.

The Michelson system does however have an advantage under certain circumstances. The speckle system measures power which is highly attenuated by atmospheric turbulence and then relies on correction by a point source. Small variations in the turbulence can result in large changes in this attenuation. Perhaps a real time seeing monitor as proposed by Sibille et al. will alleviate this problem but at present the Michelson is less sensitive to seeing changes. For equal observing times and for a single frequency it gives greater accuracy. Therefore with objects where the shape of the visibility curve can be assumed, the Michelson is better. This is also true for objects which are only marginally resolved and only the highest spatial frequencies are of interest.

The third goal mentioned was to extend the wavelength and spatial frequency coverage. The orientation and magnitude difference of the double W3 IRS 5 has been determined. Two protostars, S140 and Mon R2 IRS 3 have been resolved. Upper limits have been placed on the diameters of BN, GL 490, GL 2591, and NGC 2264 IRS. These results show a wide range in the size of objects which otherwise have similar characteristics. Further observations as well as detailed models will be necessary to understand this.

New information has been obtained for several evolved stars. Visibility curves have been measured for IRC+10216 at 2, 5, 8, and 11 microns. In addition it has been observed in orthogonal directions at 2 and 8 microns. The asymmetry present at all spatial frequencies at 2 microns is not apparent out to 1 cycle/arcsecond at 8 microns. These observations should constrain future models of the temperature and density distribution and may make it possible to understand the source of the asymmetry. It will be important to observe this object throughout its 600 day period. The changes in visibility in response to the changes in the underlying luminosity source should provide an excellent test of radiative transfer theory in such thick envelopes. Several other stars were observed. The size of the silicate shell around Alpha Ori has finally been determined and additional observations have been obtained for VY CMa, NML Tau, CIT 6, Omicron Ceti, IRC+10011, R Hyd, W Hyd, and RX Boo.

Don McCarthy is continuing the IR speckle program at Arizona and it is hoped that many of the improvements mentioned above will soon be accomplished. He has also been involved in a joint program with

Kitt Peak. Using the 4 meter telescope with its scanning secondary they have obtained the first observations of an extragalactic source, NGC 1068. An IR speckle system for the MMT is also planned. The greatest advance in infrared speckle interferometry will come with the advent of high sensitivity arrays. In summary it is clear that infrared speckle observations will play an important role in understanding a wide range of infrared sources.

APPENDIX A

SIGNAL-TO-NOISE RATIO

The expression for the signal-to-noise ratio has been calculated by Sibille et al. (1979). A simplified derivation is given here. For bright objects the noise results from the random variations in the speckle images. However for faint objects the background and detector noise dominate. If the sampled signal is integrated over one scan the result is

$$F_{\lambda} \Delta\lambda A_t \frac{W}{x} S \quad (34)$$

or

$$F_{\lambda} \Delta\lambda A_t \frac{W}{L} S N \quad (35)$$

where Δx is the distance between samples, N is the number of samples per scan, and S is the responsivity. The other terms are defined in chapter 4. For an unresolved object the power at a given spatial frequency is then

$$\left(F_{\lambda} \Delta\lambda A_t M \frac{W}{L} S N \right)^2 \quad (36)$$

The total observing time of T is divided into $2n$ scans of length t , n on the object and n on the sky. So the total power from the object is

$$\frac{T}{2t} \left(F_{\lambda} \Delta\lambda A_t M \frac{W}{L} S N \right)^2 \quad (37)$$

If the noise is g (rms per root hertz) then this contributes power of

$$\frac{T}{2t} \left(\frac{1}{\sqrt{2}} g \sqrt{T} N \right)^2 \quad (38)$$

or

$$\frac{T}{2t} \left(\frac{1}{\sqrt{2}} g \frac{1}{\sqrt{t}} N \right)^2 \quad (39)$$

For noise the signal-to-noise ratio of each spectrum is one, so the standard deviation of this noise power is

$$\sqrt{\frac{T}{2t}} \left(\frac{1}{\sqrt{2}} g \frac{1}{\sqrt{t}} N \right)^2 \quad (40)$$

The subtraction of the sky from the object scans increases this by the square root of 2 so the total standard deviation in

$$\sqrt{\frac{T}{t}} \left(\frac{1}{\sqrt{2}} g \frac{1}{\sqrt{t}} N \right)^2 \quad (41)$$

The signal-to-noise ratio of the power is then

$$\frac{\frac{T}{2t} \left(F_{\lambda} \Delta\lambda A_t M \frac{W}{L} S N \right)^2}{\sqrt{\frac{T}{t}} \left(\frac{1}{\sqrt{2}} g \frac{1}{\sqrt{t}} N \right)^2} \quad (42)$$

$$= \frac{1}{4} \left(\frac{F_{\lambda} \Delta\lambda A_t M \frac{W}{L}}{g / s} \right)^2 \sqrt{T t} \quad (43)$$

The signal-to-noise ratio of the visibility (the square root of the power) is twice this

$$\frac{1}{2} \left(\frac{F_{\lambda} \Delta\lambda A_t M \frac{W}{L}}{NEP_s} \right)^2 \sqrt{T t} \quad (44)$$

SELECTED BIBLIOGRAPHY

- Aime, C. and Roddier, F., 1976, Opt. Comm., 19, 57.
- Aitken, D. K., and Jones, B., 1973, Ap. J., 184, 127.
- Allen, C. W., 1963, Astrophysical Quantities, (London: The Athlone Press)
- Allen, David A., 1972, Ap. J. Letters, 172, L55.
- Allen, David A., 1973, M.N.R.A.S., 161, 145.
- Becklin, E. E., Frogel, J. A., Hyland, A. R., Kristian, J., and Neugebauer, G., 1969, Ap. J. Letters, 158, L133.
- Beckwith, S., Evans, N. J. II, Becklin, E. E., and Neugebauer, G., 1976, Ap. J. 208, 390.
- Bedijn, P. J., Habing, H. J., and de Jong, T., 1978, Astr. Ap., 69, 73.
- Beichman, C. A., Becklin, E. E., Capps, R. W., and Dyck, H. M., 1979, Bull.A.A.S., 9, 606.
- Blair, Guy N., Evans, N. J. II, van den Bout, Paul A., and Peters, William L. III, Ap. J., 219, 896.
- Bracewell, Ron, 1965, The Fourier Transform and its Applications, (New York: McGraw-Hill)
- Campbell, M. F., Elias, J. H., Gezari, D. Y., Harvey, P. M., Hoffmann, W. F., Hudson, H. S., Neugebauer, G., Soifer, B. T., Werner, M. W., and Westbrook, W. E., 1976, Ap. J., 208, 396.
- Capps, R. W., and Knacke, R. F., 1976, P.A.S.P., 88, 224.
- Caswell, J. R., 1974, in IAU Symp. #60: Galactic Radio Astronomy, F. J. Kerr and S. C. Simonson III, ed. (Boston: D. Reidel), p. 423.
- Chelli, Alain, 1979, Ph. D. Dissertation, l'Universite de Paris VII
- Chelli, Alain, Léna, Pierre, Sibille, Francois, 1979, Nature, 278, 143.

- Cohen, Martin, Anderson, Christopher M., Cowley, Anne, Coyne, George V., Fawley, William M., Gull, T. R., Harlan, E. A., Herbig, G. H., Holden, Frank, Hudson, H. S., Jakoubek, Roger O., Johnson, Hugh M., Merrill, K. M., Schiffer, Francis H. III, Soifer, B. T., and Zuckerman, Ben, 1975, *Ap. J.*, 196, 179.
- Coyne, George V., S.J., and Vrba, Frederick J., 1976, *Ap. J.*, 207, 790.
- Crabtree, Dennis R., and Martin, P. G., 1979, *Ap. J.*, 227, 900.
- Crampton, D., and Fisher, W. A., 1974, *Pub. D. A. O.*, 14, No. 12.
- Currie, D. B., Knapp, S. L., and Liewer, K. M., 1974, *Ap. J.*, 187, 131.
- Dainty, J. C., 1973, *Opt. Comm.*, 7, 129.
- Dainty, J. C., and Greenaway, A. H., 1979, *J.O.S.A.*, 69, 786.
- Dickel, H. R., Wendker, H. and Bieritz, J. H., 1969, *Astr. Ap.*, 1, 270.
- Dinerstein, Harriet, Lester, Daniel F., and Rank, David M., 1979, *Ap. J. Letters*, 227, L39.
- Dinger, Ann St. Clair, Dickinson, Dale F., Gottlieb, C. A., and Gottlieb, E. Webster, 1979, *P.A.S.P.*, 91, 830.
- Dollfus, A., and Zellner, B., 1979, in *Asteroids*, T. Gehrels, ed. (Tucson: University of Arizona Press), p. 170.
- Dyck, H. M., and Capps, R. W., 1978, *Ap. J.*, 220, 449.
- Dyck, H. M., Forbes, F. F., and Shawl, S. J., 1971, *A. J.*, 76, 901.
- Dyck, H. M., and Lonsdale, Carol J., 1979, *A. J.*, 84, 1339.
- Dyck, H. M., and Simon, Theodore, 1975, *Ap. J.*, 195, 689.
- Elsässer, H. and Staude, H. J., 1978, *Astr. Ap.*, 70, L3.
- Finsen, W. S., and Worley, C. E., 1970, *Republic Obs. Johannesburg Circ.*, No. 7, p. 203.
- Foy, R., Chelli, A., Sibille, F., and Léna, P. 1979, *Astr. Ap.*, 79, L5
- Fried, David L., 1979, in *High Angular Resolution Stellar Interferometry: Proc. of IAU Coll. 50*, John Davis and William J. Tango, ed. (Sydney: Chatterton Astr. Dept. Univ. of Sydney), p. 4-1.
- Fried, David L., 1966, *J.O.S.A.*, 56, 1372.

- Genzel, R., Downes, D., Moran, J. M., Johnston, K. J., Spencer, J. H., Walker, R. C., Haschick, A., Matveyenko, L. I., Kogan, L. R., Kostenko, V. I., Rönning, B., Rydbeck, O. E., and Moiseev, I. G., 1978, *Astr. Ap.*, 66, 13.
- Gillett, F. C., Forrest, W. J., Merrill, K. M., Capps, R. W., and Soifer, B. T., 1975, *Ap. J.* 200, 609.
- Habing, H. J., and Israel, F. P., 1979, *Ann. Rev. Astron. Astrophys.*, 17, 345.
- Hanbury Brown, R., 1974, *The Intensity Interferometer*, (New York: Halsted Press)
- Harvey, Paul M., Campbell, Murray F., and Hoffmann, William F., 1977, *Ap. J.*, 215 151.
- Harvey, Paul M., Campbell, Murray F., and Hoffmann, William F., 1978, *Ap. J.*, 219, 891.
- Harvey, Paul M., Campbell, Murray F., Hoffmann, William F., Thronson, Harley A. Jr., and Gatley, Ian, 1979, *Ap. J.*, 229, 990.
- Herbig, G. H., and Zappala, R. R., 1970, *Ap. J. Letters*, 162, L15.
- Hufnagel, R. E. and Stanley, N. R., 1964, *J.O.S.A.*, 54, 52.
- Korff, D. 1973, *J.O.S.A.*, 63, 971.
- Korff, D., Dryden, G. and Miller, M. G., 1972, *Opt. Comm.*, 5, 187.
- Krassner, Jerry, Smith, Lewis L., and Hilgeman, T., 1979, *Ap. J. Letters*, 231, L31.
- Kwan, John, and Scoville, Nick, 1976, *Ap. J.*, 209, 102.
- Labeyrie, A., 1970, *Astr. Ap.*, 6, 85.
- Labeyrie, Antoine, 1978, *Ann. Rev. Astron. Astrophys.*, 16, 77.
- Lada, Charles J., and Harvey, Paul M., 1980, preprint
- Léna, P., Sibille, F., and Chelli, A., 1980, in *Optical and Infrared Telescopes of the 1990's*, Adelaide Hewitt, ed. (Tucson: Kitt Peak National Observatory), p. 840.
- Low, F. J., 1980, in *Optical and Infrared Telescopes of the 1990's*, Adelaide Hewitt, ed. (Tucson: Kitt Peak National Observatory), p. 825.

- Martin, Peter G., 1978, *Cosmic Dust: Its Impact on Astronomy*, (Oxford: Oxford University Press)
- McAlister, Harold A., 1977, *Ap. J.*, 215, 159.
- McAlister, Harold A., 1978, *Ap. J.*, 225, 932.
- McAlister, Harold A., and DeGioia, Kathleen A., 1979, *Ap. J.*, 228 493.
- McAlister, Harold A., 1979, *Ap. J.*, 230, 497.
- McCarthy, Donald W., 1976, Ph.D. Dissertation, University of Arizona
- McCarthy, Donald W., 1978, High Angular Resolution Stellar Interferometry: Proc. IAU Colloq. 50, John Davis and William J. Tango, ed. (Sydney: Chatterton Astr. Dept., Univ. of Sydney), p. 18-1
- McCarthy, D. W., Howell, R., and Low, F. J., 1977a, *Opt. Eng.*, 16, 569.
- McCarthy, D. W., Howell, R., and Low, F. J., 1977b, *Ap. J. Letters*, 214, L85.
- McCarthy, D. W., Howell, R., and Low, F. J., 1978, *Ap. J. Letters*, 223, L113.
- McCarthy, D. W., Howell, R., and Low, F. J., 1980, *Ap. J. Letters*, 235, L27.
- McCarthy, D. W., and Low, F. J., 1975, *Ap. J. Letters*, 202, L37.
- McCarthy, D. W., Low, F. J., and Howell, R., 1979, *S.P.I.E.*, 172, 140.
- McCarthy, D. W., and White, R., 1980, in preparation.
- McCarthy, D. W., and Woolf, N. J., 1980, in preparation.
- Meeus, Jean, 1971a, *Sky and Telescope*, 41, 21.
- Meeus, Jean, 1971b, *Sky and Telescope*, 41, 89.
- Merrill, K. M., Russell, R. W., and Soifer, B. T., 1976, *Ap. J.*, 207, 763.
- Merrill, K. M., and Soifer, B. T., 1974, *Ap. J. Letters*, 189, L27.
- Merrill, K. M., and Stein, W. A., 1976a, *P.A.S.P.*, 88, 285.
- Merrill, K. M., and Stein, W. A., 1976b, *P.A.S.P.*, 88, 294.
- Merrill, K. M., and Stein, W. A., 1976c, *P.A.S.P.*, 88, 874.

- Morrison, David, and Lebofsky, Larry, 1979, in Asteroids, T. Gehrels, ed. (Tucson: University of Arizona Press), p. 184.
- Puetter, R. C., Russell, R. W., Soifer, B. T., and Willner, S. P., 1979, Ap. J., 228, 118.
- Rieke, G. H., and Low, F. J., 1974, in Methods of Experimental Physics, Vol. 12A N. Carelton, ed. (New York: Academic Press), p. 415.
- Rieke, G. H., Montgomery, E. F., Lebofsky, M. J., and Eisenhardt, P. R., 1980, submitted to Applied Optics.
- Roddier, F., 1974, Opt. Comm., 10, 103.
- Schwartz, Mischa and Leonard, Shaw, 1975, Signal Processing: Discrete spectral analysis, detection, and estimation, (New York: McGraw-Hill)
- Scoville, N. Z., and Kwan, John, 1976, Ap. J., 206, 718.
- Selby, M. J., Wade, R., Magro, C., 1979, M.N.R.A.S., 187, 553.
- Shawl, Stephen J., and Zellner, Ben, 1970, Ap. J. Letters, 162, L19.
- Sibille, F., Chelli, A. and Léna, P., 1979, Astr. Ap., 79, 315.
- Simon, Theodore, Simon, M., and Joyce, R. R., 1979, Ap. J., 230, 127.
- Stachnik, Robert Victor, 1976, Dissertation, State University of New York
- Sutton, Edmund Charles, 1979, Ph.D. Dissertation, University of California, Berkeley
- Sutton, E. C., Betz, A. L., Storey, J. W. V., and Spears, D. L., 1979, Ap. J. Letters, 230, L105.
- Sutton, E. C., Storey, J. W. V., Betz, A. L., Townes, C. H., and Spears, D. L., 1977, Ap. J. Letters, 217, L97.
- Sutton, E. C., Storey, J. W. V., and Townes, C. H., 1978, Ap. J. Letters, 224, L123.
- Tatarski, V. I., 1961, Wave Propagation in a Turbulent Medium, (New York: McGraw-Hill).
- Tatarski, V. I., 1971, The Effects of the Turbulent Atmosphere on Wave Propagation, (Jerusalem: Keter Press, available from US Dept. of Comm.).

- Thompson, Rodger I., and Tokunaga, Alan T., 1978, Ap. J., 226, 119.
- Thompson, Rodger I., and Tokunaga, Alan T., 1979, Ap. J., 231, 736.
- Thronson, Harley A. Jr., Campbell, Murray, F., and Hoffmann, William F., 1980, Ap. J., 239, 533.
- Thronson, Harley A. Jr., Gatley, Ian, Harvey, P. M., Sellgren, K., and Werner, M. W., 1980, preprint.
- Thronson, Harley A. Jr., and Harper, D. A., 1979, Ap. J., 230, 133.
- Tokunaga, A. T., Erickson, E. F., Caroff, L. J., and Dana, R. A., 1978 Ap. J. Letters, 224, L19.
- Toombs, R. I., Becklin, E. E., Frogel, J. A., Law, S. K., Porter, F. C., and Westphal, J. A., 1972, Ap. J. Letters, 173, L71.
- Van Blerkom, David, and Auer, Lawrence, 1976, Ap. J., 204, 775.
- Wannier, P. G., Leighton, R. B., Knapp, G. R., Redman, R. O., Phillips, T. G., and Huggins, P. J., 1979, Ap. J., 230, 149.
- Wendker, H. J., and Baars, J. W. M., 1974, Astr. Ap., 33, 157.
- Werner, M. W., Becklin, E. E., Gatley, Ian, Neugebauer, G., Sellgren, K., Thronson, Harley A. Jr., Harper, D. A., Loewenstein, R., and Moseley, S. H., 1980, preprint.
- Werner, M. W., Becklin, E. E., Neugebauer, G., 1977, Science 197, 723.
- Weymann, R., 1962, Ap. J., 136, 844.
- Willner, S. P., 1977, Ap. J., 214, 706.
- Worden, Simon P., Stein, Murray K., Schmidt, Gary D., and Angel, J. R. P., 1977, Icarus, 32, 450.
- Wynn-Williams, C. G., 1974, in Proc. IAU Symposium No. 60, Galactic Radio Astronomy, F. J. Kerr and Simonson, S. C. III, ed. (Boston: D. Reidel), p. 259.
- Wynn-Williams, C. G., 1976, Observatory, 96, 6.
- Wynn-Williams, C. G., and Becklin, E. E., 1974, P.A.S.P., 86, 5.
- Wynn-Williams, C. G., Becklin, E. E., Forster, J. R., Matthews, K., Neugebauer, G., Welch, W. J., and Wright, M. C. H., 1977, Ap. J. Letters, 211, L89.

- Wynn-Williams, C. G., Becklin, E. E., Neugebauer, G., 1972, M.N.R.A.S.,
160 1.
- Wynn-Williams, C. G., Becklin, E. E., and Neugebauer, G., 1974, Ap. J.,
187, 473.
- Wynn-Williams, C. G., Werner, M. W., and Wilson, W. J., 1974, Ap. J.,
187 41.
- Zappala, R. R., Becklin, E. E., Matthews, K., and Neugebauer, G., 1974,
192, 109.
- Zellner, Benjamin H., and Serkowski, Krzysztof, 1972, P.A.S.P., 84, 619.